NASA CR 152087

(D. Koenig)

ANALYTICAL STUDY OF STOL AIRCRAFT IN GROUND EFFECT

PART I. NONPLANAR, NONLINEAR WING/JET LIFTING SURFACE METHOD

C. A. SHOLLENBERGER and D. N. SMYTH

DOUGLAS AIRCRAFT COMPANY
LONG BEACH, CALIFORNIA
90846

March 1978

Prepared for:

NATIONAL AERONAUTICS AND SPACE ADMINISTRATION
NASA AMES RESEARCH CENTER
CONTRACT NAS2-9319

(NASA-CR-152087-Pt-1) ANALYTICAL STUDY OF STOL AIRCRAFT IN GROUND EFFECT. PART 1: NONPLANAR, NONLINEAR WING/JET LIFTING SURFACE METHOD (Douglas Aircraft Co., Inc.) 91 p HC A05/MF A01 CSCL 01C G3/05

N81-19096

Unclas 17803

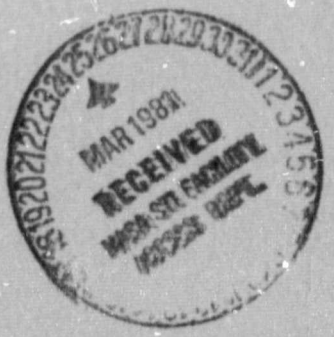

FOREWORD

The results of an analytical investigation of nonlinear, nonplanar analysis methods applicable to both thin-jet modeling and thick-jet modeling of STOL aircraft ground effect phenomenon are presented. The study consisted of two concurrent tasks which are reported on separately as Parts I and II.

Part I. Nonplanar, Nonlinear Wing/Jet Lifting Surface Method. The objective of this task was to extend the Douglas Nonplanar Lifting Systems program to include powered-lift wings having thin jets of varying strength for both part and full span arrangements and to analyze various configurations in ground effect.

Part II. Nonplanar, Nonlinear Method Applicable to Three-Dimensional Jets of Finite Thickness. The objective of this task was to apply the NASA Ames Research Center Potential Flow Analysis to power-off ground effect cases and recommend procedures for developing a thick-jet analysis method.

This study, conducted by the Technology Programs Section, Aerodynamics Subdivision of the Douglas Aircraft Company, was sponsored by the NASA Ames Research Center under Contract NAS2-9319. Dr. C. A. Shollenberger served as principal investigator for the study under the technical direction of Mr. D. N. Smyth. The NASA project engineer was Mr. David Koenig of the Large Scale Aerodynamics Branch.

The contributions of Mr. M. I. Goldhammer, who served as the principal investigator on Part I during the early stages of the study, are greatly appreciated. His previous work on the development of the Nonplanar Lifting Systems program contributed significantly to the present work. The assistance of Mr. D. H. Neuhart in preparing the input and running many of the cases is also appreciated.

The authors also gratefully acknowledge the contributions of Dr. R. T. Medan of the NASA Ames Research Center for his assistance and support in the application of the NASA Ames Research Center Potential Flow Analysis to aircraft ground effects prediction.

TABLE OF CONTENTS

LIST OF FIGURES

LIST OF SYMBOLS

A	velocity induction coefficient resulting from wing influence
b	reference span
B	velocity induction coefficient resulting from jet influence
c	local wing chord
$\bar{c}$	reference chord
$\bar{\bar{c}}$	mean aerodynamic chord
C_{d_i}	section induced drag coefficient
C_{D_i}	total induced drag coefficient
$\vec{C}_f$	section force coefficient vector
C_J	sectional jet momentum coefficient
C_ℓ	section lift coefficient
C_L	total lift coefficient
C_M	total pitching moment coefficient
C_N	total yawing moment coefficient
C_p	pressure coefficient
C_R	total rolling moment coefficient
C_S	section leading edge suction coefficient
C_Y	total side force coefficient
F_S	section leading edge suction force
$\vec{i},\vec{j},\vec{k}$	unit vector in x,y,z directions
ℓ	streamwise element length
M	Mach number
n	local normal coordinate
$\vec{n}$	unit vector normal to local surface
p	static pressure

r	distance between influenced point and induction element
R	radius of curvature
s	arc length along lifting surface
S	area of integration; arc length along jet sheet; reference wing area
$\vec{t}$	unit vector tangential to local surface
u	local tangential flow speed
$\bar{u}$	average tangential flow speed
$\vec{\bar{u}}$	average tangential flow velocity vector
U	freestream flow speed
$\vec{U}$	freestream velocity vector
$\vec{V}$	local velocity vector
x,y,z	Cartesian coordinates
α	angle of attack relative to freestream velocity vector
β	Prandtl-Glauert compressibility correction factor
γ	vortex strength; flight path angle
δ	jet width
δ_J	jet deflection angle
ζ	dummy z-coordinate
η	dummy y-coordinate
ξ	dummy x-coordinate; coordinate along element centerline
θ	jet element angle relative to horizontal axis; wing attitude angle
ϕ	velocity potential
ρ	fluid density

Subscripts

c	cross-stream
i,j	matrix equation subscripts
J	jet

JR	jet reaction
k	dummy index
ℓ	lower surface
l	rolling moment
m	pitching moment
mc	moment center
n	normal direction; yawing moment
o	referenced to coordinate origin; incompressible plane; outer flow
s	streamwise
te	trailing edge
u	x-component of velocity; upper surface
v	y-component of velocity
w	z-component of velocity
W	wing
x	x-component of vector
y	y-component of vector
z	z-component of vector
Γ	circulation value
1	upstream element of adjoining pair
2	downstream element of adjoining pair

Superscripts

'	coefficient of elementary vortex distribution function
ν	iterative step number

1. INTRODUCTION

Technology relevant to the prediction of aerodynamic characteristics of powered lift systems has advanced significantly with the increased motivation provided by application of propulsive lift to achieve Short Field Takeoff and Landing (STOL) performance. Powered lift prediction techniques can primarily be categorized as either thick or thin jet analyses. Thick jet methods originated with early propeller slipstream-wing interaction analyses, such as References 1-4, and progressed to analyses such as References 5-8 to include nonlinear and nonplanar characteristics of present externally blown flap or upper surface blown configurations. Generally thick jet prediction techniques have lagged the thin jet methods in development and also in level of application to design studies. Reference 9 discusses thick jet analysis methodology and its applicability to the NASA Ames Potential Flow Analysis program.

The thin jet approach to powered lift system analysis has centered on the jet flap concept described by Spence in Reference 10. In this formulation, the jet flap model applies to a thin, high speed jet sheet issuing from the wing trailing edge but has been successfully employed to analyze more practical powered lift systems which seemingly violate the jet flap model assumptions. As a result of the simplicity and acknowledged usefulness of thin jet flap analyses, the jet flap model will be employed presently to provide a tool for analysis of powered lift systems in proximity to the ground. As a result of the inherent nonplanar and nonlinear aspects of the ground effects problem, previous linearized jet flap analyses, such as References 11-13, are not sufficient for the present study. Consequently, a nonlinear, nonplanar jet flap finite element analysis has been developed and applied to powered lift systems in ground proximity. The present method is derived from the lifting surface theory of Reference 14 with an adaptation of the iterative two-dimensional jet flap solution method of Reference 15.

The resultant nonlinear and nonplanar jet flap analysis will be described in the next section including formulation and implementation of the method. Subsequent discussions consider the validation and application of the resultant

method for prediction of the characteristics of both powered and unpowered lift systems in ground effect. Finally, recommendations for further improvement of the powered lift ground effects technology are suggested.

2. ANALYSIS

The jet flap model of a thin, high speed jet originating at a wing trailing edge has been a mainstay of powered lift system analysis. Jet flap analysis techniques have obtained a considerable level of sophistication including nonlinear two-dimensional methods (References 15 and 16) and linearized three-dimensional finite element analysis for general configurations (Reference 12). However, since a nonplanar, nonlinear three-dimensional jet-flap analysis is not available, a combination of the nonplanar, nonlinear elementary vortex distribution lifting surface theory of Reference 14 with the basic jet flap iterative scheme of the two-dimensional method of Reference 15 has been formed to study powered lift systems in ground influence. The objective of the present study is the development of a tool for evaluation of general powered lift system ground effects where nonlinear and nonplanar aspects may be important.

The lifting surface theory of References 17 and 18 is an adaptation of the elementary vortex distribution lifting surface theory of Reference 12 which represents thin wing vorticity by superposition of piecewise linear and inverse square root vortex strength functions. Unlike its predecessor which applied boundary conditions linearized in angle of attack, flap deflection, camber angle, etc., the method of Reference 17 includes nonlinear aspects in the application of wing boundary conditions as well as nonplanar effects of the lifting surface geometry and therefore is referred to as the Nonplanar Lifting Systems (NPLS) method. The NPLS method has proven useful in prediction of aerodynamic characteristics of wing-winglet combinations, multielement high lift systems and wings in ground effects. Since the NPLS theory was derived from a linearized jet flap analysis, the incorporation of a jet flap model into the NPLS program is a logical development.

The basic jet flap solution technique selected for combination with the NPLS method is the iterative scheme, employed in Reference 15 to solve the jet flap problem in two dimensions. This two-dimensional jet flap methodology applies superposition of vortex strength distributions to represent the jet vorticity and therefore is compatible with the NPLS formulation. An iterative solution technique is employed in Reference 15 to successively approximate

the thin jet position and the jet vorticity strengths until appropriate boundary conditions are satisfied. In the present analysis the spanwise curvature or "roll-up" of the jet sheet is suppressed and consequently the two-dimensional method of Reference 15 is directly applicable. However, additional complications and difficulties are introduced by the third spatial dimension which derogate the well behaved convergence characteristics of the jet solution method in two dimensions. Nevertheless, acceptable solution characteristics are observed for the present three-dimensional method for most configurations when proper attention is given to the analysis representation of the configuration and input preparation.

The remainder of this section describes the formulation and implementation of the present nonlinear, nonplanar jet flap methodology including the analysis assumptions, limitations, and usage.

2.1 Assumptions and Limitations

The analysis developed below is intended to predict the aerodynamic characteristics of three-dimensional lifting surfaces with thin jets attached to their trailing edges. All wing-like elements within the flowfield are assumed to be adequately represented by surfaces of zero thickness with trailing edges from which the flow departs smoothly (except for deflected jet cases) and leading edges with infinite curvature. The infinitely-thin wing approximation is a commonly employed model to represent wings with finite airfoil section thickness thereby facilitating economical analysis of three-dimensional systems. Typically three-dimensional analyses accounting for wing thickness (such as Reference 19) require substantially more computation time than lower-order thin wing methods (such as vortex lattice techniques) or higher-order thin wing analyses such as presently employed. The consideration of computational resource expenditure is of great importance for nonlinear jet analysis where iterative solution schemes require repeated solution of the usual wing problem. Therefore, the basic wing lifting surface formulation of Reference 17 is appropriate for nonlinear analysis of jet flapped wings.

Similarly the zero thickness jet flap model of Reference 10 is a computationally efficient representation of high speed thin jets issuing from wing

trailing edges. This jet model has demonstrated amazing capability for the analysis of several configurations such as externally blown flaps, augmentor wings or upper surface blown flaps where the basic assumptions of the representation are seemingly violated. As with thin wing theory, the jet flap model is a practical representation of complex problems. An additional assumption regarding the present jet model ignores roll-up of the jet in the cross-stream direction. The jet momentum deflection in the streamwise direction, with the corresponding pressure differential across the jet, is intuitively anticipated to produce the dominant influence on the flow about a wing in comparison with the influence of the cross-stream jet deflections. The roll-up of trailing vortex wakes of unpowered lifting surfaces has been demonstrated to be of minor significance for loads determination and this result is extended without proof to powered configurations in the present development. Furthermore, practical geometrical constraints and complexity of the finite elements representing the jet in the present analysis precludes consideration of the jet cross-stream roll-up.

The fluid in which the jet flapped wing is immersed is presently assumed to be inviscid and incompressible. Fluid compressibility is generally of secondary importance for the ground approach case where the aircraft speed is much less than the speed of sound. Since the jet flap model ignores the internal jet fluid mechanics by the idealization of zero jet thickness, compressibility effects resulting from high jet flap speeds and high temperatures are not relevant to the basic analysis formulation. Propulsive jets will be characterized solely by their momentum. Detailed jet velocity and density distributions producing the momentum are not within scope of the jet flap model. Similarly, viscous properties of the fluid are usually negligible for cases where the flow is attached to the lifting surfaces. These fluid idealizations have proven useful for conventional aerodynamic system analysis and hence are employed here. Two areas where the inviscid fluid assumption merits care are turbulent entrainment into the high speed jet and recirculation in areas where the jet impinges on the ground. Both of these areas are beyond the scope of the present analysis. A method for approximately accounting for subcritical fluid compressibility effects is provided in the current method through a Prandtl-Glauert simularity transformation but this technique is not rigorously applicable to nonplanar configurations.

2.2 Boundary Conditions and Field Equations

Although the flowfield of the present problem is composed of two regions, the outer flow and jet flow, only the outer region requires attention since the jet will be assumed to be of infinitesimal thickness and have zero mass flow. Since the fluid in the outer region is by assumption inviscid and the upstream flowfield is uniform, the outer flow is irrotational and a velocity potential, ϕ, can be defined.

$$\vec{V} = \nabla\phi, \tag{2.2-1}$$

where $\vec{V}$ is the flow velocity.

Furthermore, since the fluid is incompressible the consideration of fluid continuity requires the velocity potential to satisfy Laplace's equation,

$$\nabla^2\phi = 0. \tag{2.2-2}$$

Equation (2.2-2) is the basic field equation for the jet flap-wing flowfield implying that all the tools of potential flow analysis, including the use of potential flow singularity distributions and superposition of basic solutions, can be employed to obtain solutions.

Boundary conditions must be specified for both solid bodies and the jet surfaces of the present problem. The solid surface boundary condition is the usual inviscid condition of tangential flow or,

$$\frac{\partial\phi}{\partial n} = 0 \tag{2.2-3}$$

where n is the coordinate normal to the wing surface. Additionally, it is assumed that there is an edge of the wing surface from which the flow departs smoothly and the usual trailing edge Kutta condition is applicable. At trailing edge locations where jet flaps originate, the initial jet angle, at which the flow departs the trailing edge, is specified.

To obtain the jet boundary condition the flow within the jet is assumed to be irrotational and the momentum within the jet remains constant along a streamwise section of the jet (i.e., no entrainment or cross-stream mixing of different energy jets). In a manner analogous to the two-dimensional development of Reference 10, the boundary conditions in three dimensions can be derived by considering the upper and lower surface pressure of the

jet element sketched in Figure 1. Since the jet boundaries separating the jet and outer flow are unable to sustain a pressure differential, the Bernoulli equation relates the lower pressure, p_ℓ, to the upper pressure, p_u, by

$$p_\ell - p_u = \tfrac{1}{2} \rho_J \left(u^2_{J_{us}} + u^2_{J_{uc}} - u^2_{J_{\ell c}} - u^2_{J_{\ell s}}\right) \tag{2.2-4}$$

where ρ_J is the jet fluid density and the jet velocity components are defined in Figure 1. The subscripts s and c refer to streamwise and cross-stream velocity components, respectively.

Since the flow within the jet is irrotational, the upper and lower jet speeds are related by,

$$u_{J_{us}} \left(R_s - \tfrac{\delta}{2}\right) = u_{J_{\ell s}} \left(R_s + \tfrac{\delta}{2}\right) \tag{2.2-5}$$

and

$$u_{J_{uc}} \left(R_c - \tfrac{\delta}{2}\right) = u_{J_{\ell c}} \left(R_c + \tfrac{\delta}{2}\right). \tag{2.2-6}$$

With the definition of mean jet speeds,

$$\bar{u}_{J_s} \equiv \frac{\left(u_{J_{us}} + u_{J_{\ell s}}\right)}{2} \tag{2.2-7}$$

and,

$$\bar{u}_{J_c} \equiv \frac{\left(u_{J_{uc}} + u_{J_{\ell c}}\right)}{2} \tag{2.2-8}$$

the upper and lower flow speeds can be expressed as,

$$u_{J_{us}} - u_{J_{\ell s}} = \frac{\bar{u}_{J_s}\, \delta}{R_s} \tag{2.2-9}$$

and,

$$u_{J_{uc}} - u_{J_{\ell c}} = \frac{\bar{u}_{J_c}\, \delta}{R_c} \tag{2.2-10}$$

Here R_s, R_c are the jet sheet radii of curvature and δ is the jet width which will later be set to zero. Now employing equation (2.2-4) with the above four equations yields,

$$p_\ell - p_u = \rho_J \delta \left(\frac{\bar{u}_{J_s}^2}{R_s} + \frac{\bar{u}_{J_c}^2}{R_c} \right) \qquad (2.2\text{-}11)$$

This is the basic dynamic boundary condition to be satisfied on the jet surfaces. As with previous three-dimensional jet flap analyses, such as References 11 and 12, the cross-stream curvature is presently ignored ($R_c >> R_s$) and then the jet pressure condition becomes,

$$p_\ell - p_u = \rho_J \delta \frac{\bar{u}_{J_s}^2}{R_s} . \qquad (2.2\text{-}12)$$

In addition to the above jet dynamic condition which specifies the pressure differential required to turn the jet momentum, a kinematic boundary condition of tangential flow on the jet surface is required, or,

$$\frac{\partial \phi}{\partial n} = 0 \qquad (2.2\text{-}13)$$

along the jet. This condition precludes entrainment of flow into the jet.

Boundary conditions have been specified on all solid surfaces and jet boundaries. Solid body boundary conditions are obviously applied at the known body surface. However the location at which the jet conditions are to be satisfied, the jet sheet position, is unknown. The unknown jet sheet shape presents a fundamental difficulty in the solution of nonlinear jet problems which is approached currently by employing an iterative scheme to successively approximate the jet shape while attempting to satisfy all of the above boundary conditions.

2.3 Method of Solution

With appropriate potential flow singularities and boundary conditions specified, the solution process consists of determining the singularity strengths and jet locations which satisfy the problem boundary conditions. In the present solution technique the solid surfaces and jet sheets are divided

into numerous finite elements each with specified singularity distribution of unknown strength. In addition, the positions of the jet finite elements are unknown and are determined during the solution process. Below, the distribution of singularities employed to represent solid bodies and jet sheets are described, and the general iterative scheme applied to determine solutions is presented. Also, the evaluation of aerodynamic loadings and forces from the converged solution is described.

2.3.1 Singularity Representation

The Laplacian velocity potential of the wing-jet flap flowfield facilitates the application of potential singularities to represent the solid bodies and jets. As in the formulation of the parent lifting surface theory, Reference 17, the appropriate singularity type to represent wings within the flowfield is a vortex sheet. This representation is proper since the lifting surface is a surface of tangential flow discontinuity so that the wing vortex strength, γ, is given by,

$$\gamma = u_{us} - u_{\ell s} \qquad (2.3.1\text{-}1)$$

where u_{us} and $u_{\ell s}$ are the upper and lower surface tangential flow speeds at the wing surface.

To determine the jet singularity type, consider the usual jet flap limit of vanishing jet width and infinite jet speed so that the jet mass flow approaches zero but the jet momentum remains finite. The sectional jet momentum coefficient is defined as,

$$C_J(y) = \frac{\rho_J \bar{u}_J^2{}_s \, \delta}{1/2 \, \rho U^2 c(y)} \qquad (2.3.1\text{-}2)$$

where U is the freestream flow speed and c is the local wing chord. Then the jet dynamic boundary condition can be rewritten as,

$$\frac{p_\ell - p_u}{1/2 \rho U^2} = \frac{C_J c}{R_s} \qquad (2.3.1\text{-}3)$$

Therefore, the jet surface is a sheet supporting a pressure differential with no normal flow, and consequently it may be represented by a vortex distribution. In a manner consistent with the derivation of the jet boundary condition, equation (2.2-12), if the cross stream component of the velocity at the jet boundary is ignored, the pressure differential across the jet sheet is,

$$p_{\ell} - p_u = \rho \bar{u}_{o_s} \gamma \qquad (2.3.1\text{-}4)$$

where $\bar{u}_{o_s}$ is the mean streamwise component of flow velocity.

Now the jet dynamic boundary condition can be expressed as

$$\frac{\gamma}{U} = \frac{1/2 c C_J}{R_s \bar{u}_{o_s}/U} \qquad (2.3.1\text{-}5)$$

and therefore relates the strength of the vortex sheet representing the jet flap to the local jet momentum, jet streamwise radius of curvature and local mean flow speed.

Now that wings and jets in the flowfield have been replaced by vortex sheet singularities, the entire flowfield can be specified by determining the strengths of the various vortex sheets. Three simultaneous integral equations, one for each of the three boundary conditions, can be written to define the wing and jet flap system. The tangential flow condition on the wing surfaces imposes the condition

$$\frac{\partial}{\partial n} \int_{-\infty}^{(x,y,z)_W} \left\{ \iint_{S_W} \gamma(\xi,\eta,\zeta) \frac{\partial}{\partial n}\left(\frac{1}{4\pi r}\right) dS + \iint_{S_J} \gamma(\xi,\eta,\zeta) \frac{\partial}{\partial n}\left(\frac{1}{4\pi r}\right) dS \right\} ds + \vec{U} \cdot \vec{n} = 0 \qquad (2.3.1\text{-}6)$$

Similarly the tangential flow condition on the jet gives,

$$\frac{\partial}{\partial n} \int_{-\infty}^{(x,y,z)_J} \left\{ \iint_{S_W} \gamma(\xi,\eta,\zeta) \frac{\partial}{\partial n}\left(\frac{1}{4\pi r}\right) dS + \iint_{S_J} \gamma(\xi,\eta,\zeta) \frac{\partial}{\partial n}\left(\frac{1}{4\pi r}\right) dS \right\} ds + \vec{U} \cdot \vec{n} = 0 \qquad (2.3.1\text{-}7)$$

Finally the jet dynamic boundary condition requires

$$\frac{2\gamma(x,y,z)}{U^2}\left[\iint_{S_W}\gamma(\xi,\eta,\zeta)\,\frac{\partial}{\partial n}\,\frac{1}{4\pi r}\,dS+\iint_{S_J}\gamma(\xi,\eta,\zeta)\,\frac{\partial}{\partial n}\,\frac{1}{4\pi r}\,dS+\vec{U}\cdot\vec{t}\right]=\frac{cC_J}{R(x,y,z)} \qquad (2.3.1\text{-}8)$$

where ξ,η,ζ are dummy integration variables and S indicates the surface over which the integration is performed.

The above three equations must be satisfied simultaneously to determine the wing and jet flap system. The solution of these equations is obtained numerically by employing finite-element techniques as described below. As mentioned previously, the principal difficulty involved in obtaining the solution is the unknown jet position.

2.3.1.1 Solid Body Singularities

Following the elementary vortex distribution (EVD) concept developed in References 12 and 17, the wing vortex singularities are represented in the present method by suitable functions with unknown coefficients. For example, the exact two-dimensional vorticity distribution for a flat plate airfoil indicates that the vortex strength at the airfoil leading edge varies in an inverse square root manner. This result is nonrigorously extended to the three-dimensional problem by specifying the vortex strength distribution,

$$\gamma(\xi)=\frac{2}{3}\,\gamma'\left[\left(\frac{\xi}{\ell}\right)^{-1/2}-\left(\frac{\xi}{\ell}\right)\right] \qquad 0\le\xi\le\ell \qquad (2.3.1.1\text{-}1)$$

where ξ is the distance measured from the wing leading edge and ℓ is the streamwise element length as illustrated in Figure 2. The unknown coefficient, γ', is determined for each leading edge element during the solution process.

Although singular vortex strength variation may occur at positions away from the wing leading edge, such as surface or jet angle discontinuities, experience with EVD methods indicate that the vortex strength behavior aft of the leading edge can be described accurately by piecewise linear distributions. These functions, often referred to as triangular distributions, are given by,

$$\gamma(\xi) = \begin{cases} \frac{\gamma'}{\ell_1}(\xi_1 + \ell_1) & -\ell_1 \le \xi_1 \le 0 \\ -\frac{\gamma'}{\ell_2}(\xi_2 - \ell_2) & 0 \le \xi_2 \le \ell_2 \end{cases} \qquad (2.3.1.1\text{-}2)$$

where ξ is the tangential distance measured along the wing camberline and ℓ_1 and ℓ_2 are the lengths of adjacent elements. The triangular distributions as well as the superposition of the two types of vorticity functions are illustrated in Figure 2. Application of combined inverse square root and triangular vorticity distributions have proven adequate for describing the vortex strengths of infinitely thin airfoils in two dimensions (Reference 15) and three dimensions (References 12 and 17). This combination is a higher order singularity representation than discrete vortex methods, such as vortex lattice techniques, and is not as restrictive in selection of collocation rules as lower order methods. Presently the location of the point where solid body boundary conditions are satisfied on each wing element is specified to be the element geometric center.

For unpowered wing sections, the trailing edge triangular vorticity distribution is forced to be zero thereby satisfying the Kutta condition of smooth departure of the flow and zero wing loading. The wing trailing vortex sheet of unpowered sections is assumed to extend downstream with a trajectory parallel to the freestream flow, whereas for powered wing sections the trailing vorticity is aligned with the deflected jet trajectory. The trailing edge condition for powered wing sections will be discussed subsequently.

Although the calculation of the induction of the leading edge and triangular elementary vortex distributions is conceptually simple, the resulting expressions are quite complicated. These induction expressions are derived in Reference 18 and are not repeated here. A farfield expansion of the velocity induction expressions has been employed in previous NPLS unpowered analyses to improve the efficiency of evaluating the influence of wing elements at control points. However as demonstrated by the results of Section 3.2, an inaccuracy has been discovered in these expansions and hence only the nearfield induction formulas have been employed in the present study.

2.3.1.2 Jet Sheet Singularities

Jet flap vorticity can be represented in a manner similar to the wing distributions by employing elementary vortex distributions. The only irregular behavior of the jet vorticity occurs at the wing trailing edge for jet angles different from the wing trailing edge angle. In two dimensions, the abrupt turning of the jet from the wing results in an exponential variation of vortex strength at the trailing edge. However, experience has indicated that this singularity in vortex strength can be adequately approximated by piecewise linear distributions. Consequently the entire jet flap sheet is represented in the NPLS method by triangular vorticity distributions (Equation (2.3.1.1-2)) as shown in Figure 2. At downstream infinity the jet flap vorticity approaches zero as the jet approaches an asympotic angle relative to the freestream and the jet radius of curvature approaches infinity. In previous EVD jet flap methods, References 12 and 15, the downstream jet behavior was represented by a decay function which originates at the furthest downstream jet element endpoint and extends to downstream infinity. In the present analysis, the downstream vorticity behavior is simply represented by forcing the jet vortex strength of the furthest downstream jet element to be zero as indicated in Figure 2.

2.3.2 Application of Wing Boundary Conditions

With the above specification of solid body singularity distributions, the influence of any wing element at any point in the flowfield can be calculated by integrating the differential form of the Biot-Savart Law. In order to simplify this integration process, the NPLS method restricts wing elements to individual planar surfaces (of course the wing surface is not necessarily planar). The results of the velocity induction integration, as given in an Appendix of Reference 18, are quite complex. All three velocity components are evaluated in the solution process and stored in the arrays $A_{u_{ij}}$, $A_{v_{ij}}$, and $A_{w_{ij}}$, where for example $A_{u_{ij}}$ gives the x-component of the induced velocity of a unit vortex strength distribution ($\gamma = 1$) of the jth wing element at the i^{th} point in space. The positions in space where the velocity induction are evaluated are generally wing and jet control points. Similarly the jet induction is evaluated and stored in the arrays $B_{u_{ij}}$, $B_{v_{ij}}$, and $B_{w_{ij}}$.

Employing finite element approximation, the wing boundary condition integral equation (Equation (2.3.1-6)) can be transferred into a set of simultaneous algebraic relations. The velocity at a wing control point is composed of the wing induced, jet induced and freestream components,

$$\vec{V} = \vec{V}_W + \vec{V}_J + \vec{U} \tag{2.3.2-1}$$

Using the influence coefficient formulation for the wing and jet induction, the velocity vector at the i^{th} wing control point becomes,

$$\vec{V}_i = \vec{I}(A_{u_{ij}} + B_{u_{ij}})\gamma'_j + \vec{J}(A_{v_{ij}} + B_{v_{ij}})\gamma'_j \tag{2.3.2-2}$$

$$+ \vec{k}(A_{w_{ij}} + B_{w_{ij}})\gamma'_j + \vec{U}$$

Consequently the tangential flow solid body boundary condition can be written as,

$$\vec{V}_i \cdot \vec{n}_i = 0 \tag{2.3.2-3}$$

or,

$$n_{x_i}(A_{u_{ij}} + B_{u_{ij}})\gamma'_j + n_{y_i}(A_{v_{ij}} + B_{v_{ij}})\gamma'_j$$

$$+ n_{z_i}(A_{w_{ij}} + B_{w_{ij}})\gamma'_j = -U_x n_{x_i} - U_y n_{y_i} - U_z n_{z_i} \tag{2.3.2-4}$$

The above matrix equation provides a number of equations equal to the number of wing control points. All terms in the equations are known for a given wing and jet geometry except the γ'_j coefficients, which specify the strength values of the wing and jet vorticity functions.

2.3.3 Application of Jet Boundary Conditions

The application of the jet flap dynamic boundary condition, Equation (2.3.1-5) within the finite element framework is integrally connnected to the iterative scheme employed to successively approximate the wing-jet flap system until a vorticity distribution and jet shape are determined which nearly satisfy all boundary conditions. The nonlinearity inherent to the jet dynamic condition is removed by employing values from the previous iteration.

In order to derive a finite element formulation of the jet dynamic boundary condition, the substitution $R = ds/d\theta$ is made in Equation (2.3.1-5) and both sides are integrated over the jet interval between the i^{th} and $(i+1)^{th}$

jet control points (see Figure 3). Then

$$\int_{S_i}^{S_{i+1}} \frac{\gamma \bar{u}_{o_S}}{U^2}\, dS = \frac{cC_J}{2} \int_{\theta_i}^{\theta_{i+1}} d\theta \qquad (2.3.3\text{-}1)$$

where the indices are defined in Figure 3, S is the arc length along the jet sheet and θ is the jet element angle relative to the horizontal axis. Assuming piecewise linear vortex strength variation along the jet sheet, the left side of the above equation can be integrated if the integrand is quasi-linearized by employing the previous iteration's value for $\bar{u}_{o_S}$. The integral of the right side of Equation (2.3.3-1) is simply the difference in the jet angle between two jet elements. The jet angle at any jet element for the ν^{th} iteration can be approximated by the jet angle during the previous, $(\nu\text{-}1)^{th}$, iteration and the normal velocity at the jet element (see insert of Figure 3),

$$\theta_i^{\nu} \cong \theta_i^{\nu-1} + \frac{V_{n_i}}{\bar{u}_{o_{S_i}}^{\nu-1}} \qquad (2.3.3\text{-}2)$$

where V_{n_i} is the velocity component normal to the jet element. This approximation becomes exact as the iteration process converges and V_{n_i} approaches zero. Of course the normal velocity, V_{n_i}, at the jet element is composed of wing and jet sheet induction as well as the freestream contribution. Employing the notation of Equation (2.3.2-4) for the induction of wing and jet vorticity distribution, the jet dynamic boundary condition can be written as

$$\left[\left(\frac{\gamma_{i-1}'^{\nu}}{8} + \frac{3\gamma_i'^{\nu}}{8}\right) \bar{u}_{o_{S_{i-1}}}^{\nu-1} \left(S_i^{\nu-1} - S_{i-1}^{\nu-1}\right) + \left(\frac{3\gamma_i'^{\nu}}{8} + \frac{\gamma_{i+1}'^{\nu}}{8}\right) \bar{u}_{o_{S_i}}^{\nu-1} \left(S_{i+1}^{\nu-1} - S_i^{\nu-1}\right)\right]$$

$$+ \frac{cC_J \gamma_j'^{\nu}}{2\bar{u}_{o_{S_i}}^{\nu-1}} \left[n_{x_i}(A_{u_{ij}} + B_{u_{ij}}) + n_{y_i}(A_{v_{ij}} + B_{v_{ij}})\right.$$

$$+ n_{z_i}(A_{w_{ij}} + B_{w_{ij}}) - n_{x_{i-1}}(A_{u_{(i-1)j}} + B_{u_{(i-1)j}})$$

$$\left. - n_{y_i}(A_{v_{(i-1)j}} + B_{v_{(i-1)j}}) - n_{z_i}(A_{w_{(i-1)j}} + B_{u_{(i-1)j}})\right]$$

$$= \frac{cC_J}{2}\left[-\theta_j^{\nu-1}+\theta_{j-1}^{\nu-1} - \frac{U_x n_{x_i}+U_y n_{y_i}+U_z n_{z_i}}{\bar{u}_{o_{s_i}}^{\nu-1}}\right. \tag{2.3.3-3}$$

$$\left. + \frac{U_x n_{x_{i-1}}+U_y n_{y_{i-1}}+U_z n_{z_{i-1}}}{\bar{u}_{o_{s_i}}^{\nu-1}}\right]$$

for jet elements not adjacent to the wing trailing edges.

At the wing trailing edge the jet angle is equal to the specified jet deflection, θ_{te}, and the integration of Equation (2.3.3-1) is performed from the wing trailing edge to the first element control point,

$$\int_{S_{te}}^{S_i} \frac{\gamma \bar{u}_{o_s}}{U^2}\, dS = \frac{cC_J}{2} \int_{\theta_{te}}^{\theta_i} d\theta. \tag{2.3.3-4}$$

Then the finite element formulation of the jet dynamic boundary condition is,

$$\left(\frac{3}{8}\gamma_i'^{\nu} + \frac{\gamma_{i+1}'^{\nu}}{8}\right)\bar{u}_{o_{s_{i-1}}}^{\nu-1}\left(S_i^{\nu-1} - S_{te}^{\nu-1}\right)$$

$$+ \frac{cC_J\gamma_j'^{\nu}}{2\bar{u}_{o_{s_i}}^{\nu-1}}\left[n_{x_i}(Au_{ij}+Bu_{ij}) + n_{y_i}(Av_{ij}+Bv_{ij})\right.$$

$$\left. + n_{z_i}(Aw_{ij}+Bw_{ij})\right] \tag{2.3.3-5}$$

$$= \frac{cC_J}{2}\left[-\theta_j^{\nu-1} + \theta_{te} - \frac{U_x n_{x_i}+U_y u_{y_i}+U_z u_{z_i}}{\bar{u}_{o_{s_i}}^{\nu-1}}\right].$$

The jet kinematic boundary condition is applied within the iterative solution scheme which attempts to continuously determine a jet shape so that there is no flow normal to the jet sheet. This condition is applied simply by requiring the local jet cant angle, θ, to be aligned with the local flow, ignoring the cross-stream component,

$$\theta_i^{\nu} = \text{ARCTAN}\left[\frac{\sum_{\text{wing}} A_{w_{ij}}\gamma_j'^{\nu} + \sum_{\text{jet}} B_{w_{ij}}\gamma_j'^{\nu} + U_z}{\sum_{\text{wing}} A_{u_{ij}}\gamma_j'^{\nu} + \sum_{\text{jet}} B_{u_{ij}}\gamma_j'^{\nu} + U_x}\right] \qquad (2.3.3\text{-}6)$$

Note that the y terms are omitted from the above relation. With the cant angle defined by Equation (2.3.3-6), the jet shape for each streamwise cut of the jet sheet is given by,

$$x_i^{\nu} = x_{te} + \sum_{k=1}^{i} \Delta S_k \cos \theta_k^{\nu} \qquad (2.3.3\text{-}7)$$

$$y_i^{\nu} = y_i^{o} \qquad (2.3.3\text{-}8)$$

and,

$$z_i^{\nu} = z_{te} - \sum_{k=1}^{i} \Delta S_k \sin \theta_k^{\nu}. \qquad (2.3.3\text{-}9)$$

Of course as the solution process proceeds from one iteration to the next, the jet/wing vortex strengths are updated resulting in flow which is no longer tangential to the jet sheet and therefore the redefinition of the jet shape is required during each iterative step.

2.3.4 Force Evaluation

At the completion of each iterative cycle, the load distribution, forces, and moments on each lifting surface are evaluated from the calculated vorticity distributions and jet locations. The pressure differential across a thin wing surface represented by a vortex sheet is given by application of the Bernoulli equation as,

$$p_{\ell} - p_u = \frac{\rho}{2}(u_u + u_{\ell})(u_u - u_{\ell}) \qquad (2.3.4\text{-}1)$$

where u_{ℓ} and u_u are the upper and lower surface flow speeds respectively, and ρ is the fluid density. The local flow velocity is obtained by summing the wing, jet flap and freestream contributions.

Nondimensionalizing by the freestream dynamic pressure, $1/2\rho U^2$, yields the

jump in pressure coefficient across the vortex sheet,

$$\Delta C_p = 2\left|\frac{\vec{u}}{U} \times \frac{\vec{\gamma}}{U}\right| = 2\left(\frac{\vec{u}}{U} \cdot \vec{t}\right)\frac{\gamma}{U}. \tag{2.3.4-2}$$

Of course this pressure force acts perpendicular to the lifting surface.

A special pressure force is applied at the leading edge of a thin wing within the elementary vortex distribution formulation. As noted previously, the flow at the leading edge is assumed to behave as though it turns around a thin two-dimensional flat plate. Consequently, an infinite vortex strength with corresponding infinite flow speed is present at the leading edge. This singular vorticity behavior results in an infinite negative pressure acting on the zero width leading edge thereby producing a finite force. The magnitude of the force can be evaluated by application of the Blasius force equation (see Reference 18 for example) to be

$$F_S = \frac{\pi}{9}\rho\ell\gamma'^2_{\ell e} \tag{2.3.4-3}$$

where F_S is the leading edge suction force per unit span, ℓ is the streamwise leading edge element length, and $\gamma'_{\ell e}$ is the coefficient of the leading edge vorticity distribution as defined in Equation (2.3.1.1-1). Nondimensionalizing the leading edge suction coefficient by the freestream dynamic pressure and local chord, c, yields the leading edge suction coefficient, C_S,

$$C_S = \frac{\pi}{2}\frac{\ell}{c}\left(\frac{\gamma'_{\ell e}}{U}\right)^2 \tag{2.3.4-4}$$

This suction acts tangentially to the airfoil leading edge surface.

A jet reaction force acts on each powered section of the wing in addition to the usual pressure force described above. The magnitude of the jet reaction force is equal to the jet momentum issuing at the trailing edge and the direction of the force is opposite to the initial jet inclination. Therefore the jet reaction force vector is,

$$\vec{f}_{JR} = \rho \tilde{u}_{J_s}^2 \delta(-\vec{i} \cos \delta_J + \vec{k} \sin \delta_J) \qquad (2.3.4\text{-}5)$$

where δ_J is the jet deflection angle relative to the horizontal axis. In nondimensional form the jet reaction force is,

$$\vec{C}_{f_{JR}} = C_J(y)(-\vec{i} \cos \delta_J + \vec{k} \sin \delta_J) \qquad (2.3.4\text{-}6)$$

where $C_J(y)$ is the section value of the jet momentum coefficient.

Now the sectional aerodynamic force coefficient, $\vec{C}_f$, can be determined by integration along the section camberline of the surface pressure differential in combination with leading edge suction force and jet reaction force

$$\vec{C}_f = \int_0^c \frac{\Delta C_p}{c} \vec{n} ds + C_S \vec{t} + \vec{C}_{f_{JR}} \qquad (2.3.4\text{-}7)$$

where $\vec{t}$ is the unit vector tangent to the leading edge surface. Sectional lift and drag coefficients are given by

$$\begin{aligned} C_\ell &= \vec{C}_f \cdot \vec{k} \cos \alpha - \vec{C}_f \cdot \vec{i} \sin \alpha \\ C_{d_i} &= \vec{C}_f \cdot \vec{i} \cos \alpha + \vec{C}_f \cdot \vec{k} \sin \alpha \end{aligned} \qquad (2.3.4\text{-}8)$$

The force acting on the wing excluding the jet reaction contribution is usually referred to as the circulation force C_{f_Γ} (which can be resolved into circulation lift C_{ℓ_Γ} and circulation drag $C_{d_{i_\Gamma}}$).

Similarly, the sectional rolling, pitching, and yawing moments (C_ℓ, C_m, C_n) are

$$C_\ell \vec{i} + C_m \vec{j} + C_n \vec{k} = \int_0^c \frac{\Delta C_p \vec{r} \times \vec{n} ds}{c^2} + \frac{C_S}{c} (\vec{r}_{\ell e} \times \vec{t}) + \frac{\vec{r}_{te} \times \vec{C}_{f_{JR}}}{c} \qquad (2.3.4\text{-}9)$$

where $\vec{r}$, $\vec{r}_{\ell e}$ and $\vec{r}_{te}$ are defined as,

$$\vec{r} \equiv (x-x_o)\vec{i} + y\vec{j} + z\vec{k} \qquad (2.3.4\text{-}10)$$

$$\vec{r}_{\ell e} \equiv (x_{\ell e}-x_o)\vec{i} + y\vec{j} + z\vec{k} \qquad (2.3.4\text{-}11)$$

$$\vec{r}_{te} \equiv (x_{te}-x_o)\vec{i} + y\vec{j} + z\vec{k} \qquad (2.3.4\text{-}12)$$

and x_o is the pitching moment reference location. The rolling and yawing moments are referenced to the x and z axes.

Total aerodynamic forces and moments are obtained by spanwise integrations of the sectional parameters. The three force components are non-dimensionalized by the reference area S. Pitching moment is non-dimensionalized by $S\bar{c}$, where $\bar{c}$ is the reference chord; while the rolling and yawing moments are non-dimensionalized by Sb, where b is the reference span. The three force components are computed from

$$C_L = \frac{1}{S}\sum \int_{span} c\, C_\ell \, d\eta \qquad (2.3.4\text{-}13)$$

$$C_{D_i} = \frac{1}{S}\sum \int_{span} c\, C_{d_i} \, d\eta \qquad (2.3.4\text{-}14)$$

$$C_Y = \frac{1}{S}\sum \int_{span} c\, C_y \, d\eta \qquad (2.3.4\text{-}15)$$

where η is the spanwise coordinate on each lifting surface and the finite summation (i.e., $\sum$) indicates that the integral is taken over each lifting surface. Integration for the total moment components requires that the moment center be specified. In the present method the moment center is assumed to be at $(x_{mc}, 0, 0)$. Hence the total moment components are

$$C_M = \frac{1}{S\bar{c}} \left\{ \sum \int_{span} \left[c^2 C_m - c(x_o - x_{mc})\vec{C}_f \cdot \vec{k} \right] d\eta \right. \qquad (2.3.4\text{-}16)$$

$$C_N = \frac{1}{Sb} \left\{ \sum \int_{span} c^2 C_n \, d\eta \right. \qquad (2.3.4\text{-}17)$$

$$C_R = \frac{1}{Sb} \left\{ \sum \int_{span} c^2 C_l \, d\eta \right. \qquad (2.3.4\text{-}18)$$

2.3.5 General Iterative Scheme

The components of the NPLS Jet Flap Analysis solution method have been described above by specifying the wing/jet singularity representations and application of appropriate boundary conditions. The iterative solution technique combines these various elements to produce a method of obtaining a set of wing/jet vortex strengths and jet sheet locations which satisfy the wing/jet boundary conditions. This iterative scheme, illustrated by the flow chart of Figure 4, begins with the input of the lifting surface coordinates and jet parameters including jet element spacing, jet trailing edge angle and section jet momentum coefficient. Also an initial jet sheet shape must be defined from which the successive approximation process originates. With this information the wing and jet elements are defined, control points located and surface normals calculated.

The second, third, and fourth steps of the solution process evaluate the aerodynamic influence coefficients, A_u, A_v, A_w, B_u, B_v, and B_w, and store the coefficients expressing the wing influence on wing control points for reuse in subsequent iterative cycles. For unpowered wing sections the trailing vortex influence is calculated and stored for reuse whereas the trailing vortex influence for powered wing sections is recalculated for each iterative cycle since the trailing vortex sheet follows the jet trajectory. The fifth solution step combines the various wing and jet influence coefficients into the set of algebraic equations which apply the wing tangential flow conditions (Equation 2.3.2-4) and the jet dynamic condition (Equations 2.3.3-3 and 2.3.3-5). In the succeeding step the matrix equation is solved using a Gaussian triangularization technique to yield the strengths of the vortex sheets representing the wing and jet.

Determination of the wing and jet vortex strengths completes the iterative cycle and hence a test is performed to indicate the convergence of the process toward a solution which satisfies the appropriate boundary conditions. Two measures of convergence, average velocity normal to the sheet and maximum velocity normal to the jet, indicate the level of compliance of the current solution with the jet tangential flow boundary condition. Presumedly the wing tangential flow and jet dynamic conditions will be satisfied if the jet sheet is aligned with the local flow for a set of vortex strengths

determined by immediately preceeding steps. Another indication of the solution convergence is provided by the change in calculated forces on the wing surfaces between iterative cycles. A force evaluation for the jet and wing solution is performed for each iterative cycle as described in the previous section. Although comparison of the wing force coefficients calculated in successive steps indicates solution progress, the internal program decision logic regarding the requirement for additional iterative cycles is based on the jet normal velocity component. If a specified maximum jet normal flow is exceeded, the iterative process is repeated beginning with the application of the jet tangential flow boundary condition, Equations (2.3.3-7) to (2.3.3-9), to determine an updated jet location. Then the solution scheme proceeds with step three as indicated in Figure 4. Other solution progression options at the convergence test step include termination of the iterative process because the solution has sufficiently converged (as measured by the jet normal flow), termination because a specified number of iterative cycles have been exceeded, or storage of solution variables of a partially converged solution so that the process may be resumed without repeating initial iterative cycles.

2.4 Ground Effect

The ground effect problem is analyzed in the present method using a mirror image technique. This technique effectively places a stream-surface coincident with the ground plane. The mirror image (Figure 5) is treated exactly like another lifting system or jet except that each element on the image has the same vorticity strength (but opposite sign) and distribution as the corresponding element on the "real" wing or jet. Hence the number of algebraic equations employed to determine the vortex strengths need not be doubled, but instead each influence coefficient must include the influence of the corresponding image vortex element. Otherwise the solution is obtained in exactly the same manner as for any free-air solution.

The present method is ideally suited to the ground effect problem because of the highly nonplanar and nonlinear nature of the problem. It has been recognized that flight in ground proximity is not usually parallel to the ground plane, and the nonplanar nature of the present method allows the proper orientation between the lifting system, the ground, and the freestream to be

simulated. This is illustrated in Figure 5 where the flight path angle (γ) and attitude angle (θ) are shown.

2.5 Modeling of Jet Impingement on the Ground Plane

An important fluid dynamics phenomenon influencing many powered lift systems operating in close proximity to the ground is the complex flow pattern associated with impingement of the propulsive jet on the ground plane. In general jet impingement results in separation of the flow from the ground plane with recirculating regions below the wing and hence is dominated by viscous influences which are beyond the scope of the present analysis. However, a simple jet impingement model is incorporated within the NPLS Jet Flap Analysis program. As illustrated in Figure 6, the jet sheet is automatically truncated within the impingement model. First, the jet element intersecting the ground plane and all jet elements further downstream are temporarily discarded. Next, the furthest downstream jet element which does not pass through or below the ground plane, is linearly extrapolated to intersect the ground plane. The interval between the last "regular" element and the ground intersection is divided equally among the temporarily discarded jet elements to avoid indexing complications within the computer code. This forms the extrapolated jet sheet segment. Once an element has been truncated for any iterative step, it does not revert to regular status during subsequent steps, but instead remains part of the extrapolated segments.

A potential difficulty with the impingement model arises when an unrealistic velocity is calculated for the furthest downstream jet element before the jet truncation. Extrapolation to the ground plane of an unrealistic cant angle can cause a final jet element of excessive length running upstream for a large distance before intersecting the ground plane whereas a single unrealistic jet cant angle for a nonimpingement case will usually be of minor impact since only a single fixed length jet element is influenced.

2.6 Compressibility Effects

Although the basic mathematical model developed here assumes incompressible flow, fluid compressibility effects can be included approximately using the compressible form of Laplace's equation,

$$(1-M^2)\frac{\partial^2\phi}{\partial x^2} + \frac{\partial^2\phi}{\partial y^2} + \frac{\partial^2\phi}{\partial z^2} = 0 \qquad (2.6\text{-}1)$$

The Prandtl-Glauert transformation is used to transform the equation to an equivalent incompressible flowfield. That transformation is

$$x_o = \frac{x}{\sqrt{1-M^2}}, \quad y_o = y, \quad z_o = z \qquad (2.6\text{-}2)$$

so that Equation (2.6-1) becomes Laplace's equation (Equation (2.2-2)) in the (x_o, y_o, z_o) system. Equations (2.6-1) and (2.6-2) indicate that the compressible flow problem is solved in the same manner as the incompressible problem, except that the streamwise coordinates (i.e., x) are stretched by the factor $1/\sqrt{1-M^2}$ (or $1/\beta$).

The vortex solution (γ_o) obtained in this manner must be transformed back to the compressible flow. In linearized lifting surface theory the transformation is made by expressing the pressure jump coefficient in terms of the vortex strength, which in turn can be expressed in terms of the u-perturbation velocity, as

$$C_{p_o} = 2\frac{\gamma_o}{U} = 2\frac{\Delta u}{U} = 2\frac{\Delta\left(\frac{\partial\phi}{\partial x_o}\right)}{U} \qquad (2.6\text{-}3)$$

Since the velocity potential is the same at corresponding points in the compressible and incompressible flows, the only transformation is to x_o, so the resulting transformation for the pressure jump coefficient is

$$\Delta C_p = \frac{\Delta C_{p_o}}{\beta} \qquad (2.6\text{-}4)$$

Strictly, Equation (2.6-4) applies only to linearized lifting surface theory since in nonlinear theory Equation (2.6-3) does not apply. In nonlinear theory

$$C_{p_o} = \left(2\frac{\vec{V}}{U}\cdot\vec{t}\right)\frac{\gamma_o}{U} = 2\left(\frac{\vec{V}}{U}\cdot\vec{t}\right)\frac{\Delta\left(\frac{\partial\phi}{\partial s_o}\right)}{U} \qquad (2.6\text{-}5)$$

where $\vec{V}$ is the local surface velocity vector and $\vec{t}$ is the unit tangent vector. Equation (2.6-5) is derived in Section 2.3.4. Since $\vec{V}$ includes velocity components other than u, and s_o (the tangential coordinate) is not necessarily coincident with x_o, the transformation cannot be made.

However, for high subsonic Mach number configurations there are generally only small deviations between s_o and x_o, so Equation (2.6-4) is a reasonable approximation. This approximation has been made in the present method and consequently the pressures on all wing elements (both leading edge and triangular vorticity distribution types) are scaled according to Equation (2.6-4).

3. CALCULATED RESULTS

In this section computed examples are presented which were obtained using the NPLS Jet Flap Analysis. A discussion of some general solution characteristics is followed by a description of calculated results for both powered and unpowered wings. Emphasis is currently placed on the ground effect problem since this is the most difficult case to analyze and is the case for which the unique qualities of the NPLS Jet Flap Analysis are of significant value.

3.1 Solution Properties

Before discussion of calculated results for specific configurations, an examination of the general numerical characteristics of the present analysis will be presented. The properties of solutions for unpowered wings are discussed in Reference 17 and therefore are addressed only briefly here. Figure 7 indicates the sensitivity of the calculated lift, drag, and moment to the number of chordwise and spanwise element divisions for an unpowered, rectangular, aspect ratio six wing with flat plate airfoil section. The increments in aerodynamic coefficients, relative to a 20 x 20, 400-element calculation, shown in Figure 7, indicate typical finite element analysis sensitivity to element spacing. Calculated lift is approximately equally dependent on the number of spanwise and chordwise divisions whereas the drag variation is most directly influenced by the chordwise spacing. Pitching moment about the quarter-chord predictions show the largest sensitivity to element spacing. Although there is significant variation in calculated coefficients apparent in Figure 7, the convergence characteristics of the NPLS method are quite adequate for basic aerodynamic analysis.

Many of the numerical characteristics of the analysis for unpowered configurations are anticipated to transfer to cases of wings with jet flaps attached and therefore a more limited examination of element spacing has been conducted for the powered case. Figure 8 shows the calculated lift, drag, and pitching moment variation with number of spanwise divisions for the same wing as above but with a jet flap. Lift and pitching moment sensitivities are of the same order as the unpowered case (Figure 7), but the drag predictions display more sensitivity to the number of spanwise divisions than the corresponding unpowered results. The convergence characteristics shown in Figure 8 for

drag (which is generally recognized to be more difficult to predict than lift) are judged to be satisfactory for the present level of development.

The iterative scheme required to solve the nonlinear jet flap problem introduces an additional dimension to the discussion of numerical properties of the NPLS Jet Flap Analysis. Figure 9 illustrates the sensitivity of jet shape solution convergence to the distribution of spanwise element spacing. The tip concentrated, unequal spanwise spacing, suggested in Reference 17 for unpowered wings, results in oscillation of the jet sheet shape near the wing tip as shown in the upper part of Figure 9. In contrast, application of equal spanwise spacing results in a well behaved solution which converges to a final state within a few iterations as indicated in the lower part of Figure 9.

The behavior of the calculated circulation lift is shown in Figure 10 for the same wing (with equal spanwise spacing) as a function of iterative cycle number. It is apparent from the results of Figure 10 that the calculated lift value for the lower jet angle case ($\delta_j = 30°$) converges rapidly and smoothly while the larger jet angle configuration ($\delta_j = 60°$) displays questionable convergence toward a final value. Generally NPLS jet flap solutions converge less rapidly for cases with higher jet angles and higher jet momentum coefficients compared to similar wings with lesser jet angles and momentum coefficients. Other configuration parameters which experience has shown to decrease the rate of solution convergence include close proximity to the ground and spanwise discontinuities in jet angle, flap angle or jet momentum.

3.2 Calculated Results for Unpowered Lifting Systems

The major emphasis of the present study was intended to be on the calculation of the aerodynamic characteristics of powered wings in ground effect. However, in the course of development of the jet flap version of the NPLS program, an inaccuracy was discovered which impacts the unpowered cases previously considered in Reference 14. Therefore, updated results will be presented for the configurations anlayzed earlier.

The inaccuracies discovered during the present study were present in the farfield expansion of the exact induction expressions for the triangular and

leading edge elementary vortex distributions. A computational efficiency feature was present in the initial NPLS analysis to switch from exact near-field expressions for velocity induction of an EVD to simpler, less time consuming farfield mathematical expansions of the induction at large distances from the influencing element. The switchover point was determined from studies such as illustrated in Figure 11 where the increment in calculated lift is shown as a function of the cutoff distance. However, the farfield expansions have been shown to introduce a significant inaccuracy into computed NPLS results for ground effect cases. Pending the development of more adequate farfield velocity induction expansions all NPLS results of this report were obtained employing only the nearfield formulas.

Several cases previously analyzed with the NPLS method have been recomputed and the present as well as original results are given in Figures 12 to 18. Additionally, aerodynamic coefficients calculated using the NASA Ames Research Center Potential Flow Analysis (POTFAN), which are given in Reference 9, are also indicated.

Lift augmentation ratios predicted for a rectangular aspect ratio six wing with a flat plate airfoil section at ten degrees angle of attack are presented in Figure 12 as a function of the distance between the wing leading edge and the ground plane. All of the thin wing prediction methods agree well except for the original NPLS result which has been demonstrated to be inaccurate. The thick wing analysis result which has been obtained using two versions (References 19 and 20) of the Douglas Aircraft Company Three-Dimensional Neumann Analysis, indicates a higher lift augmentation than the thin wing representations. This relation between thick and thin wing predicted lift in ground effect is contrary to the usual concept of the effect of wing thickness in ground effect. The often stated negative lift or "suck down" influence of section thickness is not verified by the results of Figure 12.

Results for a second rectangular planform wing are given in Figure 13 where the wing lift slope is presented as a function of ground height for an aspect ratio equal to four case. The analytically derived lift slopes were calculated assuming a linear lift curve between zero and one degree angle of attack.

Current NPLS and POTFAN results agree well with the experimental data even though the test program employed a 22-percent thick section. Evidently the thickness and viscous effects canceled for the experimental values obtained in the study of Reference 21.

Lift and drag characteristics for a final rectangular wing are given in Figures 14 to 17. For this final rectangular configuration, steady state as well as quasi-steady ascent and descent cases were analysed. As discussed further in Reference 14, the quasi-steady approximation to the ground approach problem includes the proper orientation of the lift system to the ground but ignores the flight path history of the complete dynamic transient case. Figure 14 presents the lift and drag, referenced to the freeair values, of an aspect ratio seven rectangular wing with flat plate section as predicted by the present NPLS analysis. Figure 15 gives the corresponding values of the same aspect ratio seven wing with a 40-percent chord flap deflected 60 degrees in order to approximately simulate a powered high lift system with rearward section loading. The present NPLS results are in close agreement with POTFAN predictions of Reference 9 for the same configurations. Furthermore, the relation between present NPLS ascent and descent lift values are in agreement with physically intuitive arguments whereas the original NPLS values were in conflict. Figures 16 and 17 provide a comparison of POTFAN, Boeing Advanced Panel Code (method of Reference 22 applied by R. T. Medan) as well as both present and original NPLS results. Clearly the current results of all three methods agree favorably for the quasi-steady motion of the aspect ratio seven wing.

Results for a final unpowered wing are presented in Figure 18. Here the increment in angle of attack due to ground proximity as a function of aircraft lift coefficient is presented for a typical transport wing with a five-degrees takeoff flap deflection. The ground height for each wing incidence for the transport wing case is the ground separation for which the main gear contact the ground and therefore correspond to the takeoff rotation of aircraft. Although somewhat lower than the original NPLS results, present NPLS results appear to agree with the wind tunnel data somewhat more closely than the POTFAN predictions.

3.3 Calculated Results for Powered Lifting Systems — Basic Configurations

To examine the aerodynamic characteristics predicted by the NPLS Jet Flap Analysis for a basic configuration, a rectangular planform, aspect ratio equal to six wing was selected and Figures 19 to 28 give the results of the study of this basic wing with jet flap. Out of ground effect lift curves and drag polars for three jet deflections are presented in Figures 19 and 20 for the flat plate wing section. Similar results are shown in Figures 21 and 22 for the wing with a full span forty-percent chord mechanical flap. A uniform strength jet with a momentum coefficient of 1.0 is applied to all these aspect ratio equal to six cases. Also shown in Figures 19 to 22 are linear analysis predictions obtained using the method of Reference 12. For these out of ground effect cases only minor differences are observable between the present nonlinear analysis calculations and the linear method results. Largest differences between the linear and nonlinear results occur, as anticipated, for the mechanical flap cases and high jet deflections.

Results indicating the calculated influence of the ground on the basic aspect ratio six wing are shown in Figures 23 to 28. Jet centerline trajectories and spanwise load distributions for the flat plate section wing are displayed for the three jet deflections in Figures 23, 24, and 25. As anticipated, the freeair jet trajectory is below the steady state ground effect jet path and also the descent and ascent cases are the upper and lower bounds of the jet trajectories. Lift and drag variation with ground height is presented in Figure 26 for the unflapped wing with a jet deflection of thirty degrees in steady flight. Figures 27 and 28 are the ground effect counterparts of the lift curve and drag polar of Figures 19 and 20 indicating all three jet deflection angles and steady state, ascent and descent cases. It is apparent from Figures 27 and 28 that the nonlinear analysis ground effect aerodynamic characteristics are significantly different from the linear solution values, especially when impingement of the jet on the ground plane occurs. Some of the NPLS results shown in Figure 28 were obtained from marginally converged numerical solutions and should be regarded only qualitatively. Nevertheless, the importance of inclusion of nonlinear analysis aspects and jet impingement in ground effect calculations is evident from these results even though the present impingement model is a relatively primitive representation of a complex flow.

3.4 Calculated Results for Powered Lifting Systems — Comparison with Test Data

Three powered lift configurations for which ground effect test results exist have been selected for analysis using the NPLS Jet Flap Analysis program. The comparison of the analytical and experimental predicted aerodynamic characteristics will be discussed in the order of increasing complexity.

The simplest configuration studied is the semispan test model of Reference 23 which incorporates a relatively thin jet issuing from the trailing edge of a rectangular aspect ratio 8.3 wing. Although a small chord mechanical flap was employed to turn the jet flap, it was judged to have little aerodynamic influence and thus has been ignored in the analysis model. Also, even though the flap setting was 60 degrees, observations estimated the actual trailing edge jet angle to be 55 degrees and therefore this lesser value was accepted for input into the NPLS program. The experimental data of Reference 23 were obtained without boundary-layer control on the fixed ground board. Predicted and measured circulation lift augmentation ratios are compared in Figure 29 for the configuration of Reference 23. Both predicted and measured trends in lift augmentation indicate a slight favorable ground influence as the ground is approached followed by a significant loss in lift for small ground separations. However, in comparison with the experimental results, the NPLS method indicates a larger favorable effect and smaller ground separation before a negative effect is predicted. Apparently the NPLS model does not sufficiently account for the jet impingement interaction for the configuration of Reference 23 at ground heights less than two chords.

A second, somewhat more complex configuration incorporating a large fuselage and a swept, tapered wing was tested in Reference 24. The NPLS analysis idealization of this configuration is illustrated by the wing element boundaries, shown in plan, side, and aft views of Figures 30, 31 and 32. The fuselage in this case was represented by an extension of the wing to the configuration centerline. Note that the trailing edge of the wing is straight and unswept which experience has indicated is a favorable influence on NPLS solution convergence, compared to broken or swept trailing edges. Figure 33 provides a comparison between measured and predicted aircraft total lift as a function of jet momentum coefficient for the freeair case. The NPLS method

appears to overpredict the aircraft lift at low jet momentum coefficient values and under predicts the lift at high jet momentums for the out-of-ground effect case. Variation of aircraft lift as a function of wing leading edge ground height is given in Figures 34 and 35 for two different jet momentum coefficients. Although the NPLS Jet Flap Analysis predictions indicate similar trends as the data, the NPLS lift values are significantly lower and the negative effect of the ground on lift appears to be overpredicted. Influences which may account for the discrepancy between experimentally and analytically derived lift values include the large aircraft fuselage and wing section thickness not included in the analysis.

The final, and most complex, configuration anlayzed presently with the NPLS Jet Flap Analysis program is the NASA C-8/A Augmentor Wing Aircraft. This configuration, described in Reference 25, employed strong jet blowing between two flap surfaces to form an augmentor wing high lift system over the inboard part of the wing. Also the ailerons were deflected with trailing edge blowing and a small amount of blowing was applied over the fuselage near the wing trailing edge. The initial NPLS idealization employed to analyze the C-8/A aircraft is illustrated by the plan, side, and aft views of Figures 36, 37, and 38. Several alternative representations involving simplifications were examined and found to have jet flap solution characteristics somewhat improved over the original, most complex representation. None of the wing representations for the C-8/A aircraft displayed solution convergence properties that were as well behaved as the simpler experimental configurations discussed previously. The most simplified analysis idealization of the C-8/A aircraft is shown in Figures 39, 40 and 41. This simplified representation employed a constant camber wing section with constant flap/aileron deflection and jet momentum.

Figure 42 presents the flight test measurements of Reference 26, linear analysis predictions and NPLS results for the C-8/A configuration operating out of ground effect. Both the complex and simplified NPLS representation results are indicated in Figure 42. Similar lift curve estimates for the C-8/A operating at a ground height of one wing chord are given in Figure 43. Only the simplified NPLS representation lift prediction is available in Figure 43 since the complex representation solutions failed to converge

adequately. None of the analytical lift curves of Figures 42 or 43 compare well with the test values and the only positive correlation is the decrease in lift curve slope of the ground effect case relative to the freeair result for both flight test and simplified NPLS predictions. Clearly additional study is indicated before such a complex configuration can be analyzed routinely by the present NPLS Jet Flap Analysis.

4. EXTENSIONS TO THE NPLS JET FLAP ANALYSIS

Four areas of extension are suggested by current experience with the NPLS Jet Flap Analysis. First, aspects of the basic technique are amenable to improvements in computational efficiency. For example, the reintroduction of farfield velocity induction function, without the previously encountered inaccuracy, would significantly decrease the calculation time requirements.

A second area of NPLS development involves improvements to the solution convergence characteristics. Numerical relaxation of the solution may significantly speed the rate of convergence of the jet flap solution toward a final value. Additionally, relaxation may expand the class of configurations for which solutions may routinely be obtained. Relaxation could be applied to the jet position and/or the vortex strengths. Other numerical improvements, such as the smoothing of jet sheets at spanwise discontinuities of jet deflection, jet momentum or wing trailing edge characteristics, should be investigated to improve the iterative solution behavior.

The third area of analysis improvement involves development of a more realistic jet impingement model. The present idealization of the jet intersection with the ground plane is only a first approximation of the actual flow phenomenon and is a source of solution difficulty for some configurations. Numerical experimentation with various impingement representations may indicate the most suitable model within the scope of the present inviscid analysis.

A final aspect of suggested NPLS Jet Flap Analysis improvement entails an increase in complexity of configurations which can be represented within the analysis. For example, incorporation of a fuselage representation within the finite element analysis could be accomplished either by paneling the body with appropriate singularities or by an approximate slender body model representation. The iterative nature of the jet flap solution technique results in significant increased time requirements for additional analysis elements and therefore an approximate body representation may be appropriate.

5. CONCLUSIONS

An advancement in the technology to predict aerodynamic characteristics of powered lift systems operating near the ground has been achieved through the development of a nonlinear, nonplanar three-dimensional jet flap analysis. The application of an iterative technique to solve the jet flap problem has been successfully demonstrated in three dimensions. However, the present study is considered to be only another step in the systematic development of powered lift system prediction methodology and further development has been indicated.

The development of the basic finite element jet flap computer analysis is complete including an efficient program code and a capability to input complex configurations. Solution qualities have been examined and demonstrated to be adequate for many cases. However, certain configuration characteristics, including spanwise discontinuities in flap deflection, jet angle or jet momentum, tend to degrade the solution rate of progression toward a final converged result.

Apparent contradiction between intuitive concepts and NPLS predictions previously reported for unpowered wings in quasi-steady ascent and descent has been resolved by removing an inaccuracy in the previous lifting surface theory implementation. Results obtained with the current version of the analysis agree well with other thin wing analysis methods for unpowered lift systems.

Calculations employing the present method have indicated that linear and nonlinear analysis predictions agree well for flat plates with jet flap wings operating in freeair but may differ significantly for complex wings or for wings in close ground proximity. Also, calculations have revealed a significant importance of jet impingement on the ground plane to the prediction of ground effect on powered lift system characteristics. Apparently the perfection of a more adequate jet impingement model would facilitate more reliable ground effects predictions.

6. IMPLEMENTATION OF THE ANALYSIS

The Nonplanar Lifting Systems (NPLS) Method and computer program were developed under the Independent Research and Development program of the McDonnell Douglas Corporation. The NPLS computer program is proprietary to the McDonnell Douglas Corporation (MDC) and its distribution and use is limited to U.S. Government Agencies only.

The user's manual for the NPLS computer program has been issued as a separate MDC report (Reference 27) subject to the above limitation.

7. REFERENCES

1. Koning, C. Influences of the Propeller on Other Parts of the Airplane. Aerodynamic Theory, Vol. IV, Springer Verlag, Berlin. 1935.

2. Graham, E.W., Lagerstron, P.A., Licher, R.M., and Beane, B.J. A Preliminary Theoretical Investigation of Effects of Propeller Slipstream on Wing Lift. Douglas Aircraft Company Report SM-14991. 1953.

3. Rethorst, S.C. Aerodynamics of Nonuniform Flows as Related to an Airfoil Extending Through a Circular Jet. Journal of Aero. Sci., Vol. 25, No. 1. 1958. pp. 11-28.

4. Ribner, H.S., and Ellis, N.D. Theory and Computer Study of a Wing in a Slipstream. AIAA Paper No. 66-466. 1966.

5. Mendenall, M.R., Dillenius, M.F.F., and Spangler, S.B. Calculation of Aerodynamic Characteristics of STOL Aircraft with Externally-Blown-Jet-Augmented Flaps. AIAA Paper No. 73-83. 1972.

6. Lan. C.E. An Analytical Investigation of Wing-Jet Interaction. NASA CR-138140. 1974.

7. Shollenberger, C.A. Three-Dimensional Wing/Jet Interaction Analysis Including Jet Distortion Influences. J. of Aircraft, Vol. 12, No. 9. 1975.

8. Shollenberger, C.A. A Wing and Jet Interaction Analysis Based on a Doublet Singularity Formulation. McDonnell Douglas Report No. MDC J7421. 1977. (Restricted distribution)

9. Shollenberger, C.A. Analytical Study of STOL Aircraft in Ground Effect - Part II. Nonplanar,Nonlinear Method Applicable to Three-Dimensional Jets of Finite Thickness. NASA CR 152088. 1978.

10. Spence, D.A. The Lift Coefficient of a Thin, Jet-Flapped Wing. Proc. Roy. Soc., A. Vol. 238. 1956.

11. Maskell, E.C. and Spence, D.A. A Theory of the Jet Flap in Three Dimensions. Proc. of Roy. Soc. A. 251, 407. 1959.

12. Lopez, M.L. and Shen, C.C. Recent Developments in Jet Flap Theory and Its Application to STOL Aerodynamic Analysis. AIAA Paper No. 71-598. 1971.

13. Lissaman, P.B.S. Analysis of High Aspect Ratio Jet Flap Wings of Arbitrary Geometry. AIAA Paper No. 73-125. 1973.

14. Goldhammer, M.I., Crowder, J.P., Smyth, D.N. STOL Aircraft Transient Ground Effects - Part I. Fundamental Analytical Study. NASA CR 137766. 1975.

15. Halsey, N.D. Methods for the Design and Analysis of Jet-Flapped Airfoils. J. of Aircraft Vol. 11, No. 9. 1974.

16. Davenport, F.J. Singularity Solutions to General Potential Flow Airfoil Problems. Boeing Report D6-7202. 1963.

17. Goldhammer, M.I. A Lifting Surface Theory for the Analysis of Nonplanar Lifting Systems. AIAA Paper No. 76-16. 1976.

18. Goldhammer, M.I. Nonplanar Lifting System Method. McDonnell Douglas Report No. MDC J6985. 1976. (Restirctcd distribution)

19. Hess, J.L. Calculation of Potential Flow about Arbitrary Three-Dimensional Lifting Bodies. McDonnell Douglas Report No. MDC J5679-01. 1972.

20. Friedman, D.M. A Three-Dimensional Lifting Potential Flow Program. McDonnell Douglas Report No. J6182. 1974. (Restricted distribution)

21. Saunders, G.H. Aerodynamic Characteristics of Wings in Ground Proximity. M. Sc. Thesis, Dept. of Aeronautics and Astronautics, Massachusetts Institute of Technology. 1963.

22. Johnson, F.T., and Rubbert, P.E. Advanced Panel-Type Influence Coefficient Methods Applied to Subsonic Flows. AIAA Paper 75-50. January, 1975.

23. Vogler, R.D. and Turner, T.R. Wind-Tunnel Investigation at Low Speeds to Determine Flowfield Characteristics and Ground Influence on a Model with Jet-Augmented Flaps. NACA TN 4116. 1957.

24. Butler, S.F.J., Guyett, M.B., and Moy, B.A. Six-Component Complete Models with Variation of Aspect Ratio, Dihedral, and Sweepback, Including the Influence of Ground Proximity. ARC R&M No. 3441. 1967.

25. Ashleman, R.H. and Skavdahl, H.J. The Development of an Augmentor Wing Jet STOL Research Airplane (Modified C-8/A). NASA CR-114503, Vol. 1. 1972.

26. Wingrove, R.C. Parameter Estimation of Powered-Lift STOL Aircraft Characteristics Including Turbulence and Ground Effects. NASA TMX-62,382. September, 1974.

27. Shollenberger, C.A. and Smyth, D.N. Nonplanar Lifting Systems Jet Flap Analysis Method — User's Manual. McDonnell Douglas Report No. MDC J7770. 1978.

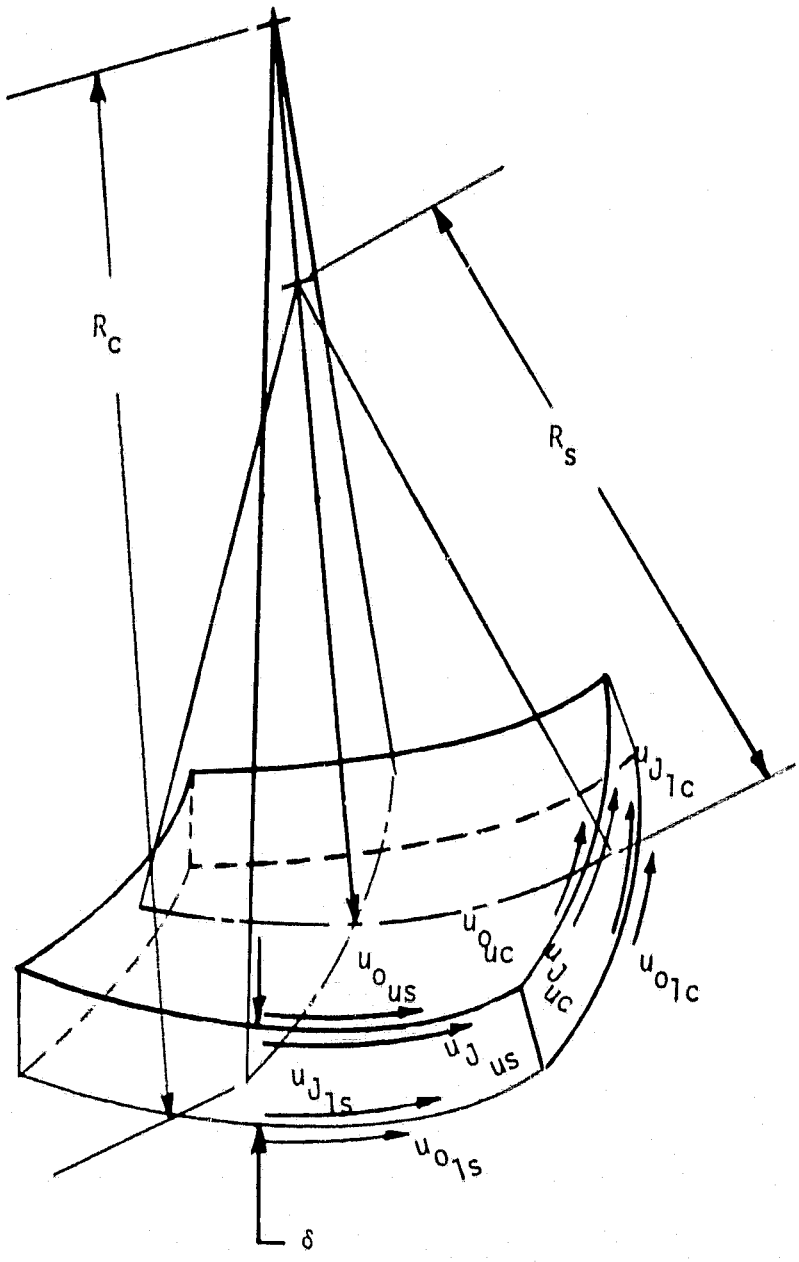

Figure 1. Element of Jet Sheet

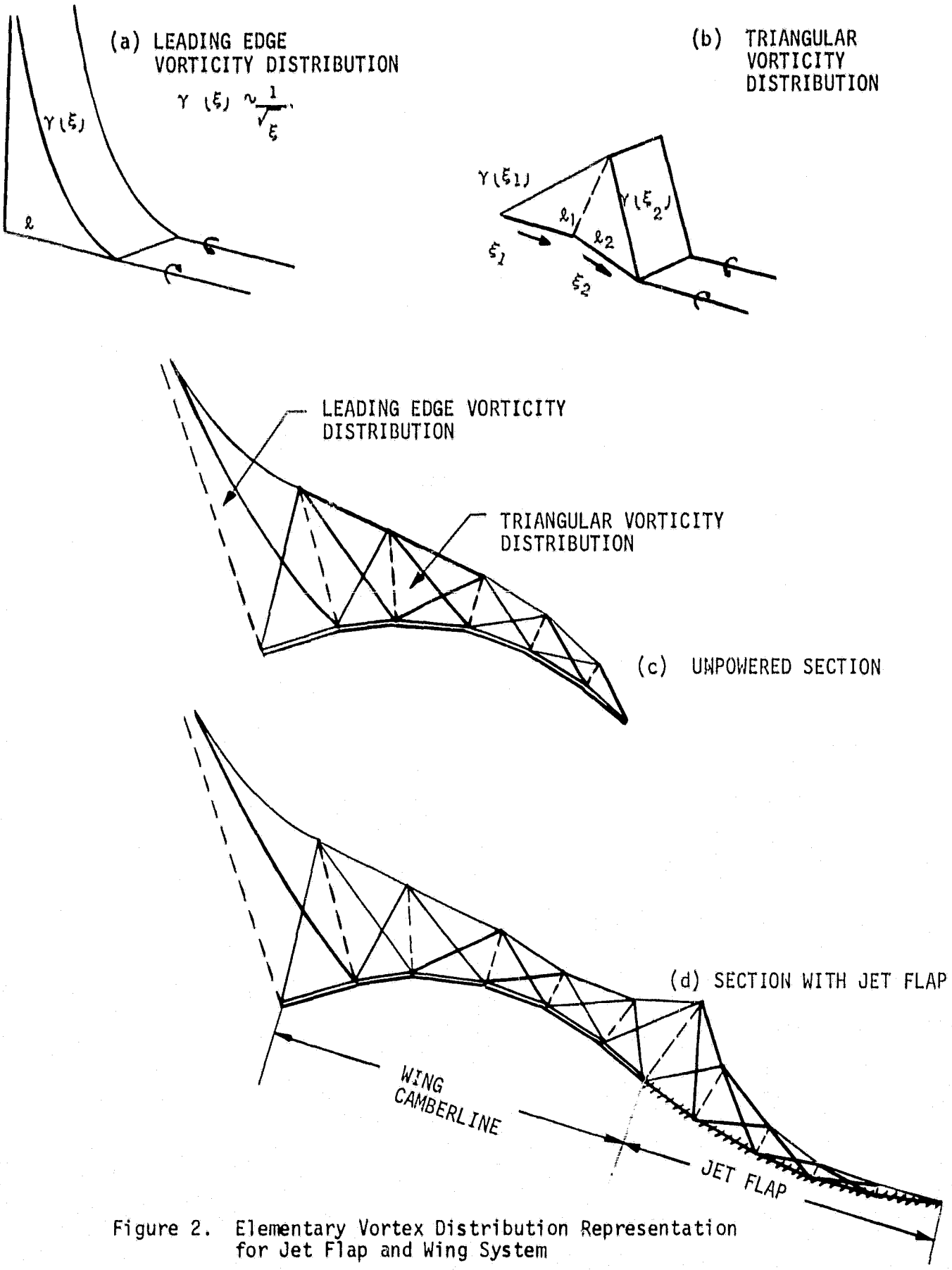

Figure 2. Elementary Vortex Distribution Representation for Jet Flap and Wing System

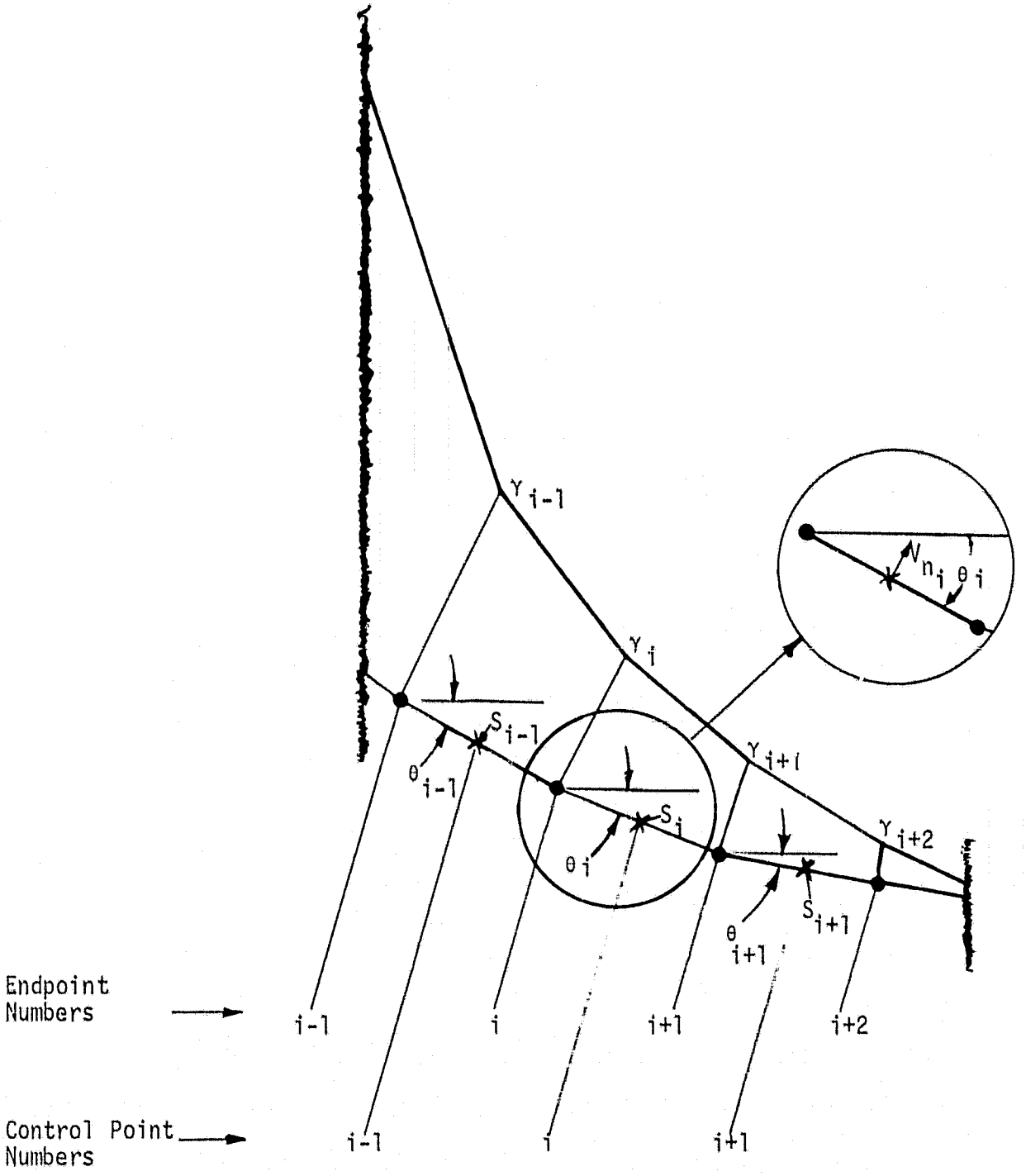

Figure 3. Geometrical and Indexing Arrangement For A Streamwise Section Of The Jet Flap Sheet

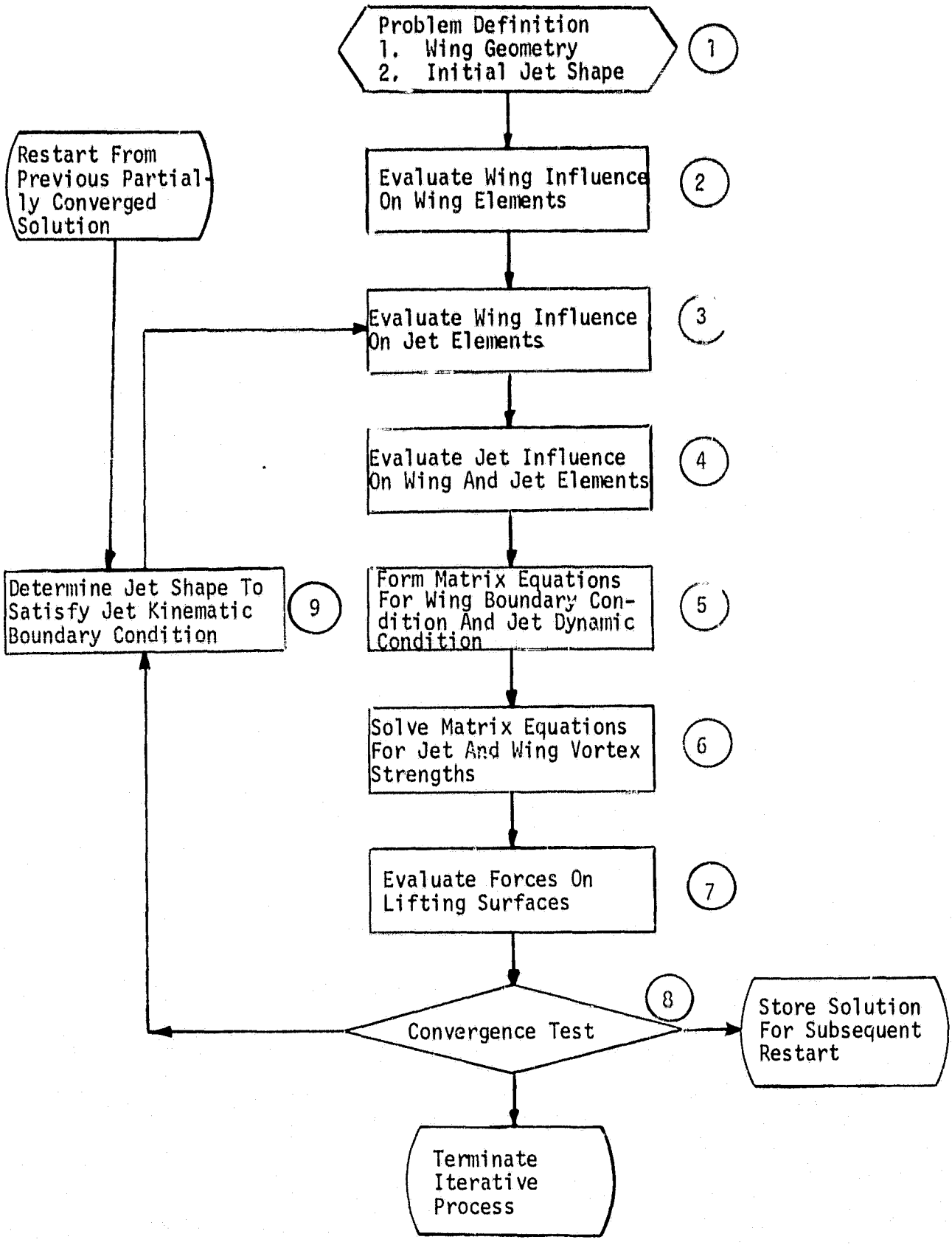

Figure 4. Nonplanar Lifting Systems Jet Flap Program Iterative Solution Scheme

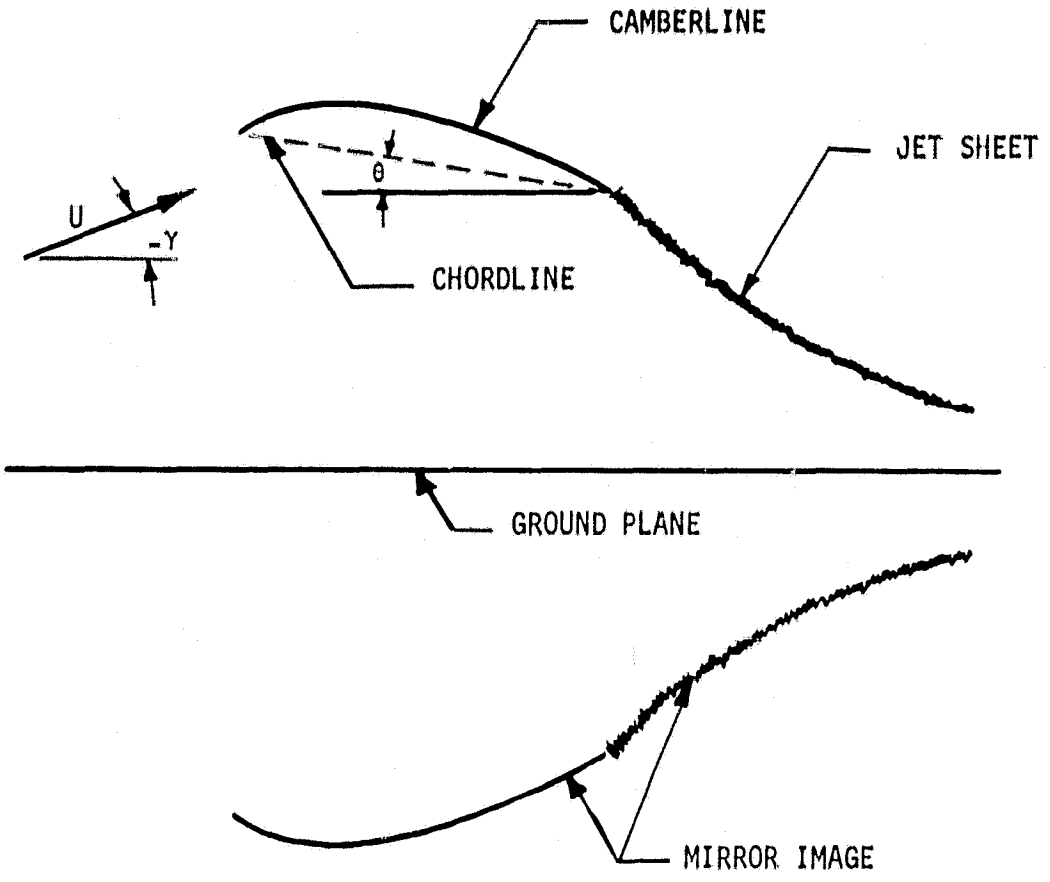

θ = ATTITUDE ANGLE γ = FLIGHT PATH ANGLE

$\alpha = \theta - \gamma$

Figure 5. Illustration in Two-Dimensions of the Mirror Image Technique for Ground Effect Analysis and Parameters Required to Define the Flight Path

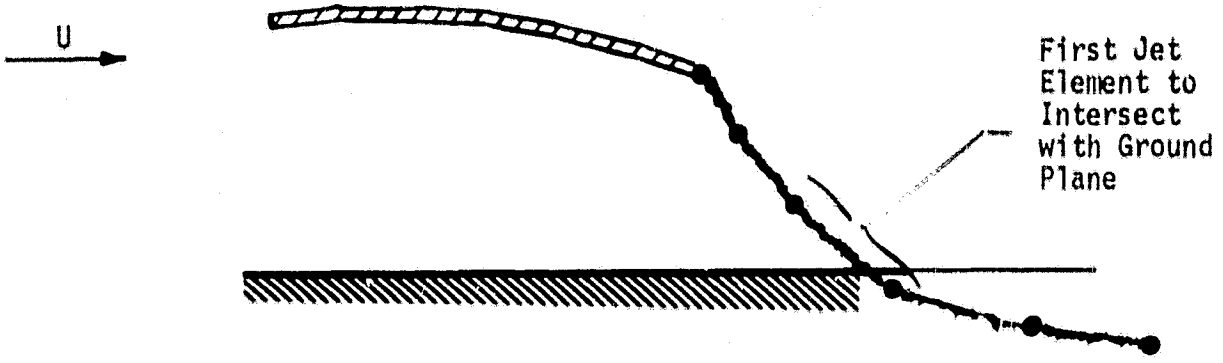

(a) Before Jet Truncation

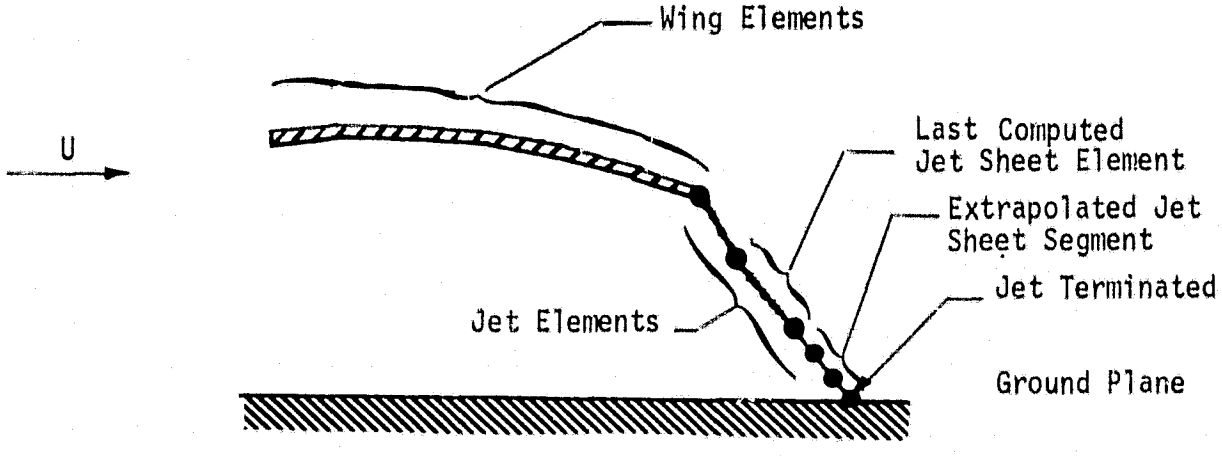

(b) After Truncation

Figure 5. Schematic of Jet Inpingment Model

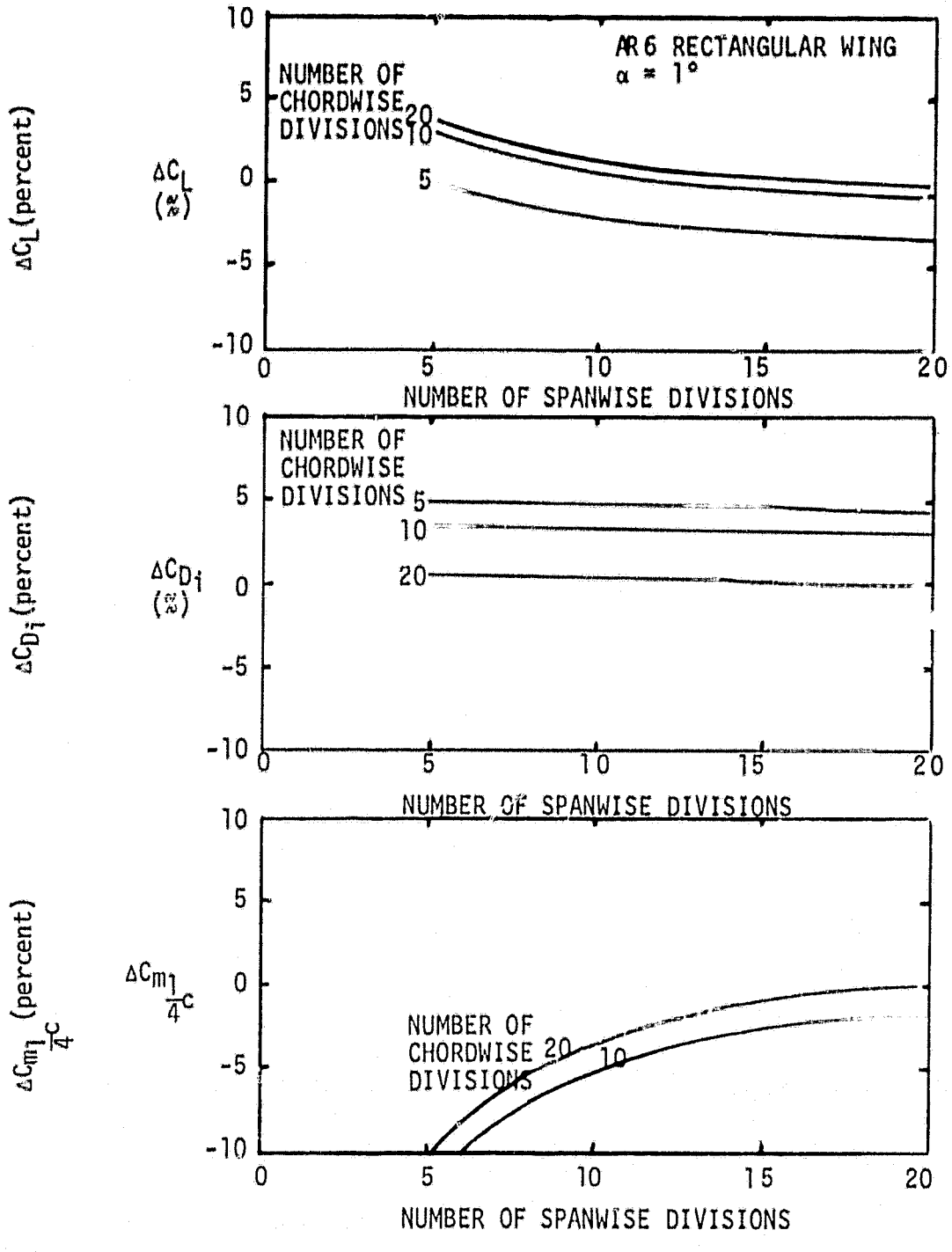

Figure 7. Sensitivity of the Solution to the Number of Spanwise and Chordwise Divisions (Base Case: 20 chordwise x 20 spanwise divisions)

CHORDWISE DIVISIONS:
7 WING
6 JET

FULL SPAN, UNIFORM JET
$\delta_J = 30°$ $C_J = 1.0$
OUT OF GROUND EFFECT

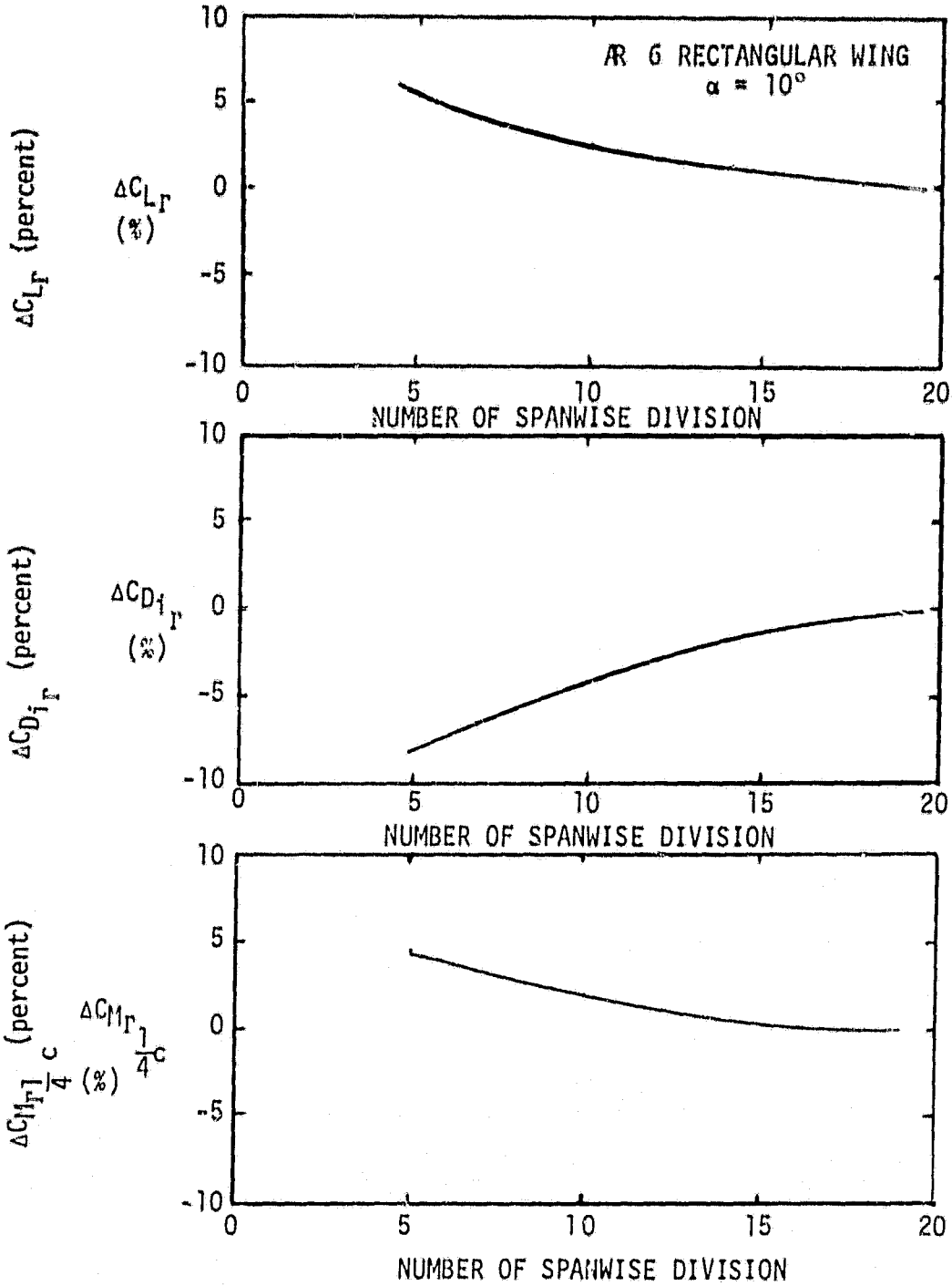

Figure 8. Sensitivity of the NPLS Jet Flap Solution to the Number of Spanwise Divisions (Base Case: 20 Spanwise Divisons).

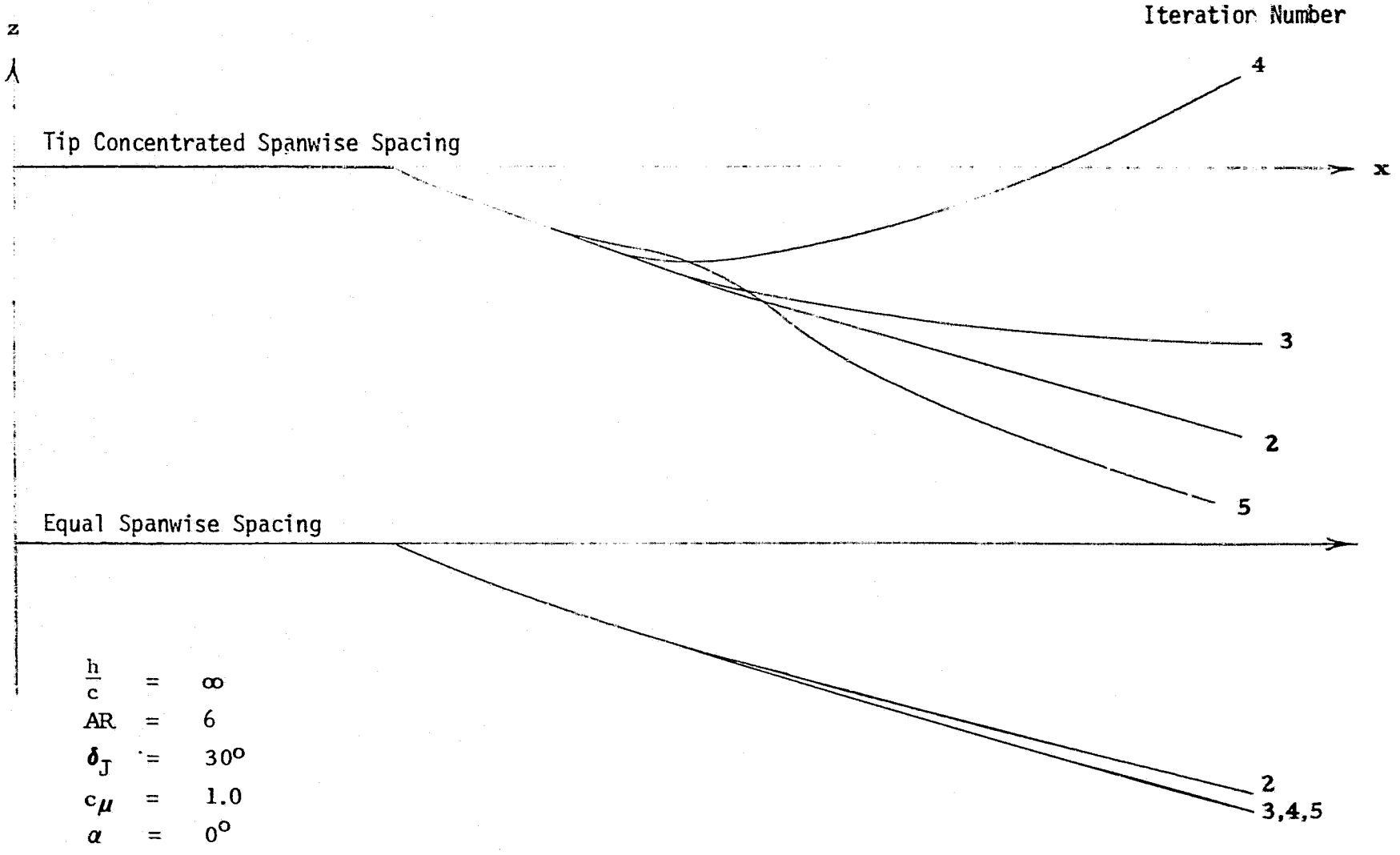

Figure 9. Jet Shapes Near the Tip for a Rectangular Jet-Flapped Wing.

AR 6 Rect. Wing with Full Span Jet
10 Spanwise Rows
$7_{wing} + 6_{jet}$ Chordwise Elements

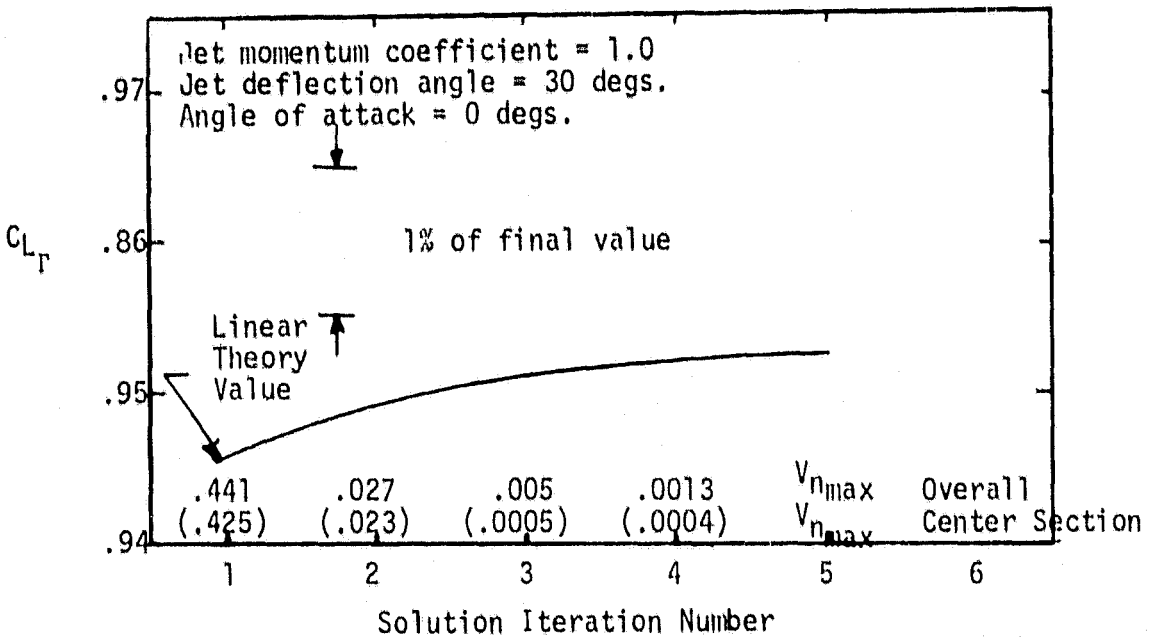

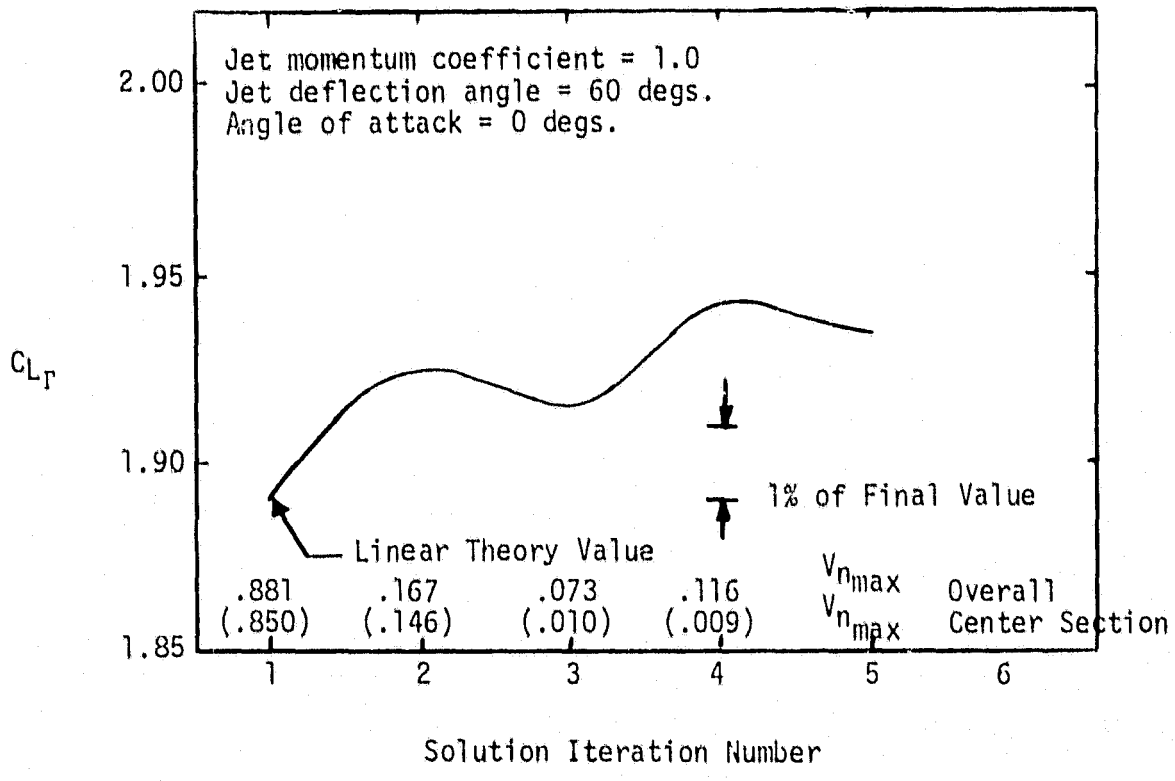

Figure 10. Convergence Characteristics of NPLS Wing Jet Solution

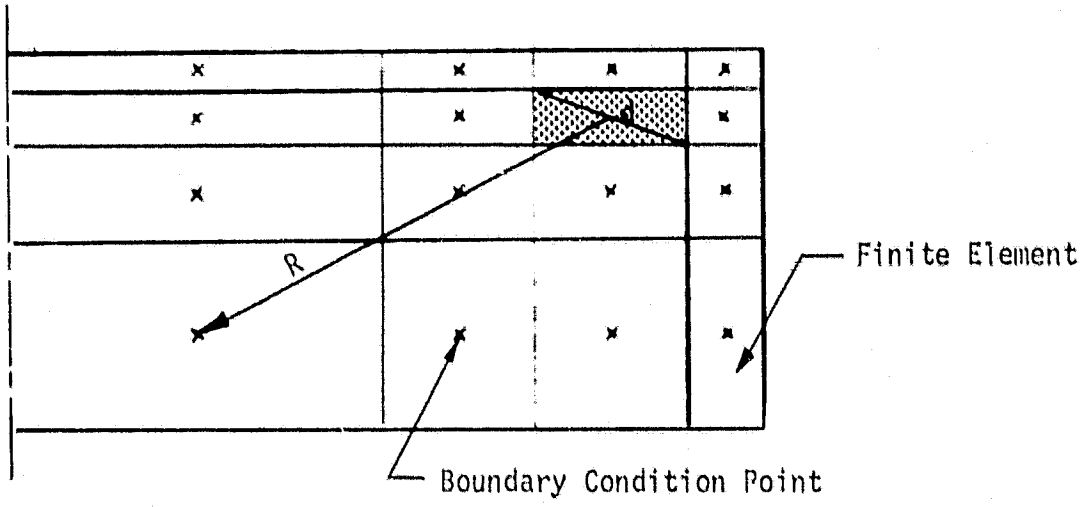

(a) Illustration of Planform and Finite Element Divisions used to Study EVD Functions.

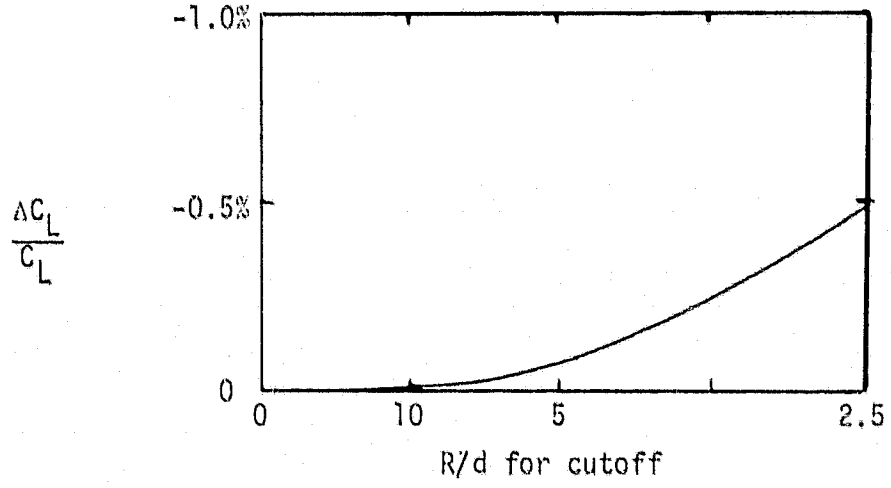

(b) Change in Lift as a Function of Cutoff Distance

Figure 11. Criterion for Selection of Farfield Cutoff Distance.

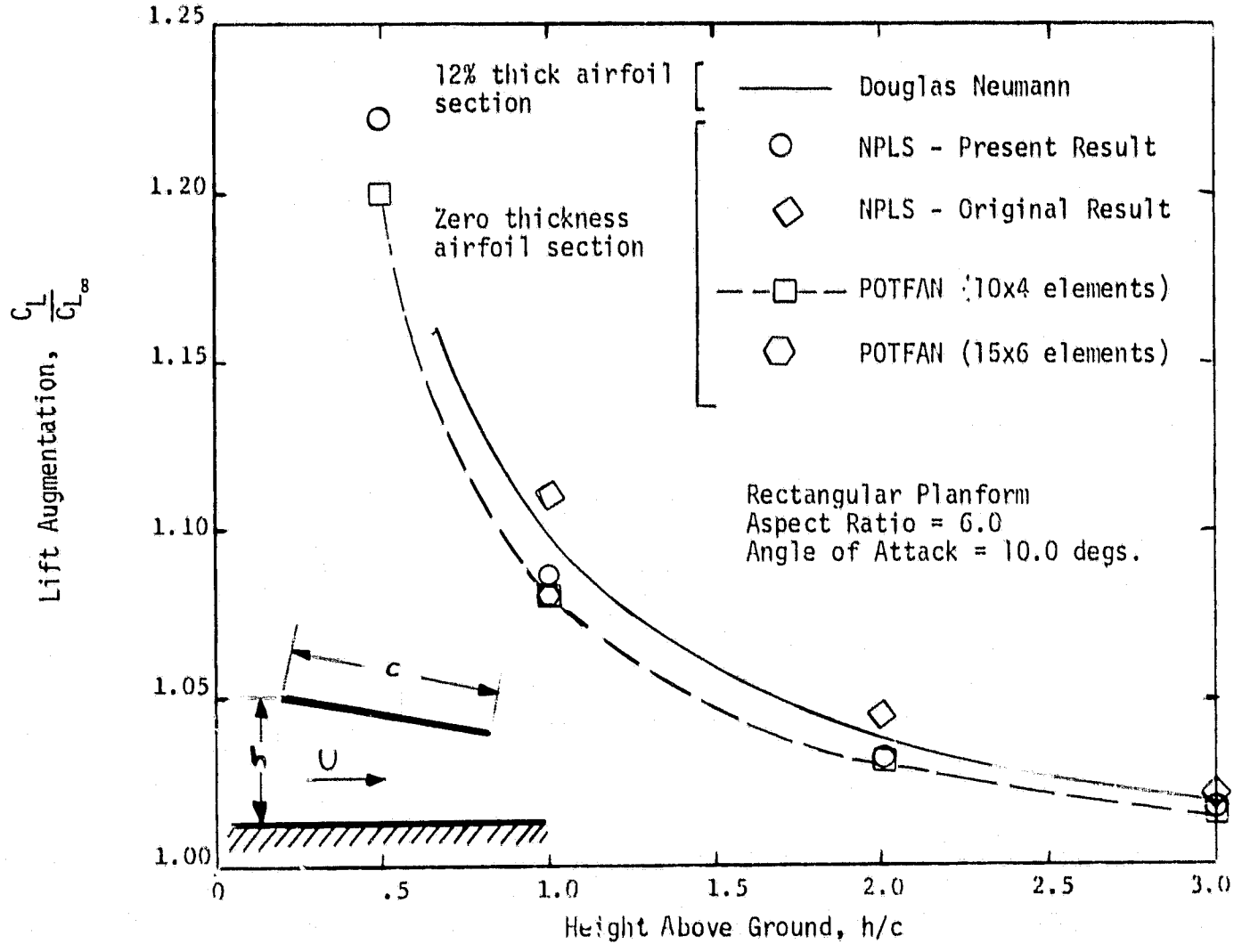

Figure 12. Predicted Lift Variation with Ground Proximity of Rectangular Aspect Ratio 6.0 Wing.

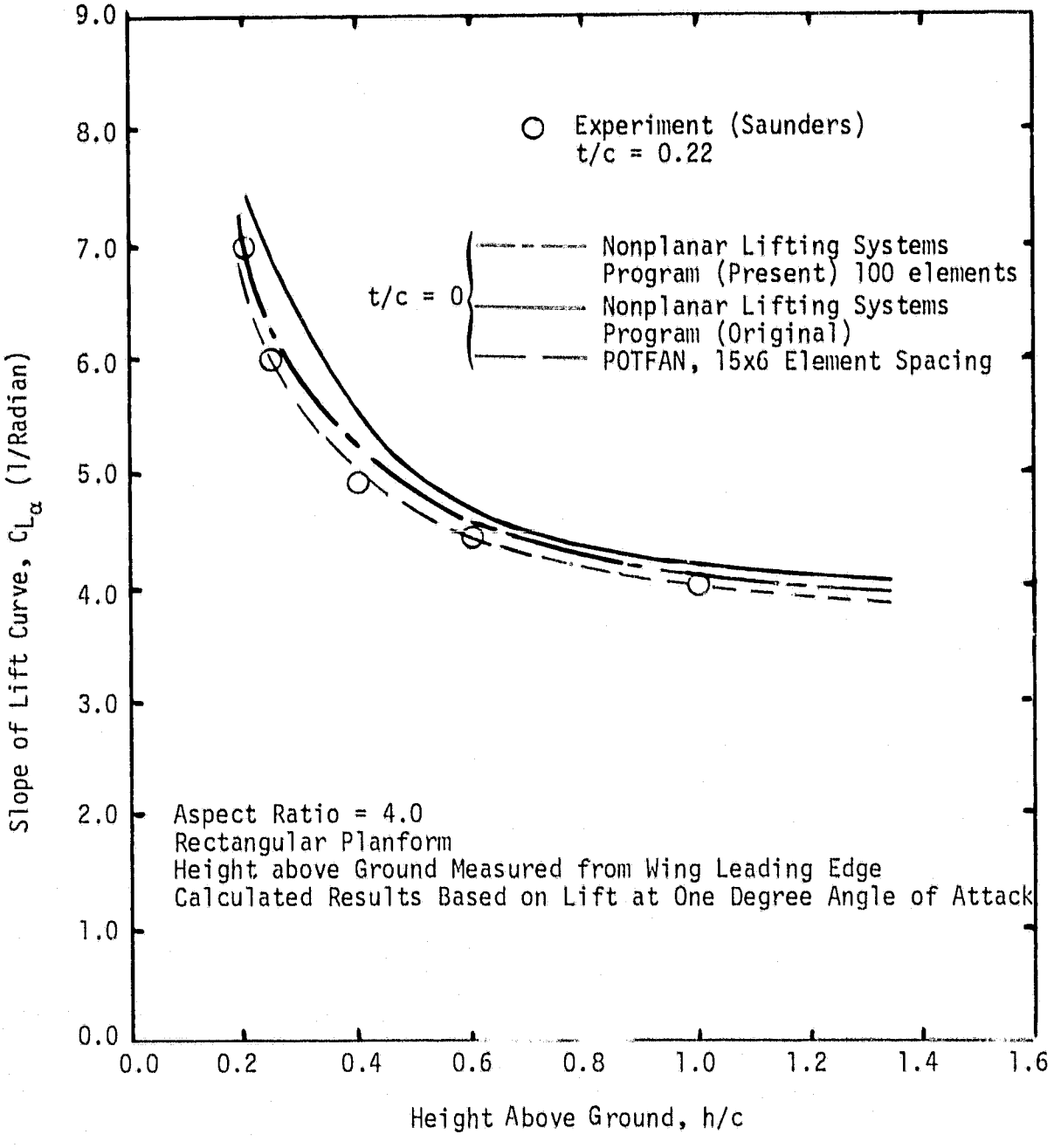

Figure 13. Experimental and Calculated Lift Slope Variation with Ground Height for Rectangular Planform Wing.

RECTANGULAR WING
ZERO FLAP DEFLECTION
ASPECT RATIO = 7.0
ANGLE OF ATTACK = 10.0 DEGS.
HEIGHT ABOVE GROUND MEASURED FROM WING LEADING EDGE

——— NPLS 42 Elements, Steady C_{L_∞} = 0.7907
– – – – NPLS 42 Elements, Quasi-Steady Descent, C_{L_∞} = 0.7868
—— —— NPLS 42 Elements, Quasi-Steady Ascent, C_{L_∞} = 0.7979

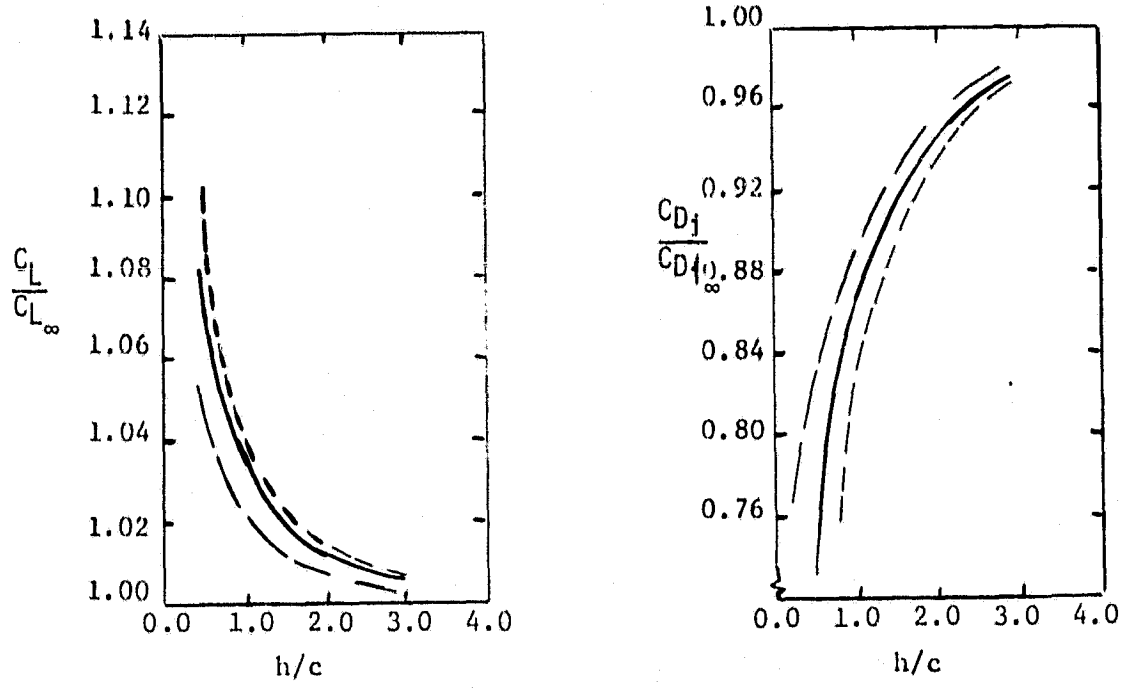

Figure 14. Lift and Induced Drag of a Rectangular Wing in Ground Effect Predicted by NPLS for Steady and Quasi-Steady Flight.

Rectangular Wing
Full Span Flap
Flap Deflection = 60 Degs.
Flap Chord = 0.4 Total Chord
Aspect Ratio = 7.0
Angle of Attack = 10.0 Degs.
Height above Ground Measured from Wing Leading Edge
——— NPLS 7x6 Steady $C_{L_\infty} = 3.5836$
– – – – NPLS 7x6 10 Degs. Quasi-Steady Descent $C_{L_\infty} = 3.4509$
—— —— NPLS 7x6 10 Degs. Quasi-Steady Ascent $C_{L_\infty} = 3.7277$

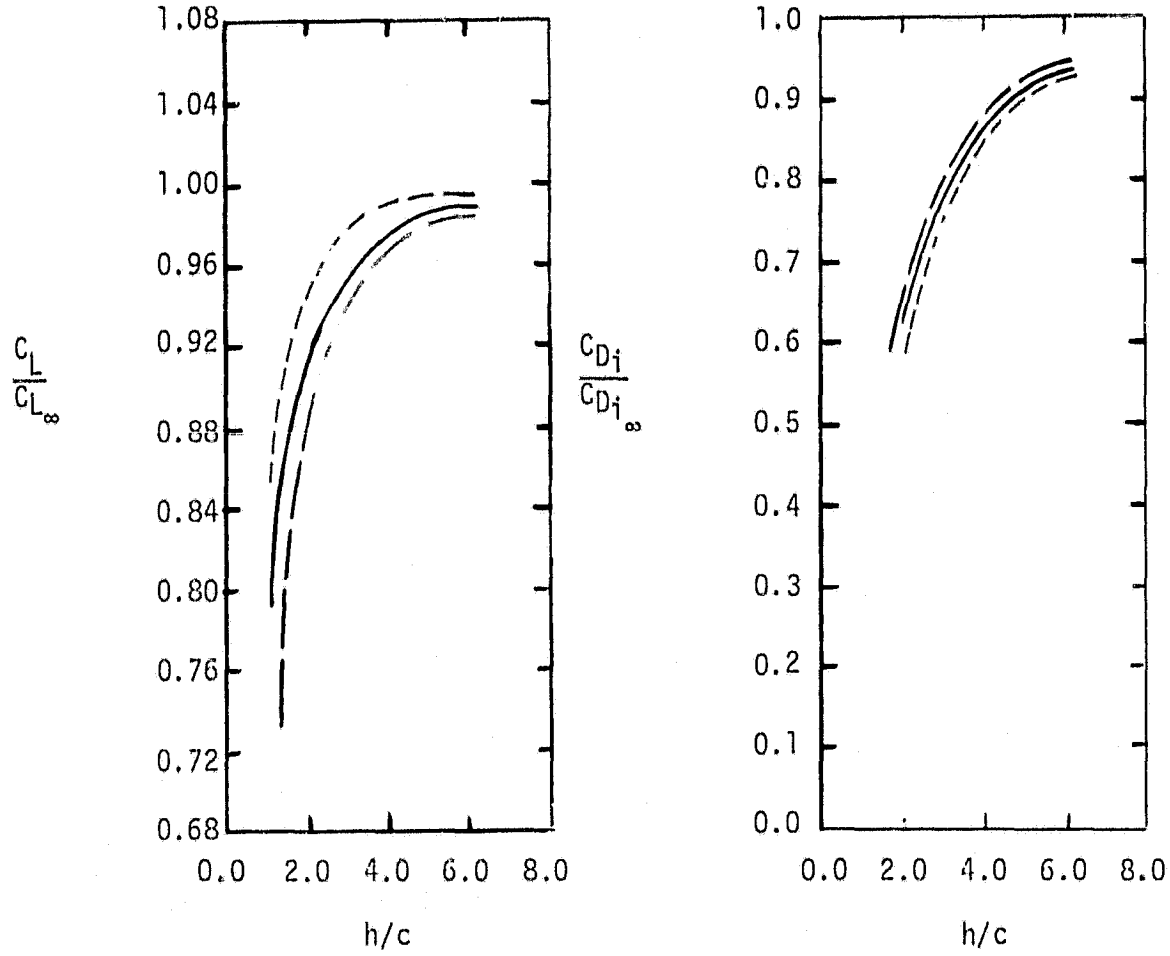

Figure 15. Lift and Induced Drag of a Rectangular Wing with 40-Percent Chord Flap in Ground Effect Predicted by NPLS for Steady and Quasi-Steady Flight.

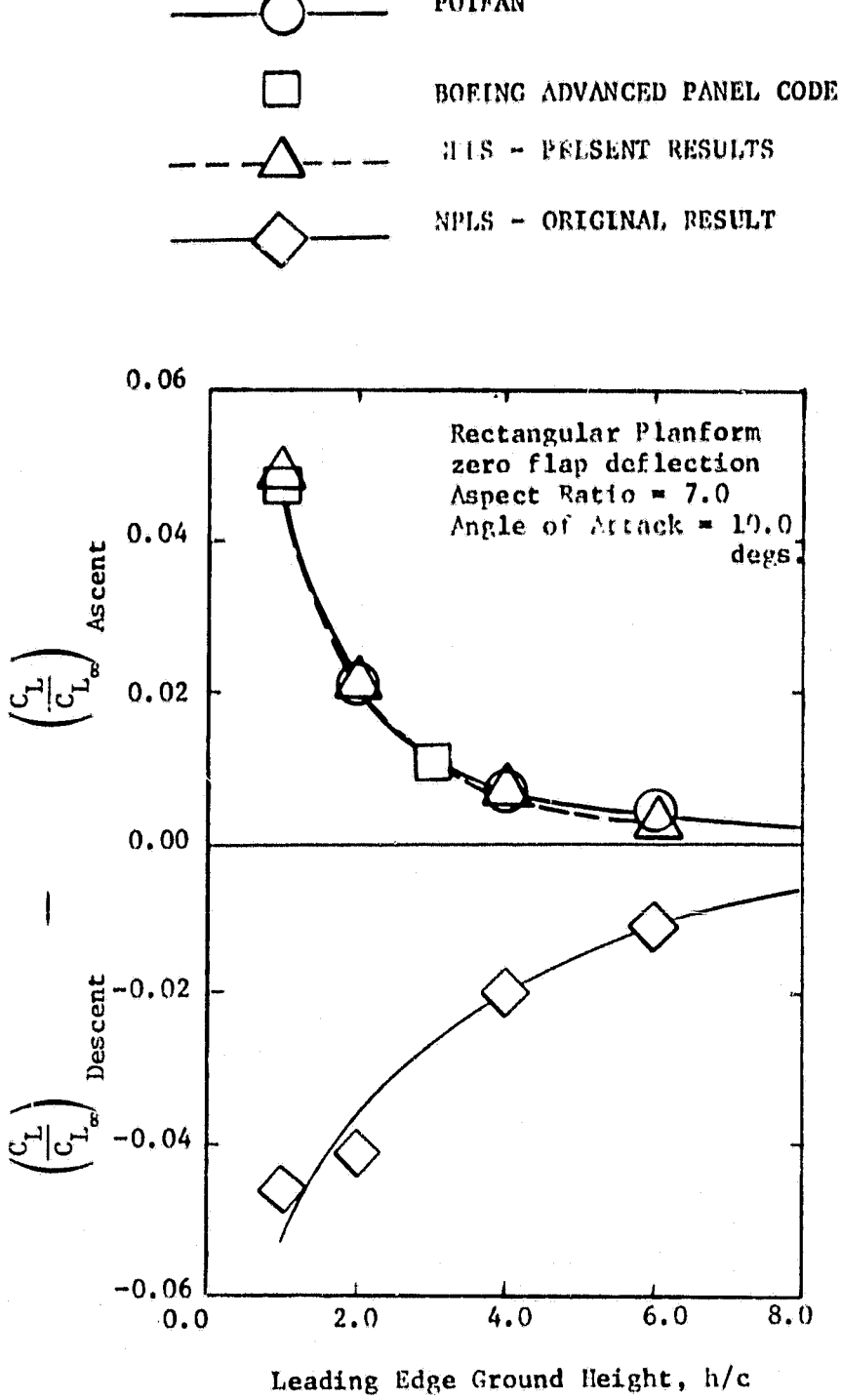

Figure 16. Lift Augmentation Difference Between 10 Degrees Ascent and Descent for Rectangular Aspect Ratio Equal to Seven Wing.

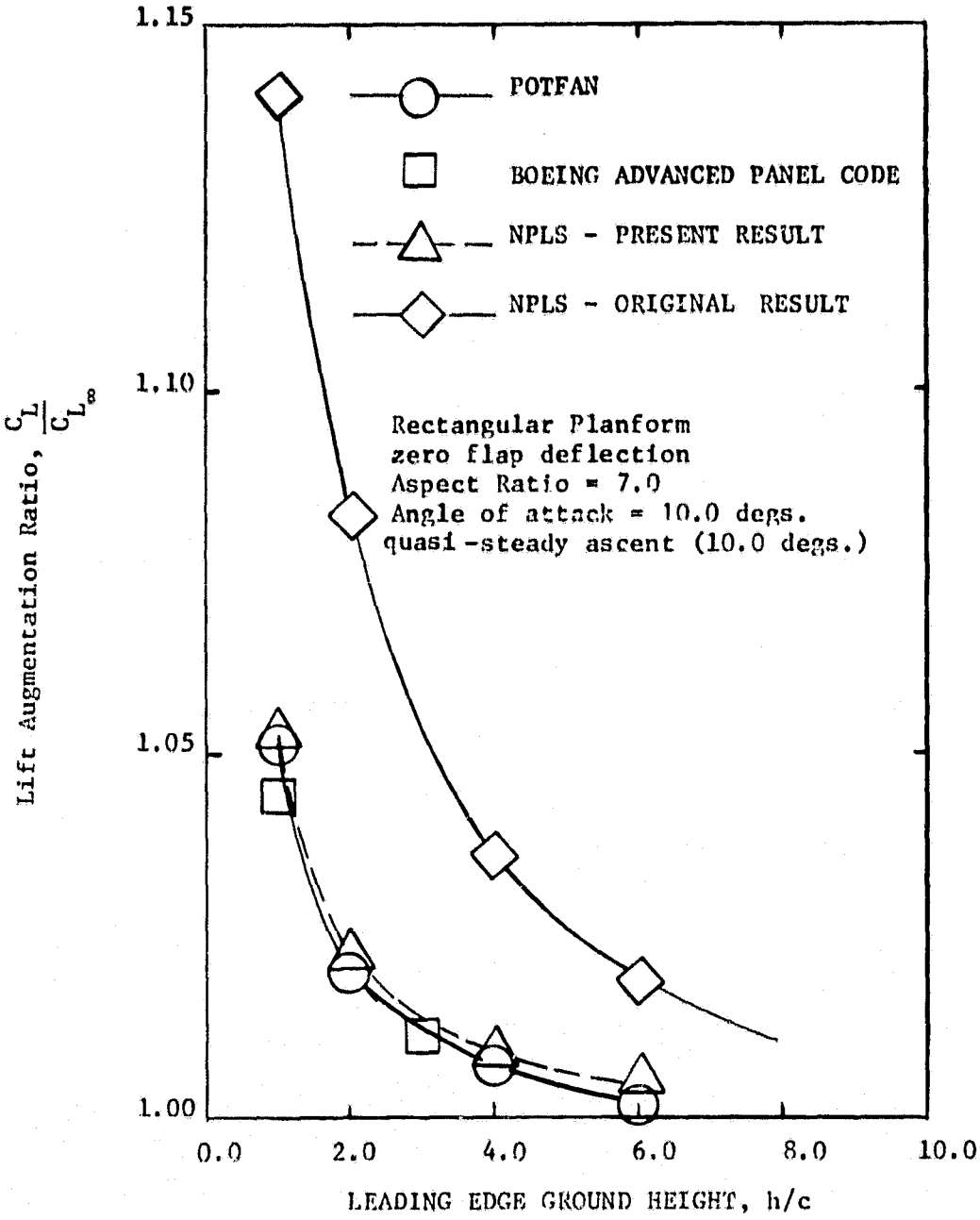

Figure 17. Lift Augmentation for a Rectangular Planform Aspect Ratio Equal to Seven Wing in Ten Degree Quasi-Steady Ascending Flight.

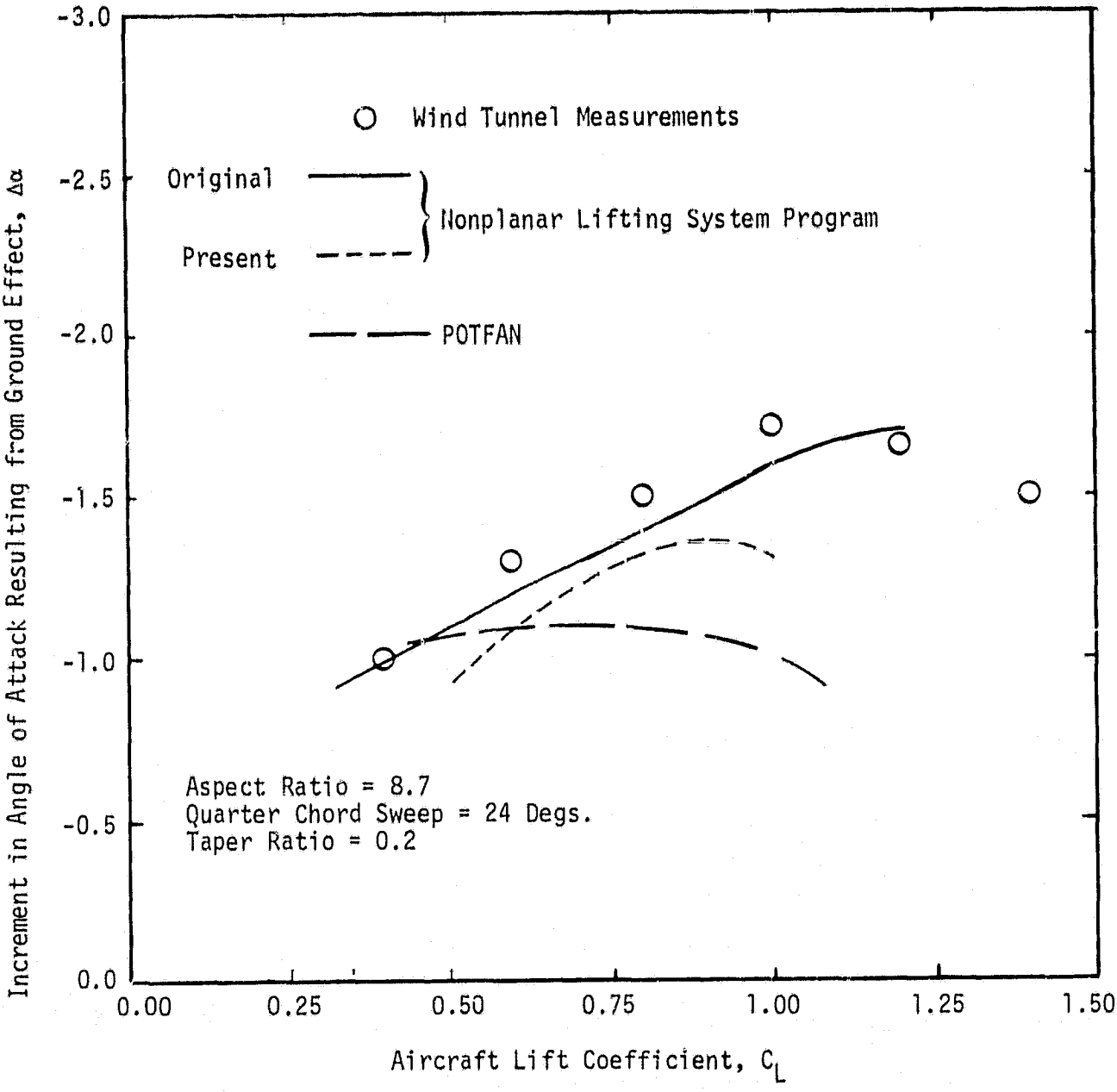

Figure 18 Comparison Between Theory and Wind Tunnel Data for the Ground Effect on Lift on a Subsonic Transport Aircraft with Flaps Deflected Five Degrees.

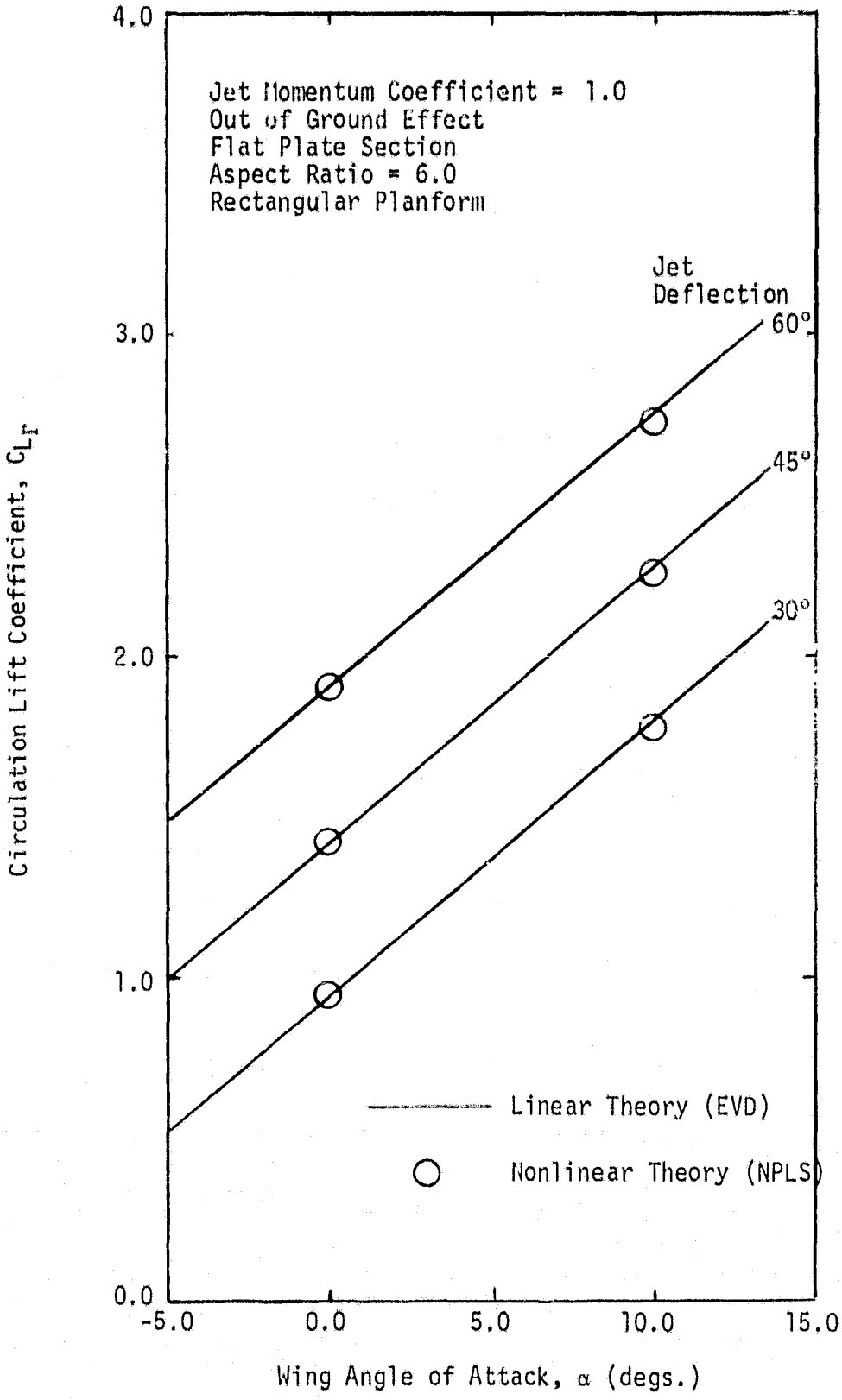

Figure 19. Freeair Lift Predicted for Rectangular Wing with Jet Flap.

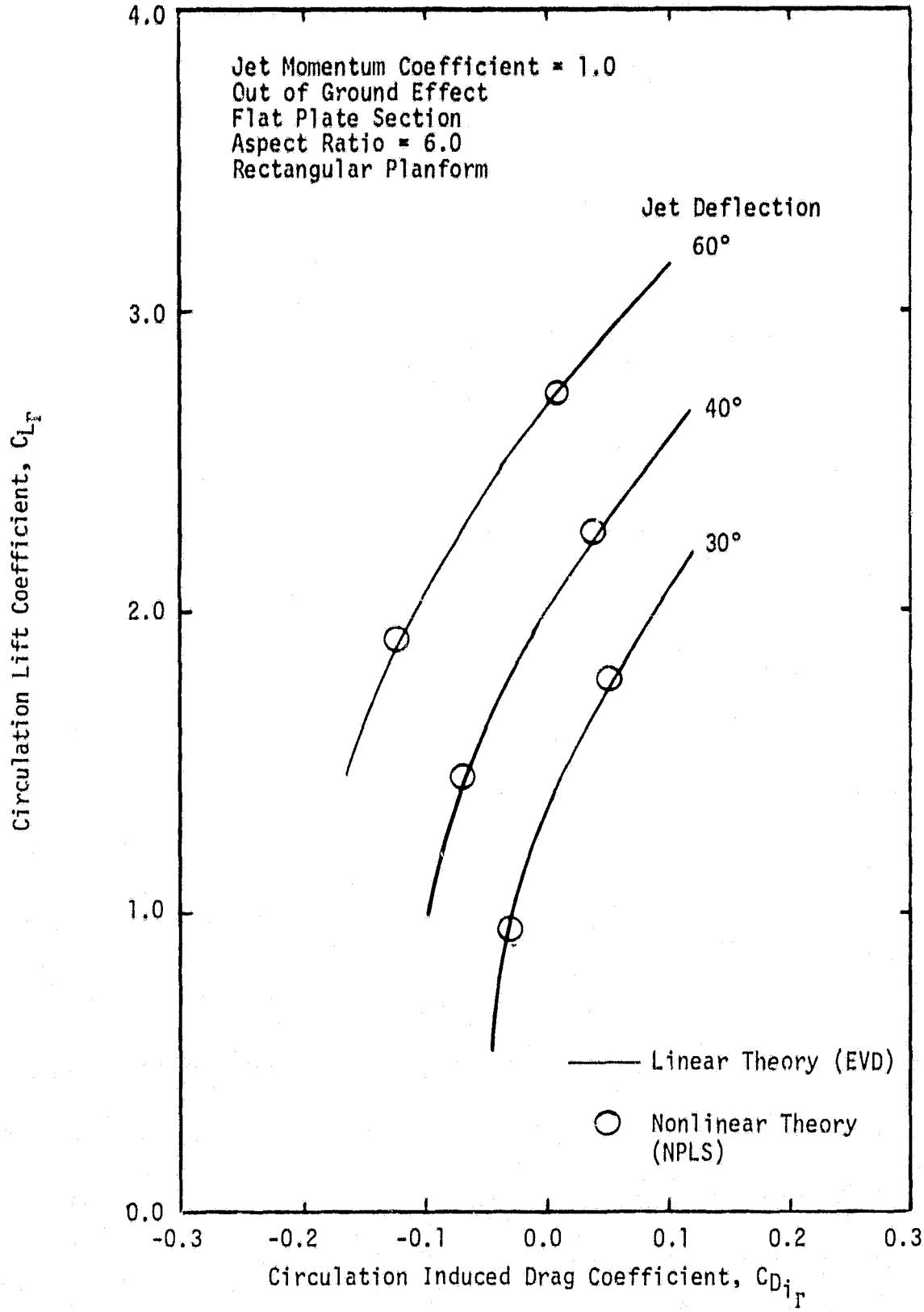

Figure 20. Freeair Drag Polar for Rectangular Wing with Jet Flap.

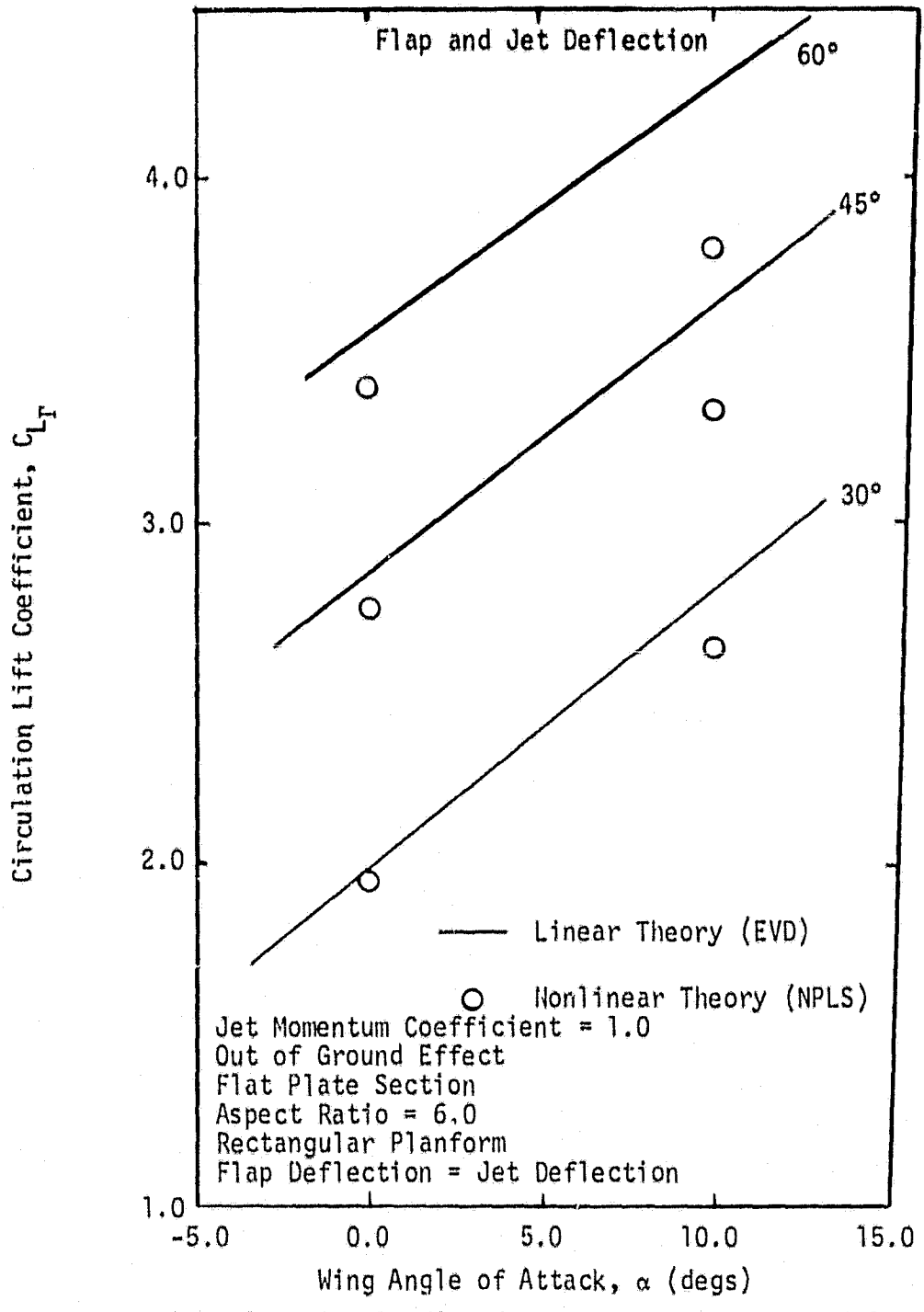

Figure 21. Freeair Lift Predicted for Rectangular Wing with Jet Flap and Forty Percent Chord Mechanical Flap.

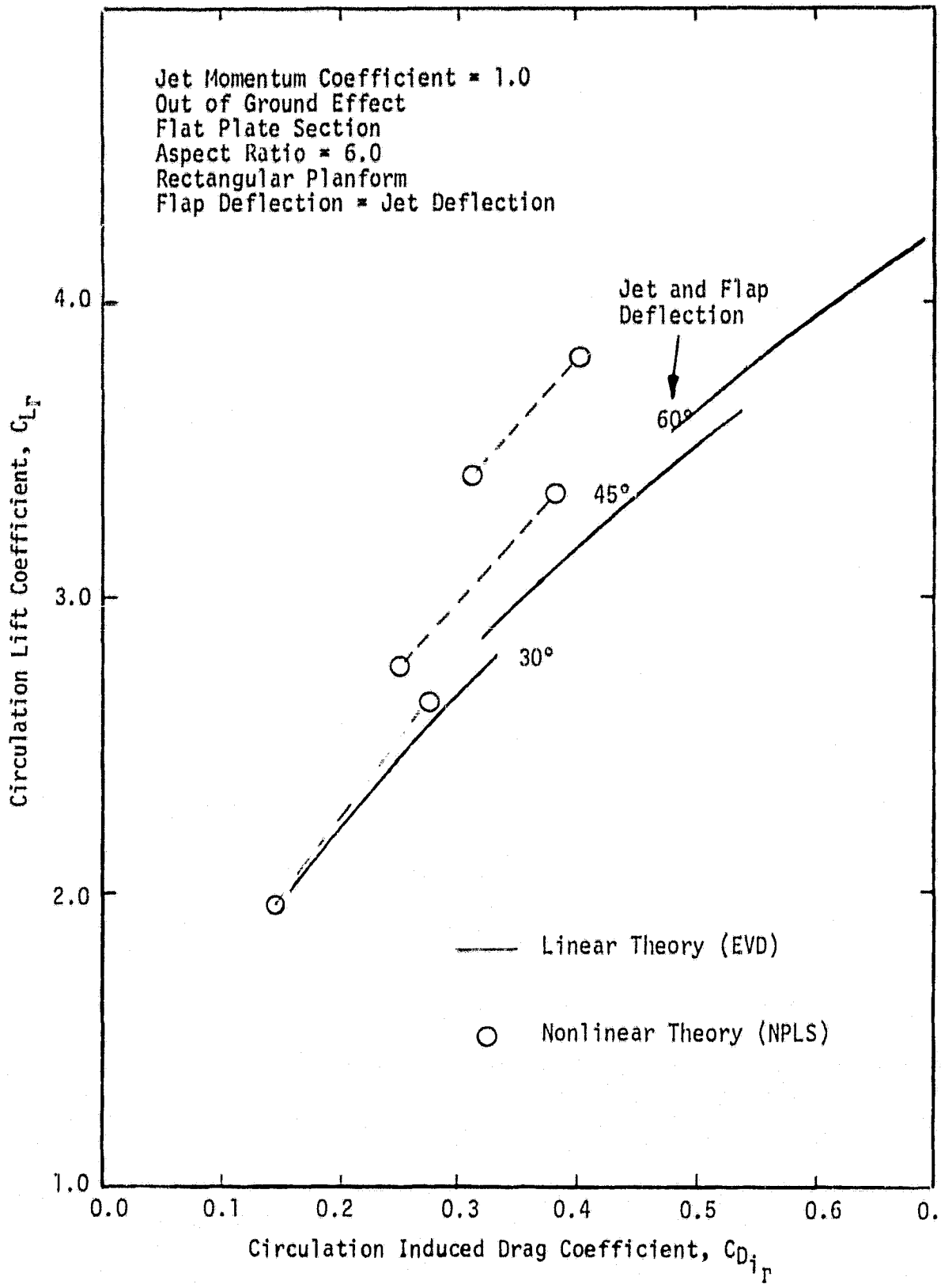

Figure 22. Freeair Drag Polar for Rectangular Wing with Jet Flap and Forty Percent Chord Mechanical Flap.

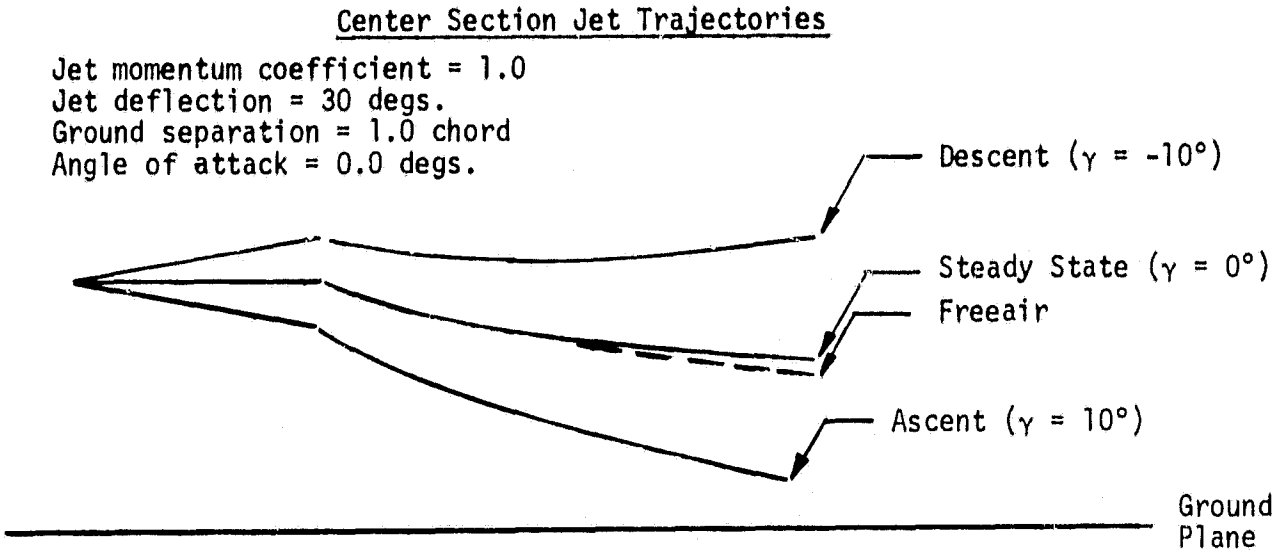

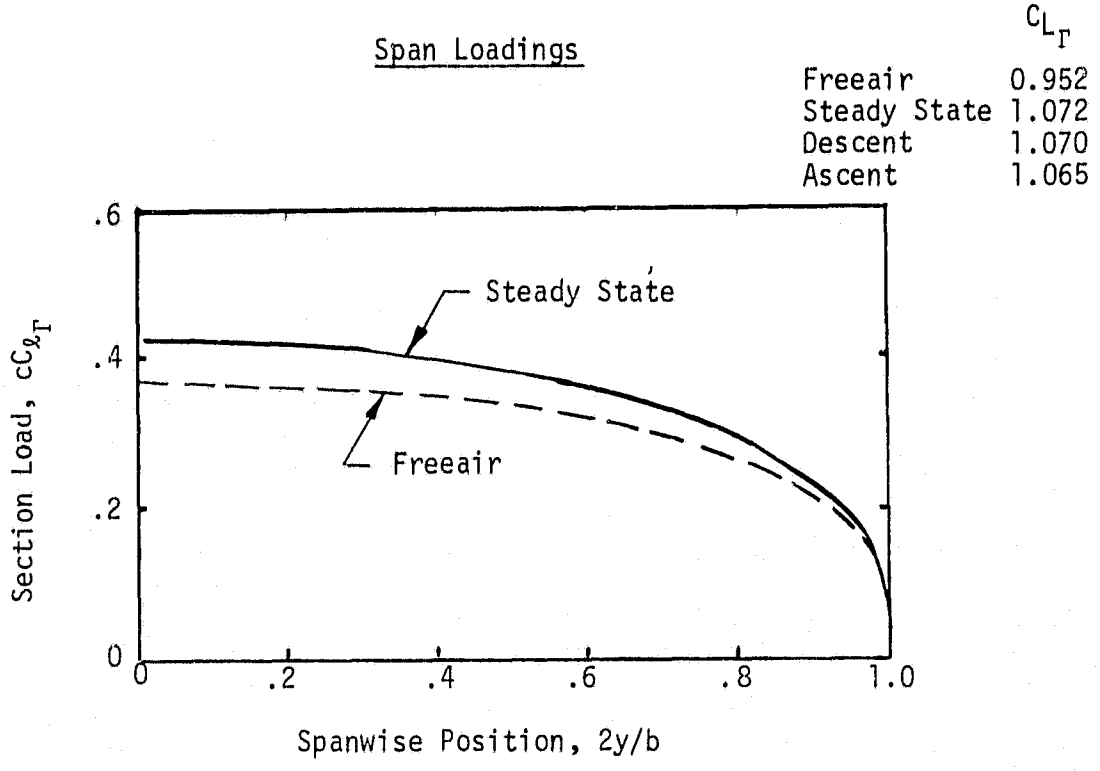

Figure 23. AR 6 Rectangular Wing with Full Span Jet with 30 Degrees Jet Deflection: Effect of Steady & Quasi-Steady Ground Effects.

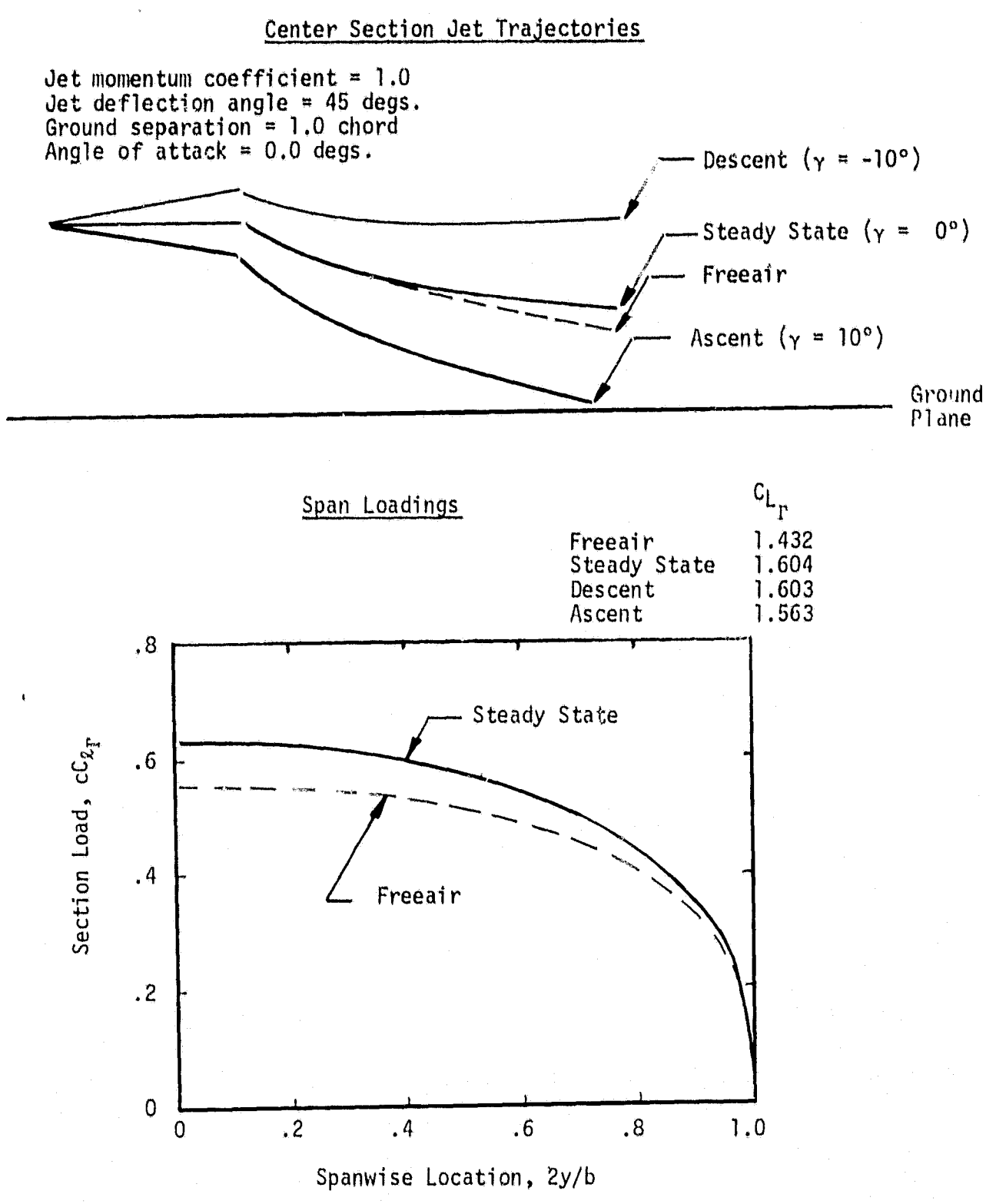

Figure 24. AR 6 Rectangular Wing with Full Span Jet with 45 Degrees Jet Deflection: Effect of Steady & Quasi-Steady Ground Effects.

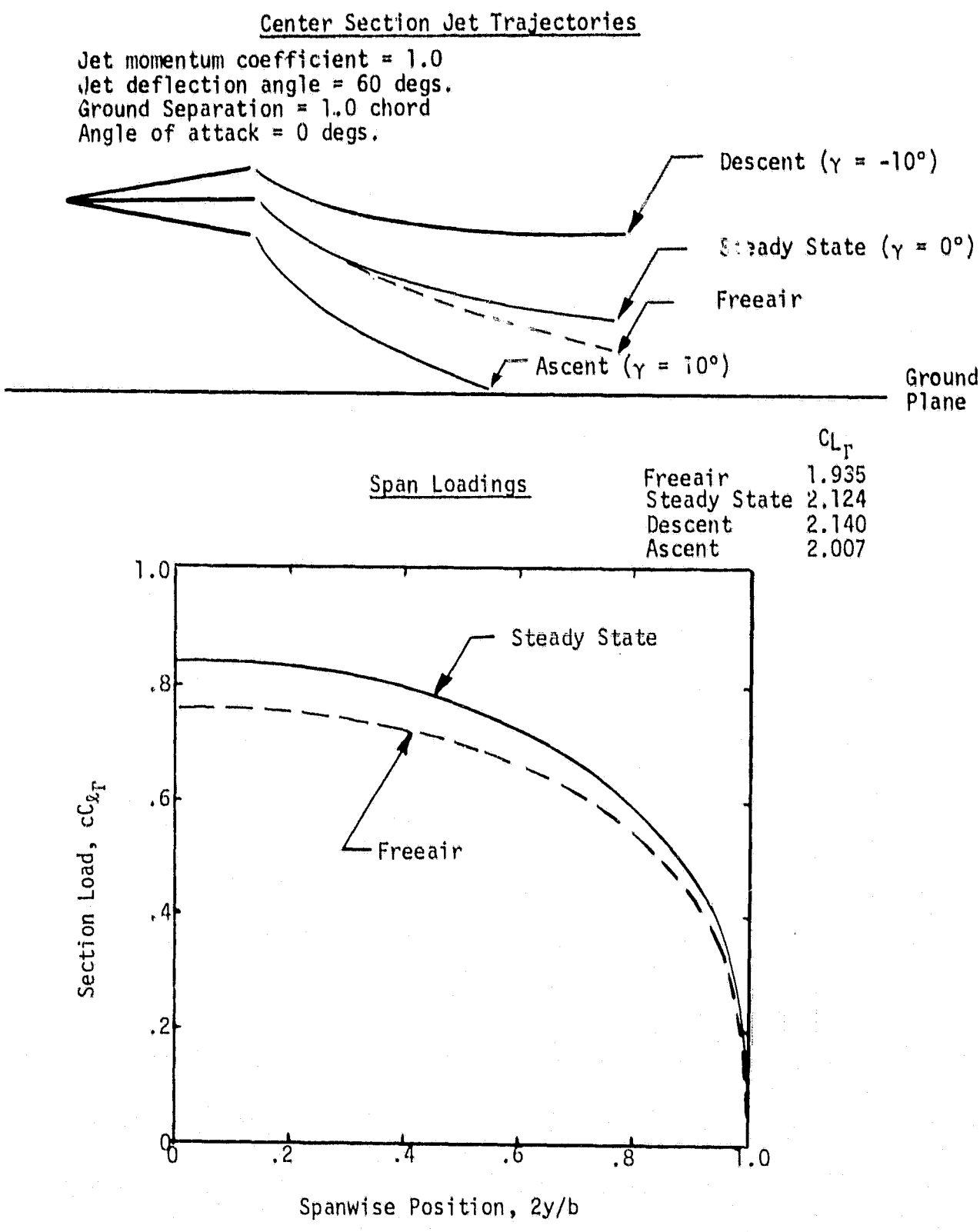

Figure 25. AR 6 Rectangular Wing with Full Span Jet with 60 Degrees Jet Deflection: Effect of Steady & Quasi-Steady Ground Effects.

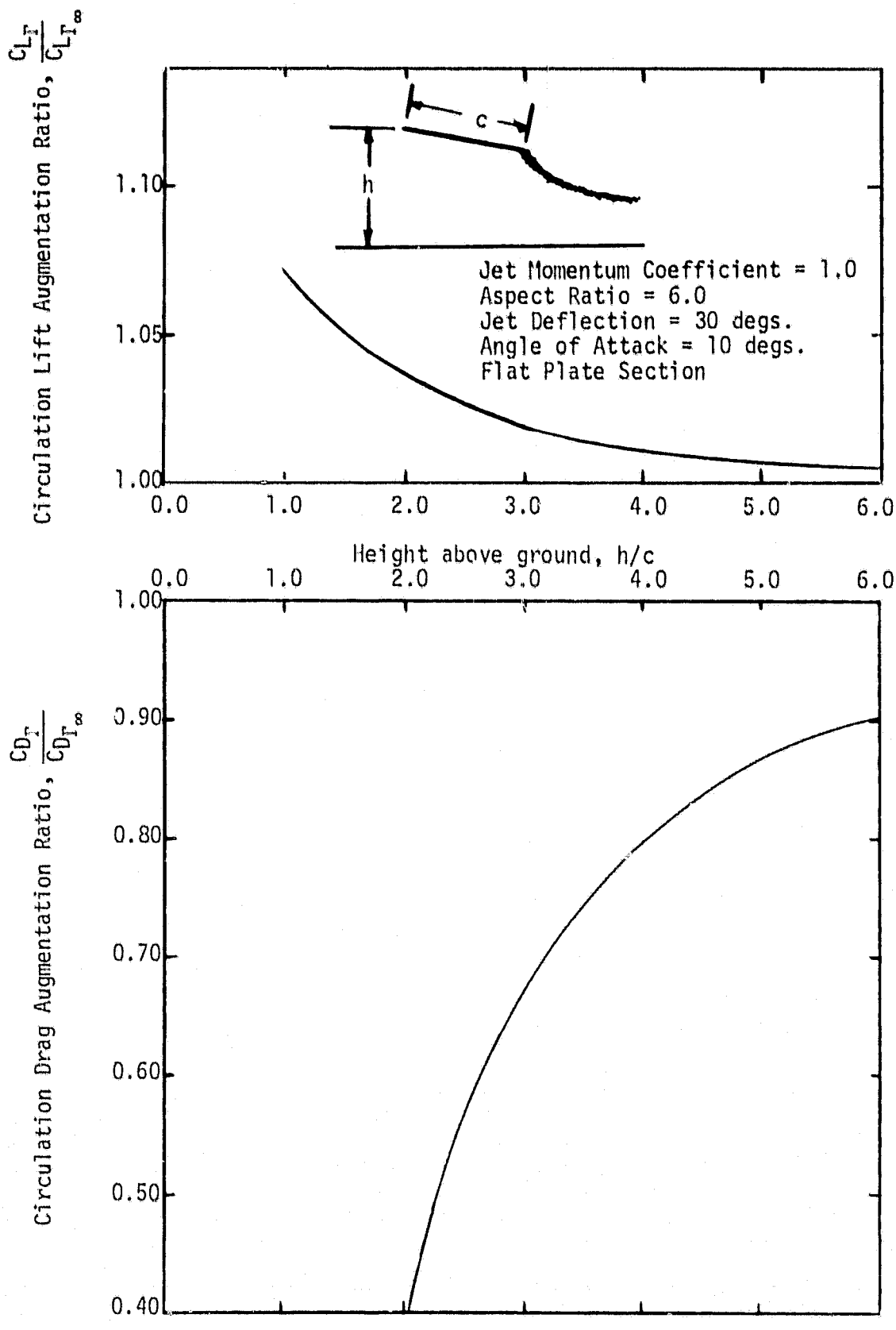

Figure 26. Predicted Lift and Drag Characteristics for Rectangular Wing with Jet Flap in Ground Effect.

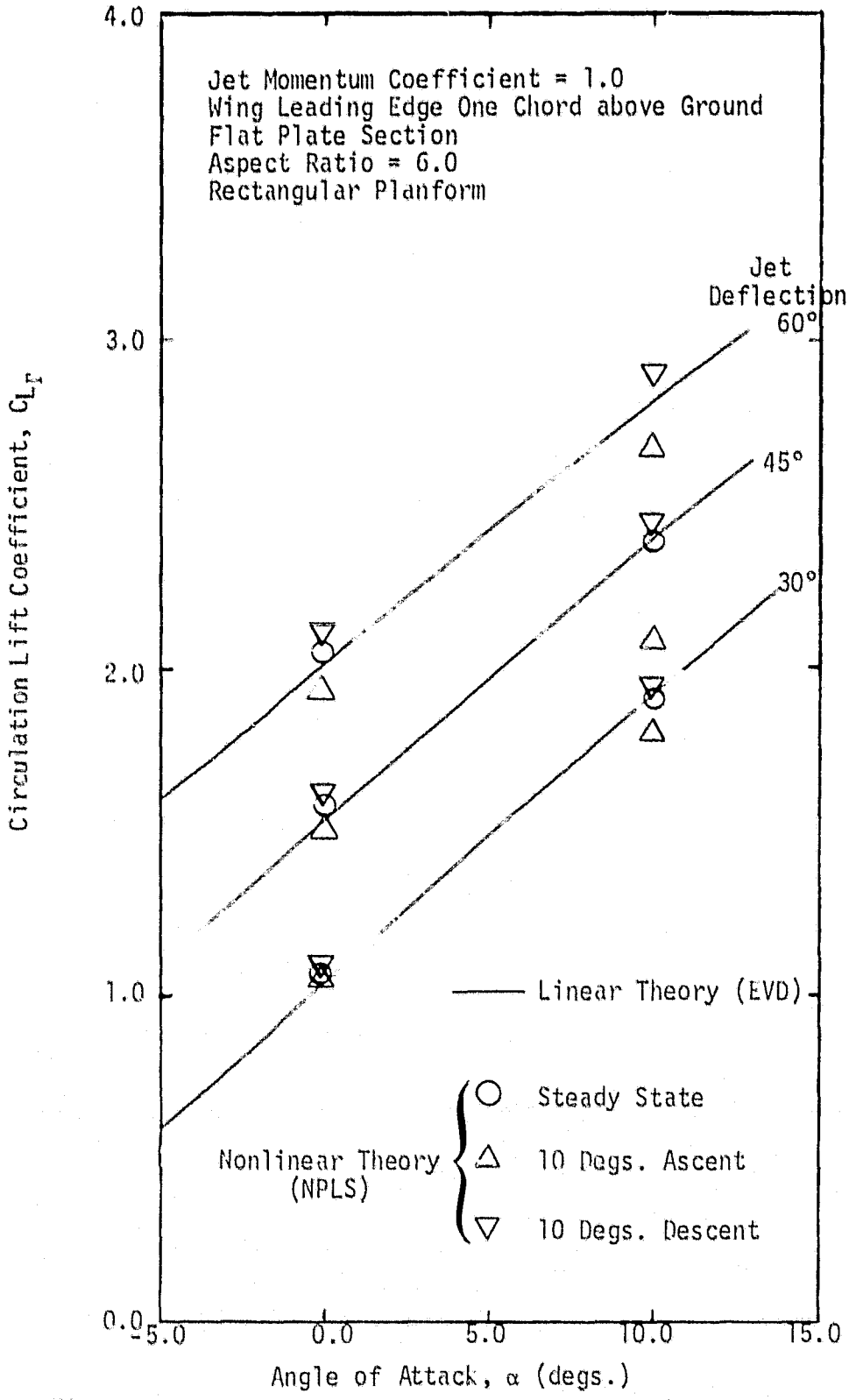

Figure 27. Predicted Lift for Rectangular Wing with Jet Flap in Ground Effect.

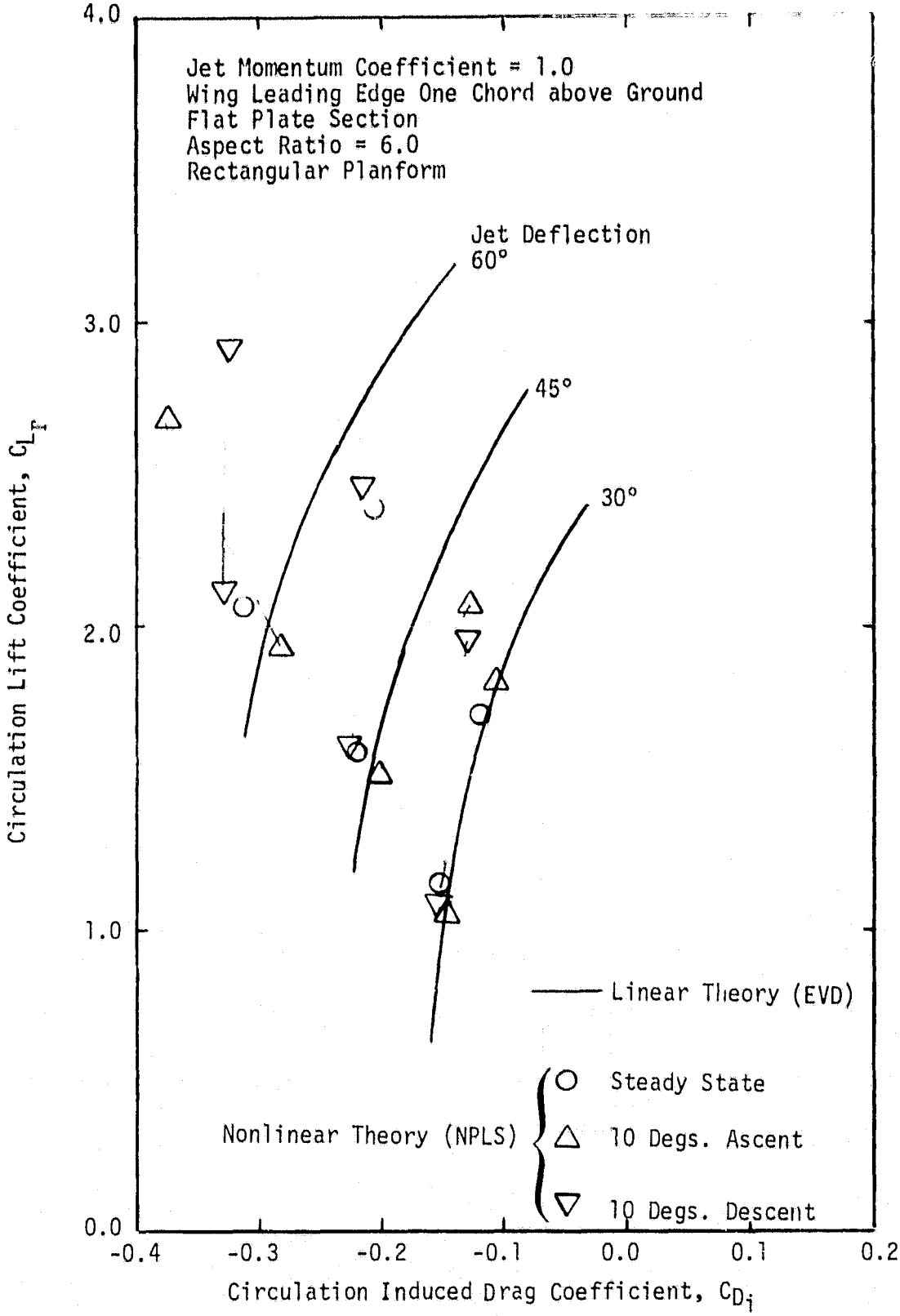

Figure 28. Drag Polar for Rectangular Wing with Jet Flap in Ground Effect.

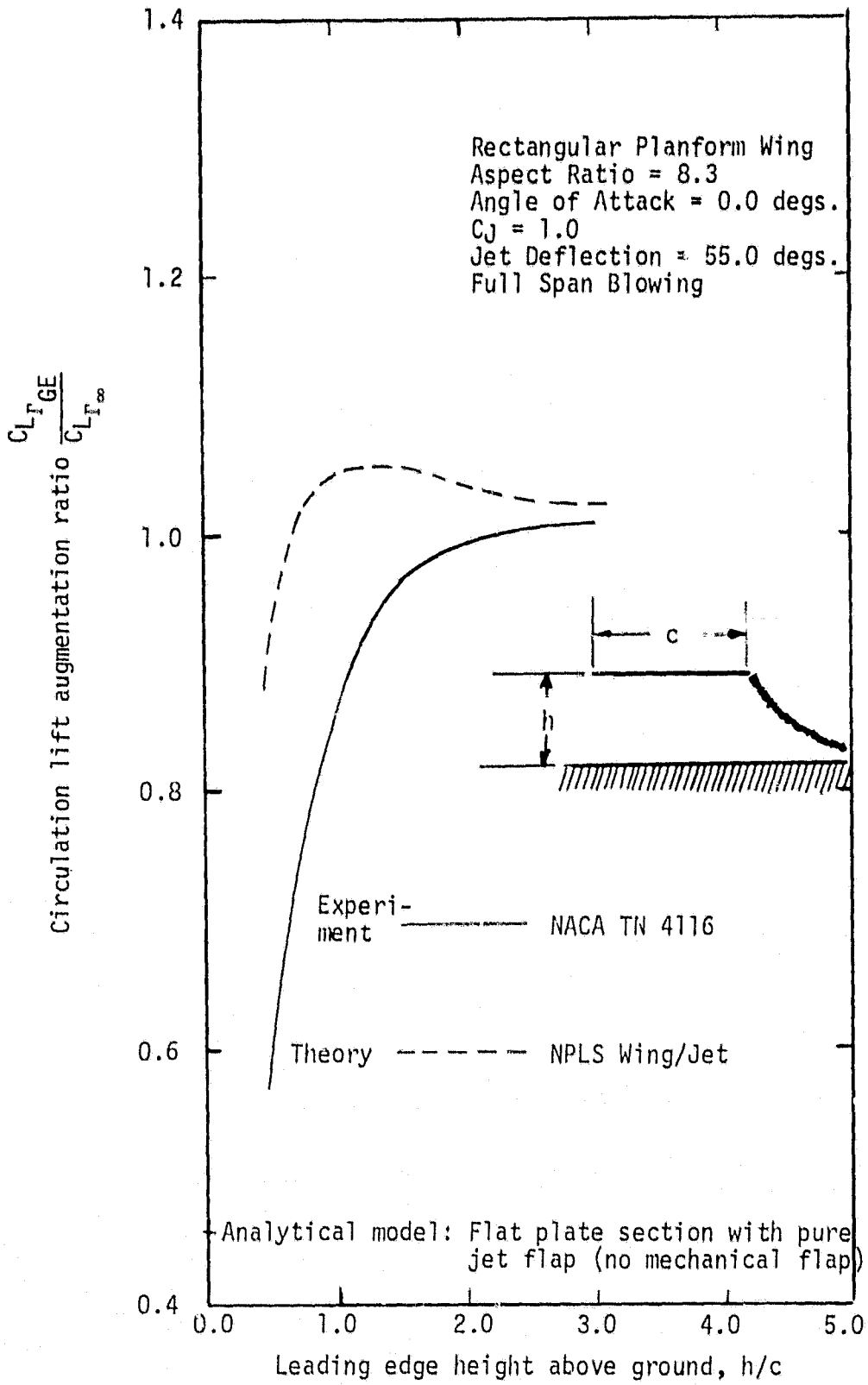

Figure 29. Comparison of Experimental and Analytical Lift Augmentation Ratios for Rectangular Wing in Ground Effect.

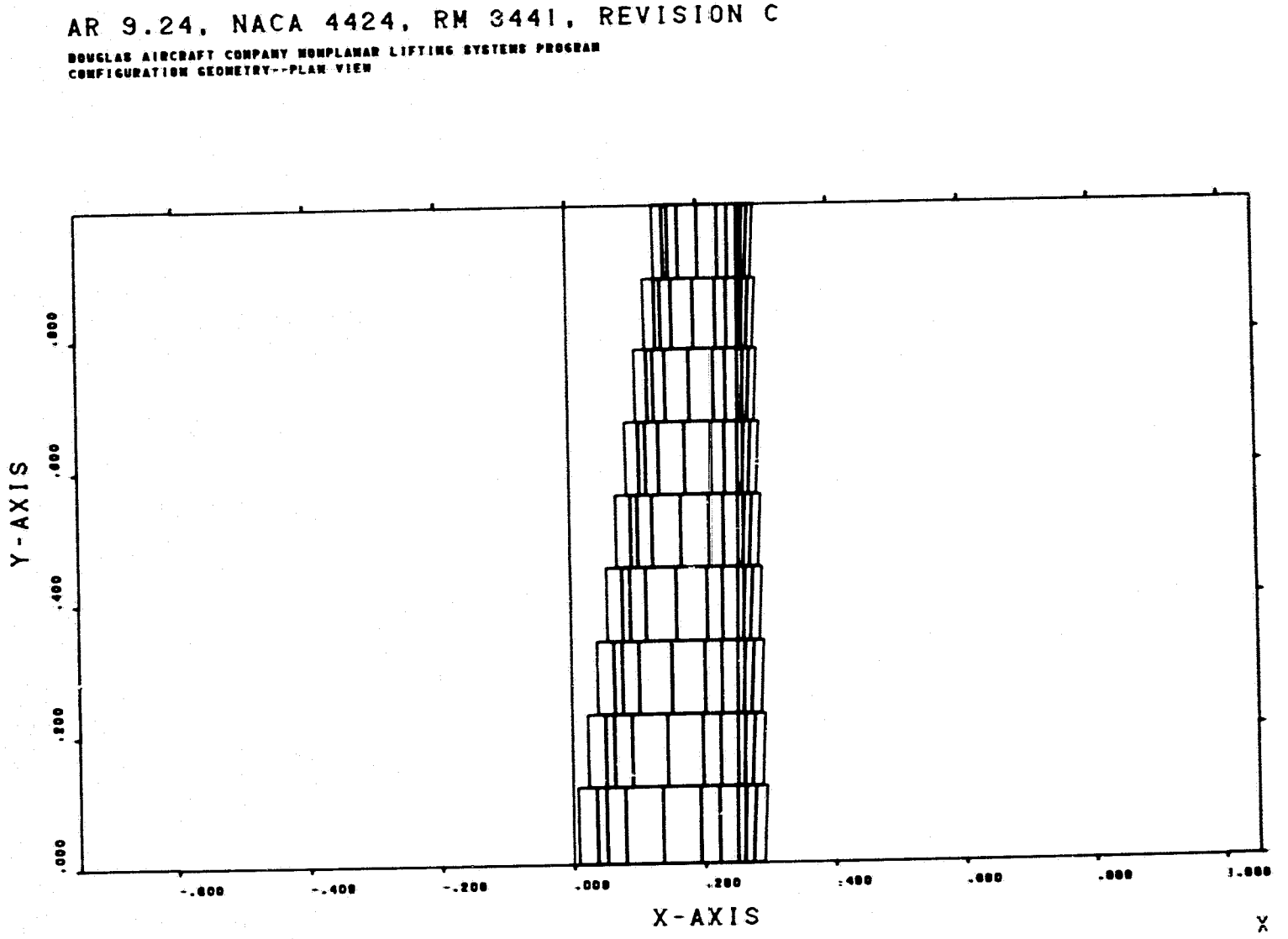

Figure 30. Plan View of NPLS Element Arrangement for Configuration of Reference 24.

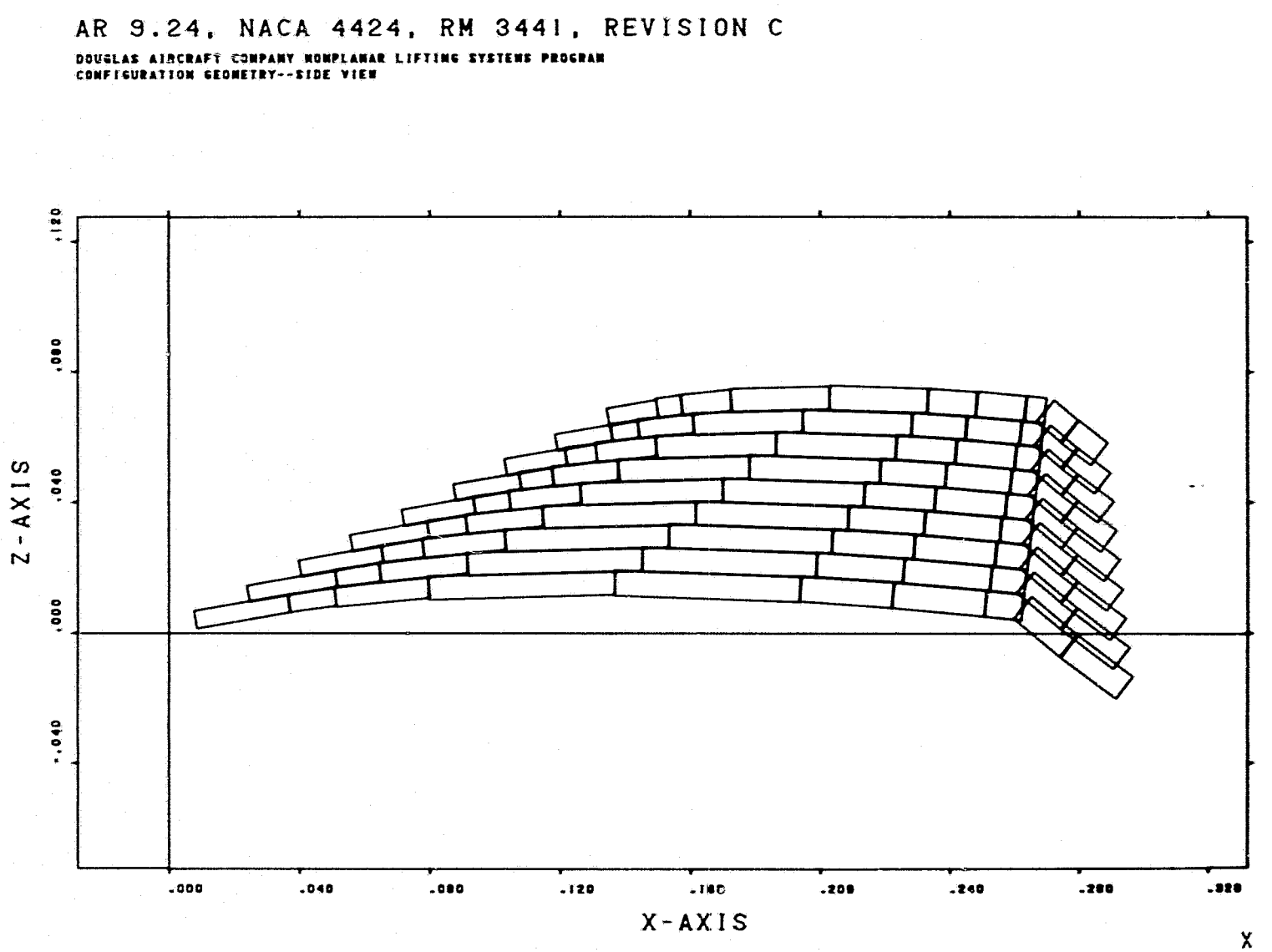

Figure 31. Side View of NPLS Element Arrangement for Configuration of Reference 24.

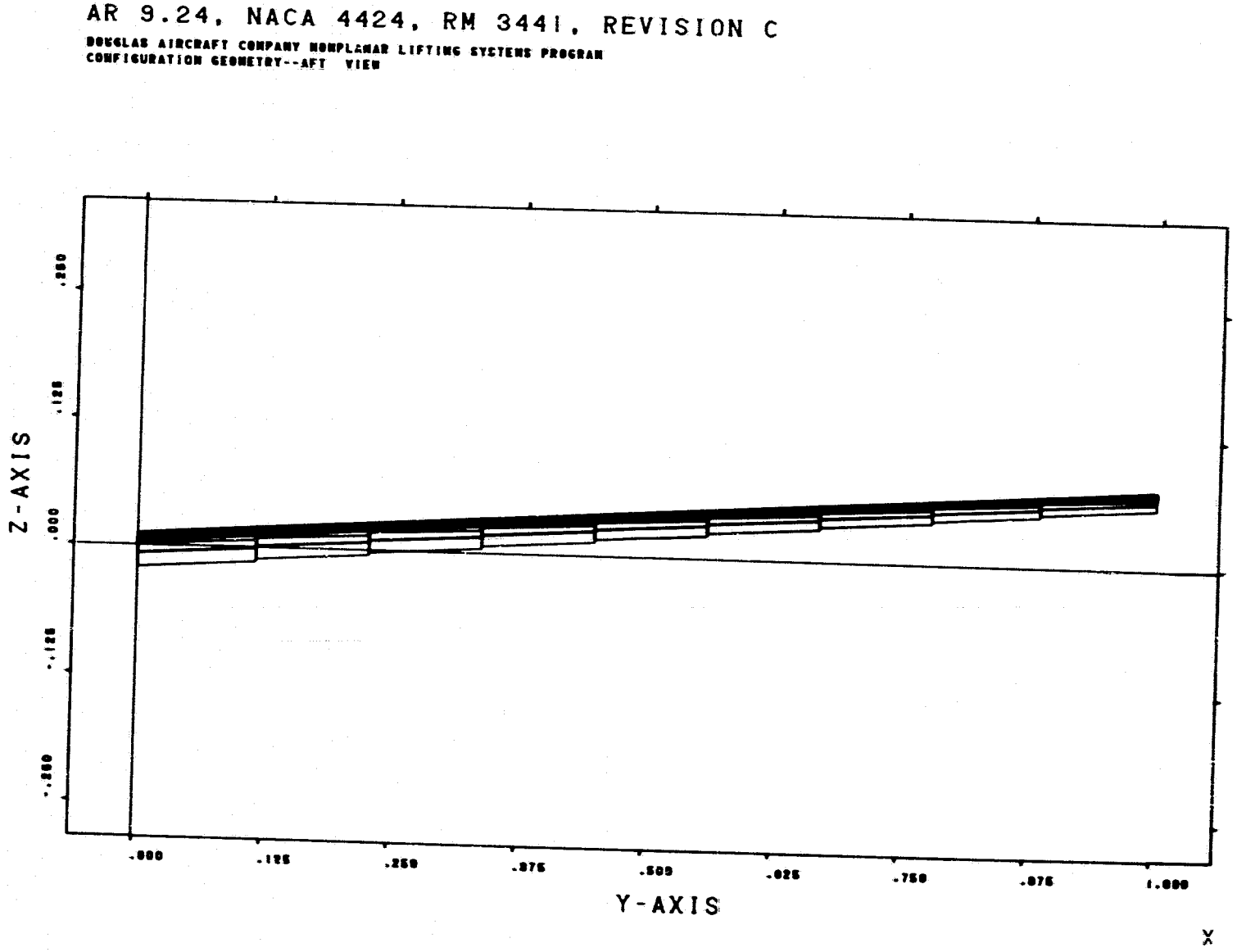

Figure 32. Aft View of NPLS Element Arrangement for Configuration of Reference 24.

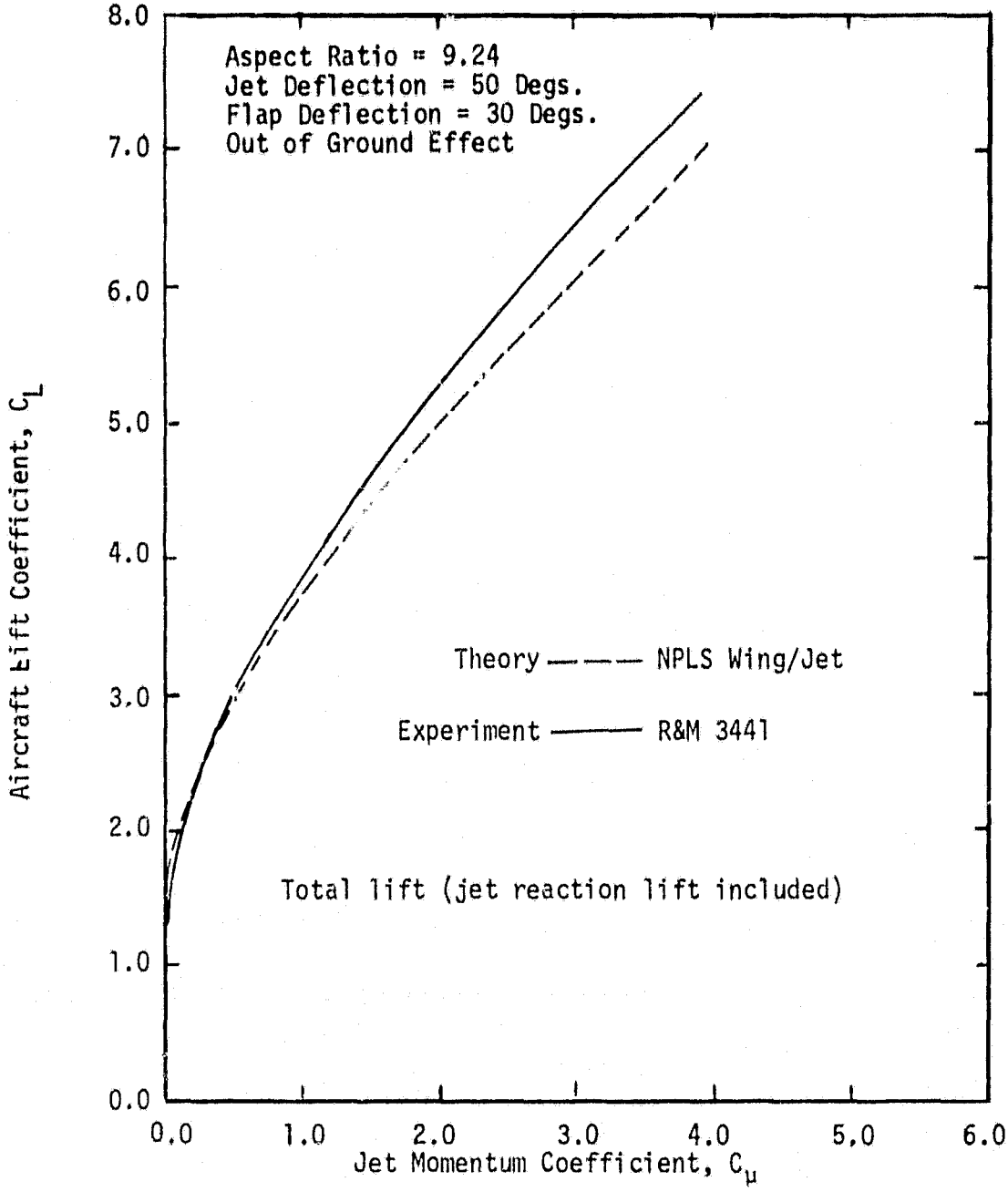

Figure 33. Comparison of Experimental and Theoretically Predicted Lift Coefficient for a Jet Flapped Aircraft.

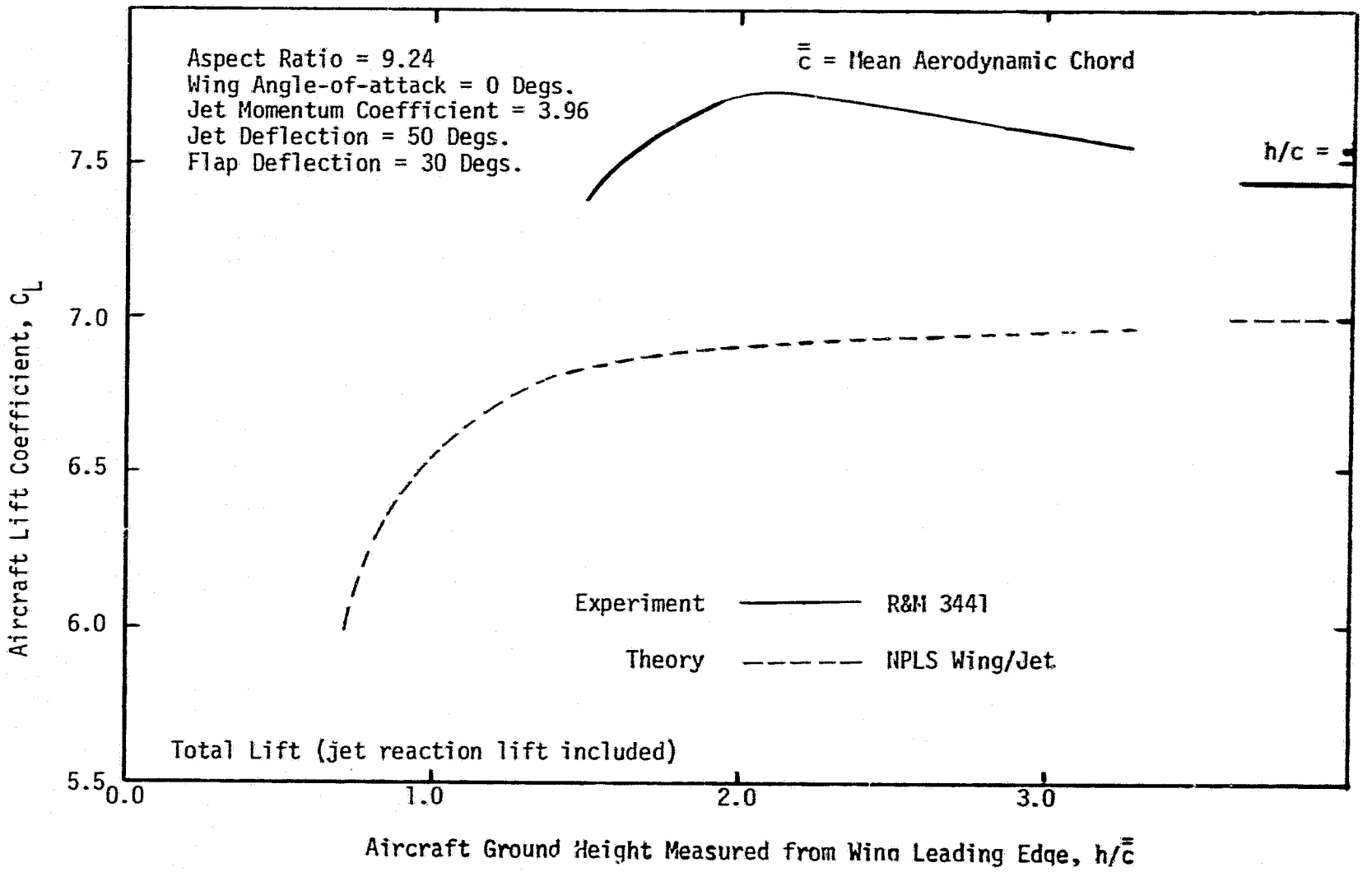

Figure 34. Influence of Ground Height on Total Lift Coefficient of a Jet Flapped Aircraft. (Jet Momentum Coefficient = 3.96)

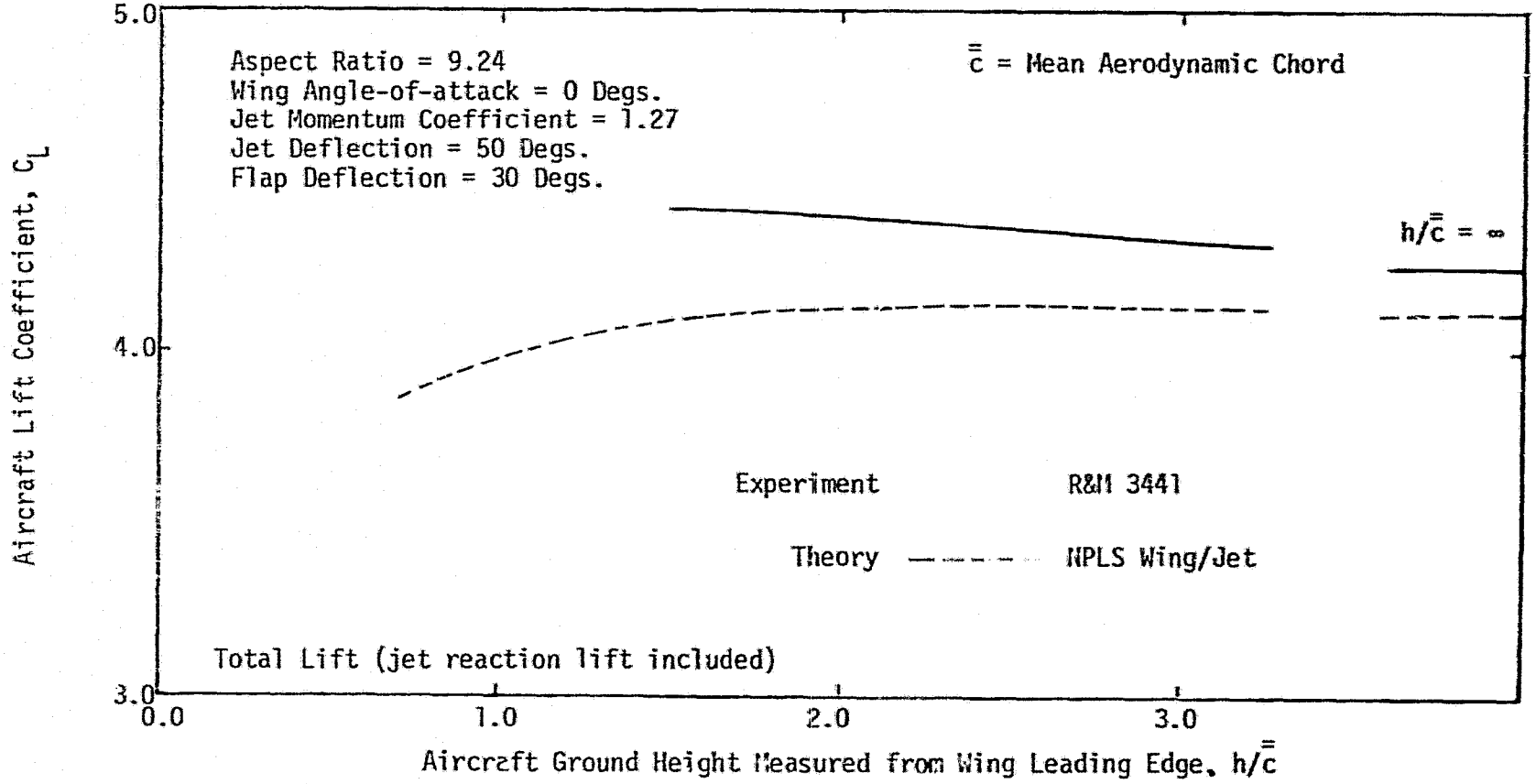

Figure 35. Influence of Ground Height on Total Lift Coefficient of a Jet Flapped Aircraft. (Jet Momentum Coefficient = 1.27)

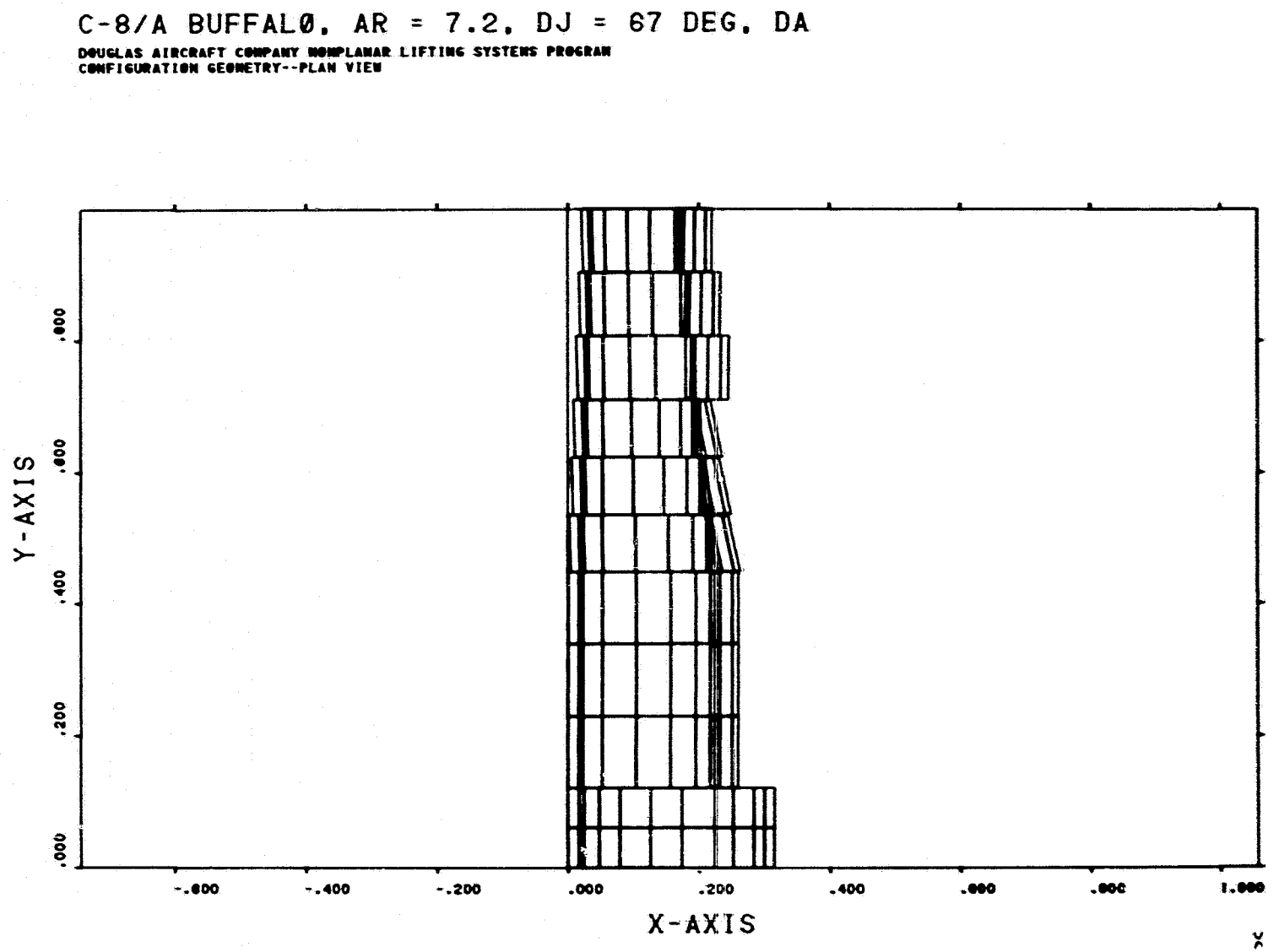

Figure 36. Plan View of Theoretical Model Employed to Analyze the C8/A Augmentor Wing Aircraft - Complex Representation.

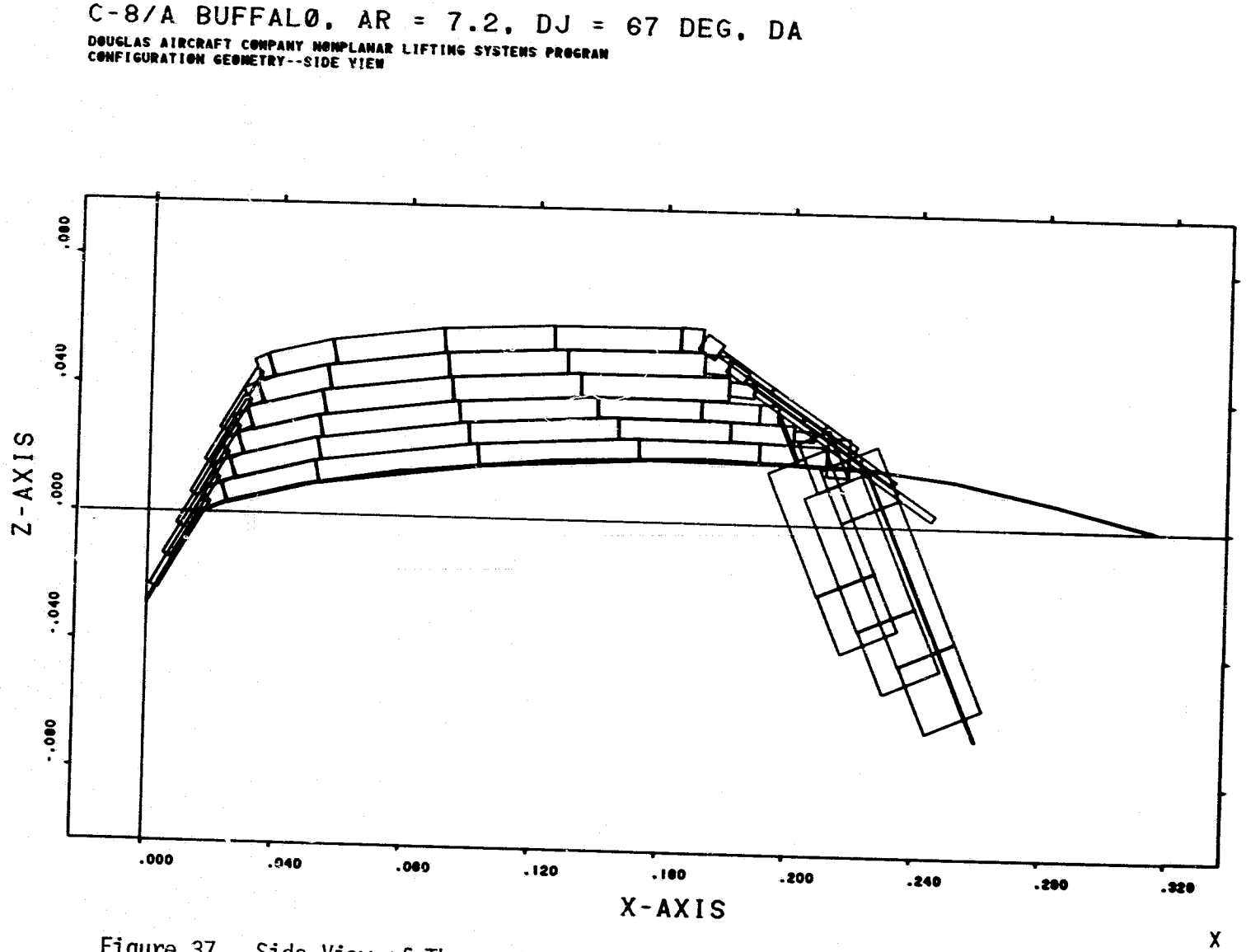

Figure 37. Side View of Theoretical Model Employed to Analyze the C8/A Augmentor Wing Aircraft - Complex Representation.

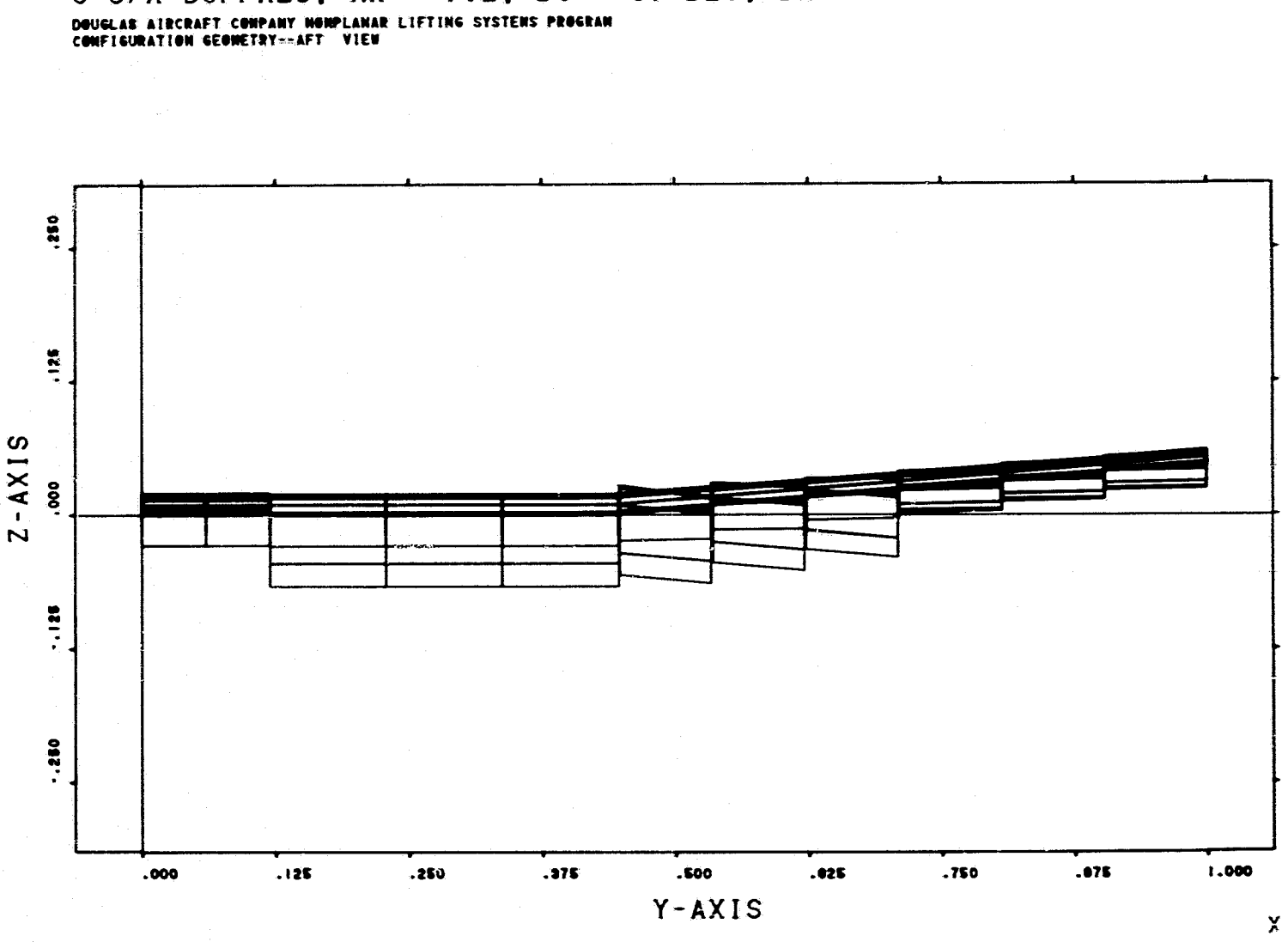

Figure 38. Aft View of Theoretical Model Employed to Analyze the C8/A Augmentor Wing Aircraft - Complex Representation.

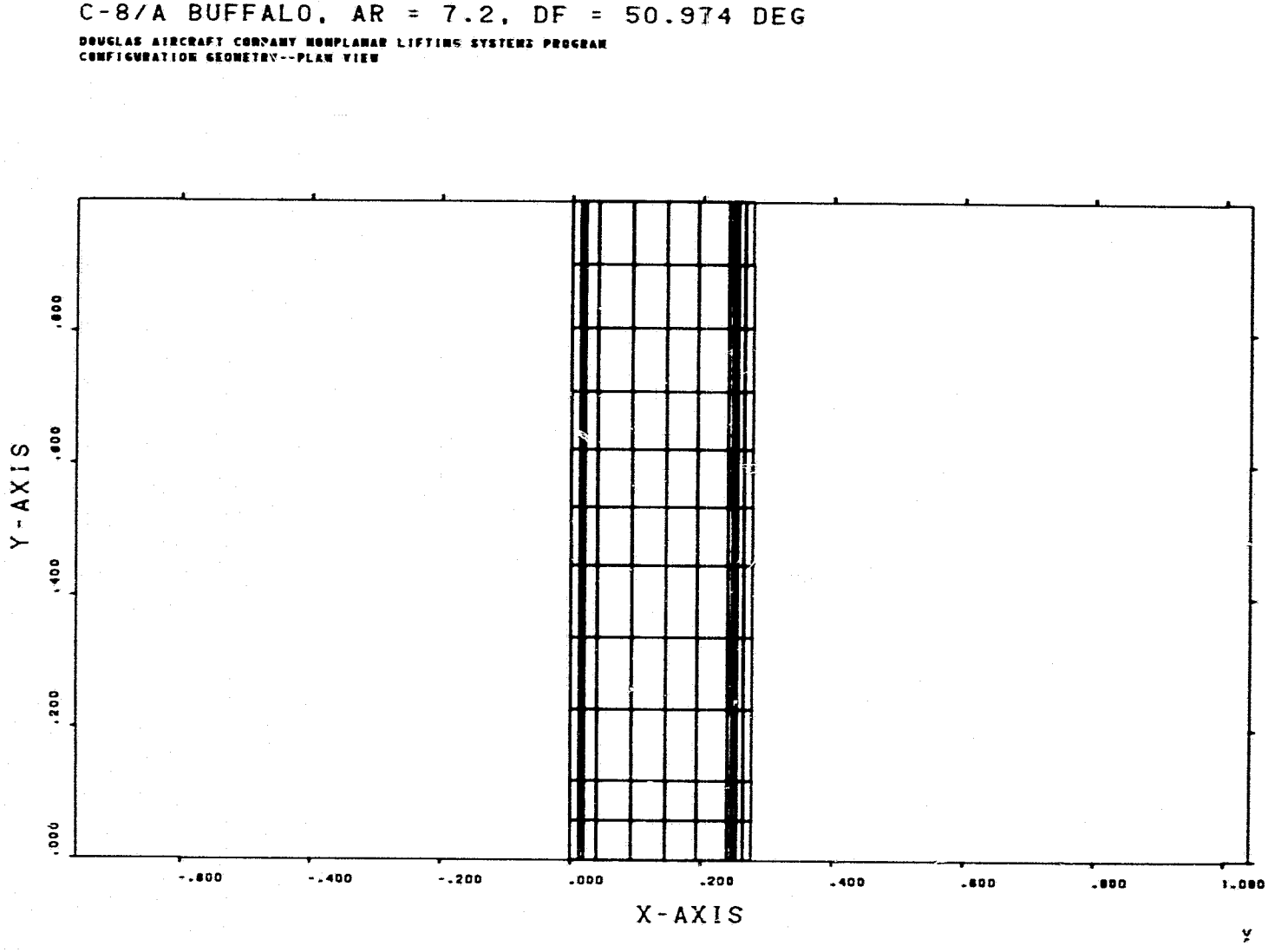

Figure 39. Plan view of Theoretical Model Employed to Analyze the C8/A Augmentor Wing Aircraft - Simplified Representation.

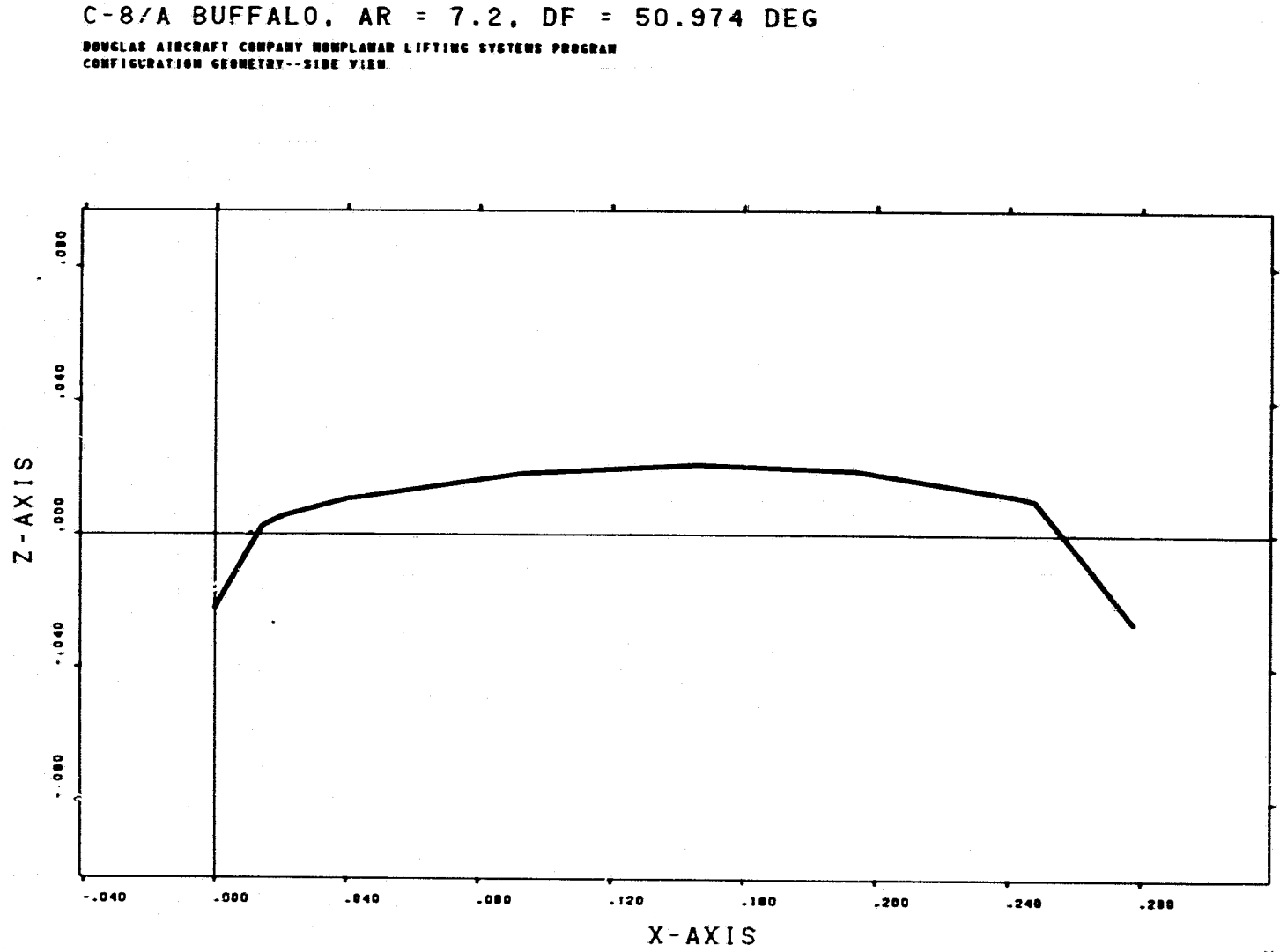

Figure 40. Side View of Theoretical Model Employed to Analyze the C8/A Augmentor Wing Aircraft - Simplified Representation.

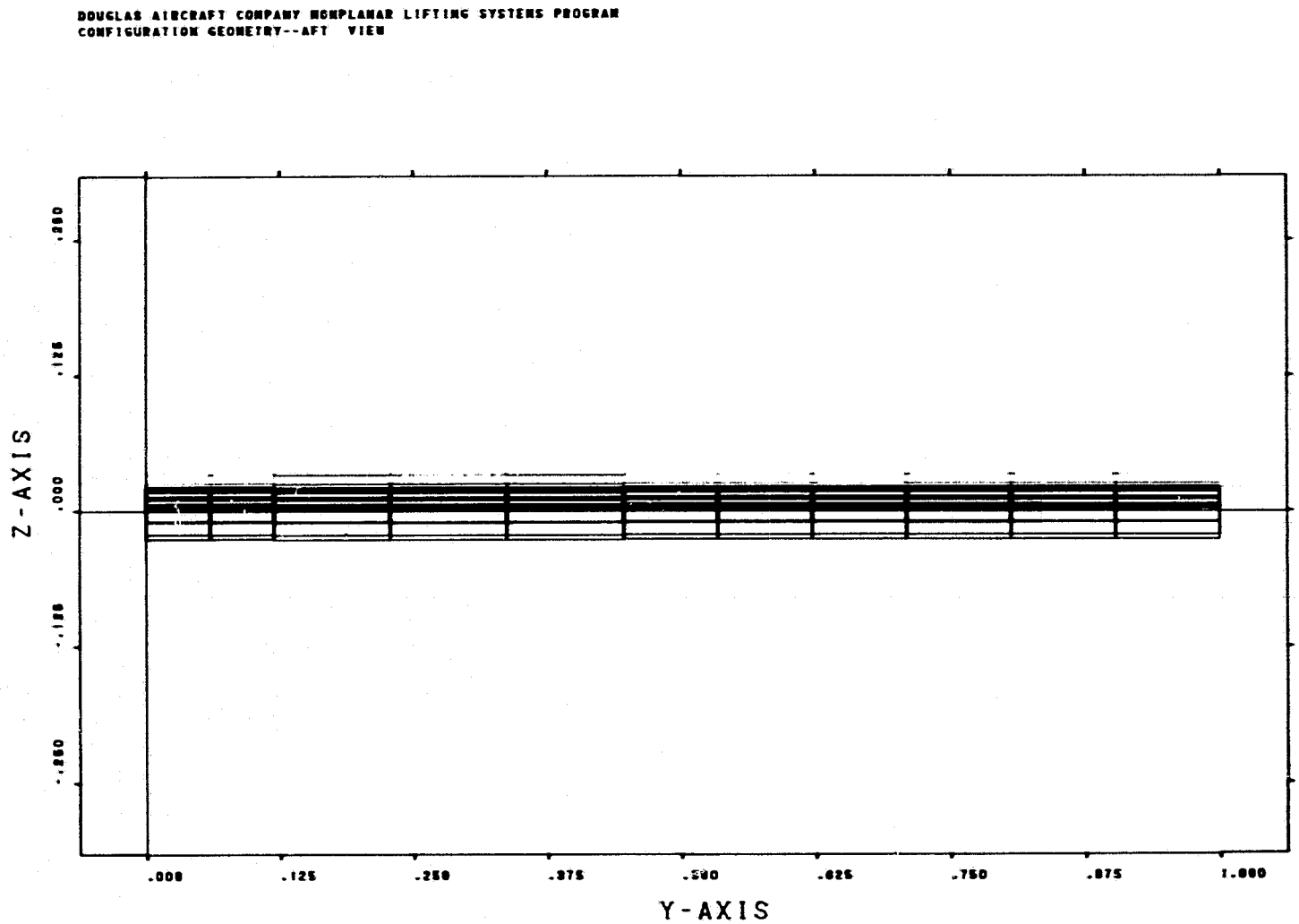

Figure 41. Aft View of Theoretical Model Employed to Analyze the C8/A Augmentor Wing Aircraft - Simplified Representation.

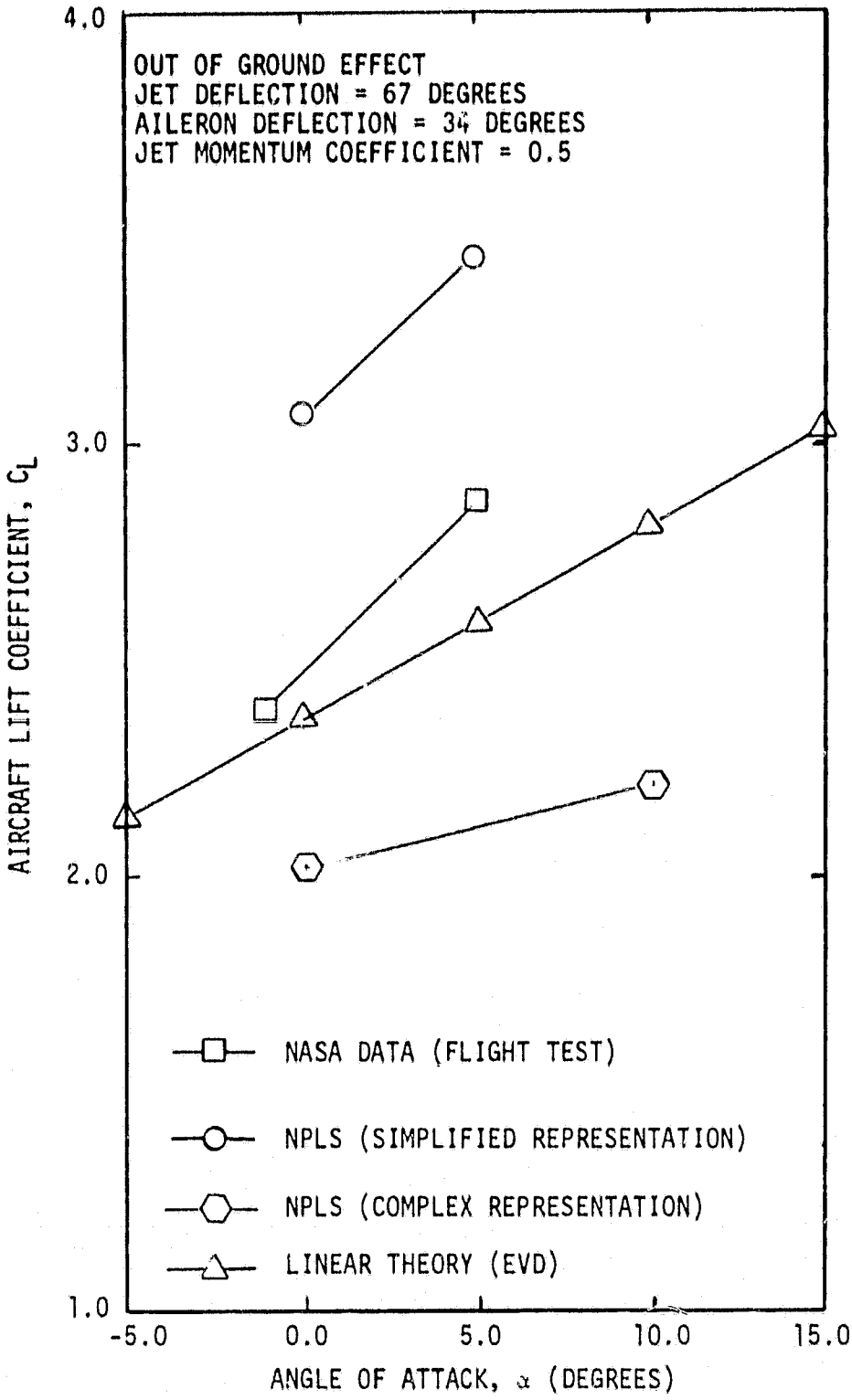

Figure 42. Lift Predicted and Measured for C-8/A Augmentor Wing Aircraft out of Ground Effect

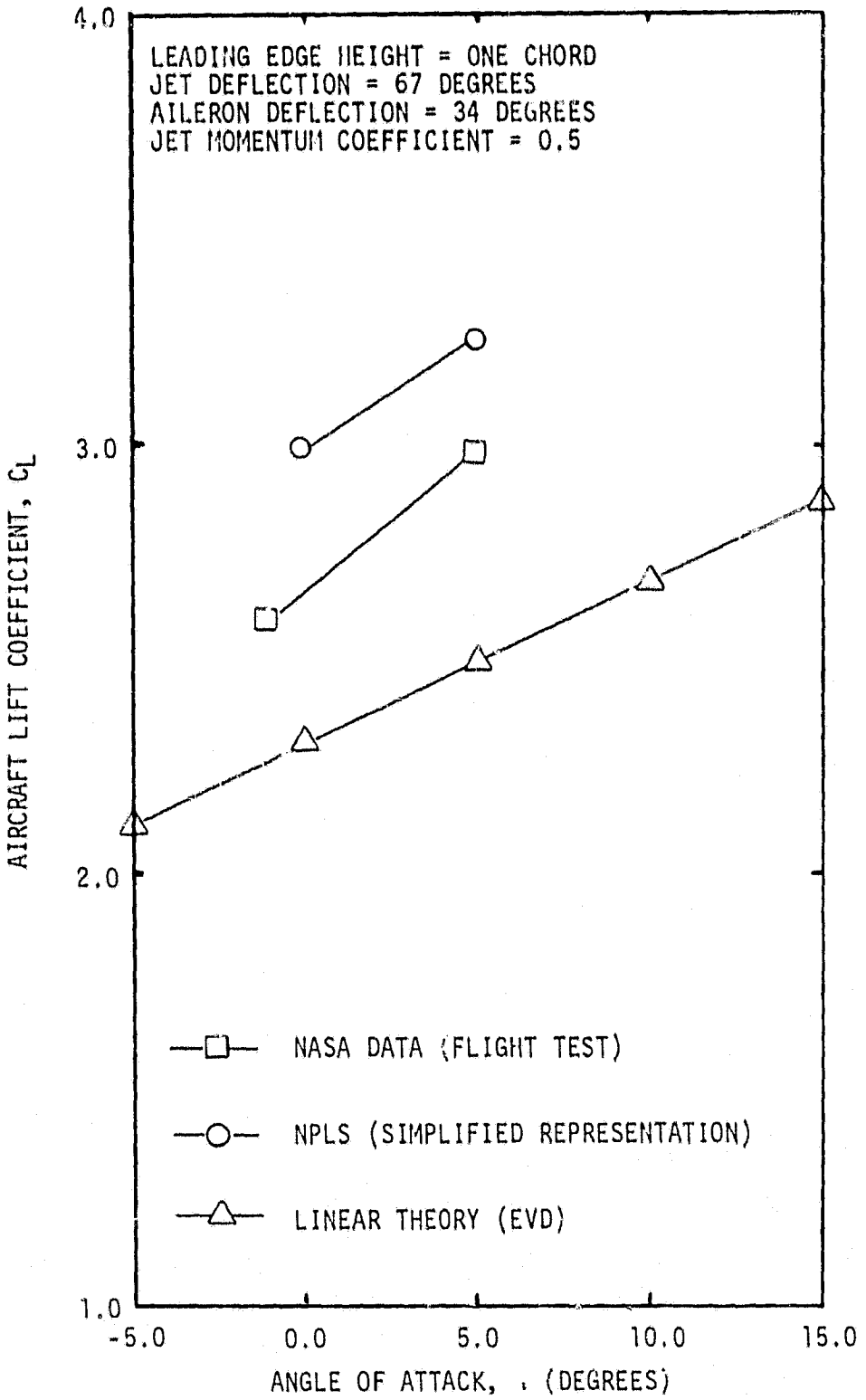

Figure 43. Lift Predicted and Measured for C-8/A Augmentor Wing Aircraft in Ground Effect